2021

Neutron scattering: A subsurface application review

Mirhasan Hosseini
Edith Cowan University

Muhammad Arif

Alireza Keshavarz
Edith Cowan University

Stefan Iglauer
Edith Cowan University

10.1016/j.earscirev.2021.103755
Hosseini, M., Arif, M., Keshavarz, A., & Iglauer, S. (2021). Neutron scattering: A subsurface application review. *Earth-Science Reviews, 221*, article 103755.https://doi.org/10.1016/j.earscirev.2021.103755

Earth-Science Reviews 221 (2021) 103755

Contents lists available at ScienceDirect

Earth-Science Reviews

journal homepage: www.elsevier.com/locate/earscirev

Neutron scattering: A subsurface application review

Mirhasan Hosseini [a], Muhammad Arif [b], Alireza Keshavarz [a], Stefan Iglauer [a,*]

[a] Edith Cowan University, School of Engineering, 270 Joondalup Drive, 6027 Joondalup, Australia
[b] Department of Petroleum Engineering, Khalifa University, Abu Dhabi 127788, United Arab Emirates

ARTICLE INFO

Keywords:
geoscience
hydrocarbons
neutron scattering
pore structure
rock characterization
SANS

ABSTRACT

Geomaterials and filling fluids properties that are pertinent to a geologic porous media can be characterized using a range of methods, such as nuclear magnetic resonance, X-rays, infrared spectroscopy, and neutron scattering (NS). In this context, NS features as an important tool elucidate key properties of a porous medium, which has recently gained significant attention. Key rock properties that can be measured by NS include: rock texture (i.e. crystallographic preferred orientation), mechanical properties (i.e. stress and strain) as well as porous medium properties (pore porosity, pore size and connectivity). In addition, NS imaging can help elucidate the phase behaviour of confined reservoir fluids in rock matrix under prevailing pressures and temperatures. Thus, a precise characterization of these properties (amongst other multiphase flow attributes) is critical for several applications in varied fields such as hydrocarbon reservoirs, geothermal systems, crystallography, geomechanics and geochemistry.

Low neutron attenuation by most substances (deep sample penetration) and strong neutron attenuation by hydrogen are essential features of neutrons that allow NS to collect high-quality data across a wide variety of subsurface conditions. These features enable NS to be ideally suited to some applications as compared to other techniques such as X-rays and magnetic resonance imaging (MRI). For example, X-rays may not have sufficient resolutions for examining nanopore structures and confined fluids. Contrastingly, MRI is limited by the visualization of a range of pore sizes. However, NS can capture angstrom-to-micron-scale information of atomic to meso-to-macro-scale structures of rocks and fluids (i.e. hydrogen-rich fluids) inside a porous medium. These insights are vital for predictive reservoir models, where meaningful reservoir-scale (hectometre-scale) predictions can be performed.

However, when compared to X-rays, neutrons have weak sources and/or low signals; therefore, experimental time can be quite long and samples need to be relatively large. Other limitations of NS (some may be also true of other techniques) include problems like accessing neutron sources (e.g. complicated nuclear processes for neutron production and small number of available instruments when compared to X-rays), high costs, and the strong absorption of neutron signals by some elements [e.g. cadmium (Cd), boron (B), and gadolinium (Gd)].

Despite the potential of NS, a review that considers key NS subsurface applications, limitations, and outlooks is currently lacking. Thus, in this review, we describe the basic concepts, experiments, methods, requirements, restrictions, and applications of NS for rock and fluid characterization.

This study finds that despite its overall challenges, NS is a promising technique for characterizing subsurface rock and fluid systems, opening diverse avenues for future technological and scientific research within this area.

1. Introduction

Precise reservoir characterization is vital, both economically and scientifically, for several applications including: hydrocarbon recovery (Green and Willhite, 1998; Lake et al., 2014; Thanh et al., 2020), CO_2 geo-storage (IPCC, 2005; Ito et al., 2017; Raza, 2017; Iglauer, 2018), H_2 geo-storage (Yekta et al., 2018; Hemme and Van Berk, 2018; Iglauer et al., 2021a, 2021b), groundwater production (Pluymaekers et al., 2012; Al-Enezi et al., 2018), subsurface remediation (Bust, 2002; Cornelissen et al., 2011; Fraiese et al., 2020), nuclear waste storage (Pryakhin et al., 2015; Tsang et al., 2015), geothermal engineering (Aragón-Aguilar et al., 2017; Zhu et al., 2020; Balcewicz et al., 2021), coal mining and coal bed methane recovery (Fan et al., 2012; Tang et al., 2017; Ye et al., 2019; Liang et al., 2020), as well as geophysical explorations (Alao

* Corresponding author.
E-mail address: s.iglauer@ecu.edu.au (S. Iglauer).

https://doi.org/10.1016/j.earscirev.2021.103755
Received 11 February 2021; Received in revised form 29 June 2021; Accepted 26 July 2021
Available online 3 August 2021

et al., 2013; Huang et al., 2015; Johann and Monteiro, 2016; Oyeyemi et al., 2019).

The key properties for reservoir characterization include, but are not limited to, crystal structure, texture, stress, strain, porosity, permeability, pore size, and phase behaviour of confined reservoir fluids in rock matrix. The crystal structure analysis of geomaterials provides crucial information, such as detailing the kinetics of gas hydrate formation or decomposition, and how elements of minerals are stacked together (Wenk, 2006; Kuang et al., 2018). Texture and strain are other properties that provide essential information regarding shape, size, and arrangement of grains and homogeneity of rock (Wenk, 1985; Ertel et al., 1989; Feldmann, 1989; Kocks et al., 1998). Porous medium properties, such as porosity, permeability, and pore size, are required in order to identify and simulate fluid flow in porous media, whereby they can significantly affect the mechanisms of gas storage in geological formations (Hosseini et al., 2014; Hosseini, 2016). The phase behaviour of confined reservoir fluids in rock matrix under various conditions is essential for interpreting rock-fluid interactions and molecular dynamic simulations of interfacial phenomena (Neil et al., 2020b; Gautam et al., 2017a).

In this context, numerous characterization techniques can be applied for laboratory investigation of rock core samples, where these include, but are not limited to, X-ray diffraction (XRD), magnetic resonance imaging (MRI), gas absorption, mercury intrusion, scanning electron microscopy (SEM), and 3D micro-computerized tomography (CT) imaging (Collins and Wright, 1985; Blunt et al., 2013; Abdoulghafour et al., 2020). XRD is normally used to determine rock mineralogy (Hosseini, 2018). MRI is a powerful technique to characterize confined fluids in rock pore networks (Zhang et al., 2018). Gas absorption and mercury intrusion (porosimetry/pycnometry) are conventional techniques for rock microstructure characterization (Xu, 2019). 3D micro-CT imaging using X-rays can efficiently resolve the rock microstructure (Iglauer et al., 2011; Hall, 2013; Zhao et al., 2017a, 2017b, 2017c; Zambrano et al., 2019). A combination of SEM and micro CT can extend the observation limit required for rock microstructure characterization i.e. a multiscale correlative imaging approach (Wenk, 2006; Ma et al., 2017; Arif et al., 2020). However, the characterization of microstructural properties of rock (e.g. porosity, permeability, and pore size) remains a challenge owing to the complexity of its geological structure, compositional heterogeneity and texture (Sun et al., 2017). This is particularly true for unconventional reservoirs, such as tight sands and shale rocks (Ma et al., 2017; Arif et al., 2020). Conventional methods such as mercury intrusion and gas absorption are limited to only measuring the microstructural properties of open pores (Sinha et al., 2013a, 2013b; Rashid et al., 2015), while 3D micro-CT imaging using X-rays may not have sufficient resolutions for examining nanopore structures and confined fluids (Basavaraj and Gupta, 2004). XRD is also somewhat insensitive to the presence of hydrogen in mineral structures. Moreover, magnetic resonance imaging (MRI) is limited by its visualization of a range of pore sizes (Chen et al., 2003).

In addressing these problems, one key technology that has emerged in the last three decades is neutron scattering (NS) (Wong and Howard, 1986; Sen and Mazumder, 2002; Zhao et al., 2017a, 2017b, 2017c). Neutron scattering has been successfully applied to rigorously resolve rock microstructural properties across a range of scales (Wenk, 2006). A neutron's high sensitivity to light elements like hydrogen, and its high penetrating ability enables the examination of confined-fluid behaviour (especially in hydrogen-rich compounds such as water) at relevant pressures and temperatures, investigating large samples with little or no radiation damage whilst characterizing nanopore structures (1 nm to 10 μm) (Weber et al., 2013; Dewanckele et al., 2014; Xu, 2019). In technological terms, neutrons offer a special, non-destructive tool for quantifying atomic structural information such as texture, stress, strain, as well as porous medium information such as porosity, connectivity, and surface area (Ramsay, 1988; Ramsay, 1993; Liang et al., 2009; Le Floch et al., 2015).

Thus, during the past three decades, there has been growing interest in NS technology in several subsurface science and engineering fields; e.g., crystallography, geochemical and geomechanical analysis, enhanced hydrocarbon recovery, geothermal energy production, and CO_2 geo-sequestration (Anovitz et al., 2011; Anovitz et al., 2013; Bahadur et al., 2016; Wang et al., 2017; Abe et al., 2018; Carvalho et al., 2019; Zambrano et al., 2019).

However, although specialized reviews of specific applications of neutron-based techniques within earth science have been published (e.g. Wilding et al., 2005; Wenk, 2012; Perfect et al., 2014; Tengattini et al., 2020), a comprehensive review covering NS principles and types as well as all main NS subsurface applications, limitations, and future outlooks is currently lacking.

This review article therefore provides a succinct overview of NS principles, historical developments, types, and applications. The article also focuses on applications of NS (especially SANS) as a technique of choice, to characterize or evaluate reservoirs for CO_2 geo-storage, enhanced hydrocarbon recovery, and enhanced geothermal systems. Future trends and problems associated with NS are also reviewed.

This review thus acts as an entry point for new researchers in this area, and provides sufficient evidence of the effectiveness of NS for a range of subsurface applications.

2. Neutron scattering

This section presents a brief overview of neuron properties, historical developments and of concepts pertinent to NS techniques in order to lay the groundwork for the most important applications of NS in subsurface investigations.

2.1. Neutron properties

In 1930, Walther Bothe and Herbert Becker showed that radiation of high penetrating power is produced when some atoms, such as beryllium (Be), boron (B), and lithium (Li), are bombarded with α-particles emitted from polonium (Po) (Oesch et al., 2019). This power was also observed by James Chadwick, whereby subatomic particles were called neutrons (Nesvizhevsky and Villain, 2017; Chadwick, 1932). Neutrons are powerful agents for probing the nuclear and magnetic structure of condensed matter and lattice dynamics. Neutrons can investigate the diffusion of hydrogenous molecules and characterize light atoms such as lithium and hydrogen, in addition to distinguishing adjoining elements in the Periodic Table. Neutron mass (1.675×10^{-27} kg) constitutes a significant portion of the total mass of an atomic nucleus. Further, since neutrons are electrically neutral and penetrate profoundly into a sample, they can be used to examine large, geologically interesting rock samples (Wenk, 2012).

Whilst there are various neutron sources, the most applicable sources for scattering purposes are continuous reactors and spallation sources (Wenk, 2012). Continuous (steady state) reactors produce neutrons (e.g. thermal or cold) continuously by fission processes, whereas spallation sources operate in a pulsed (or time-of-flight) mode to produce pulsed neutron beams via the collision of high-energy protons or electrons (Melnichenko, 2016).

The depth of penetration massively depends on the species, density, and energy of a form of radiation. The exact depth of penetration of neutrons depends on an atomic species they interact with. However, for most samples and atomic species, neutrally charged neutrons have a greater penetrating capability than X-rays and electrons (Fig. 1). It should be noted here that, as shown in Fig. 1, the penetration depth for neutrons is in the order of 1 cm, while it is 1 mm for X-rays and 1 μm for electrons. For example, for low-density solid matter, the size of the scattering centre (nucleus) is usually much less than the distance between the scattering centres. As a result, these neutral particles have high penetration and low absorption through most materials. Neutrons have both wave-like and particle-like properties (Wenk, 2006). Some

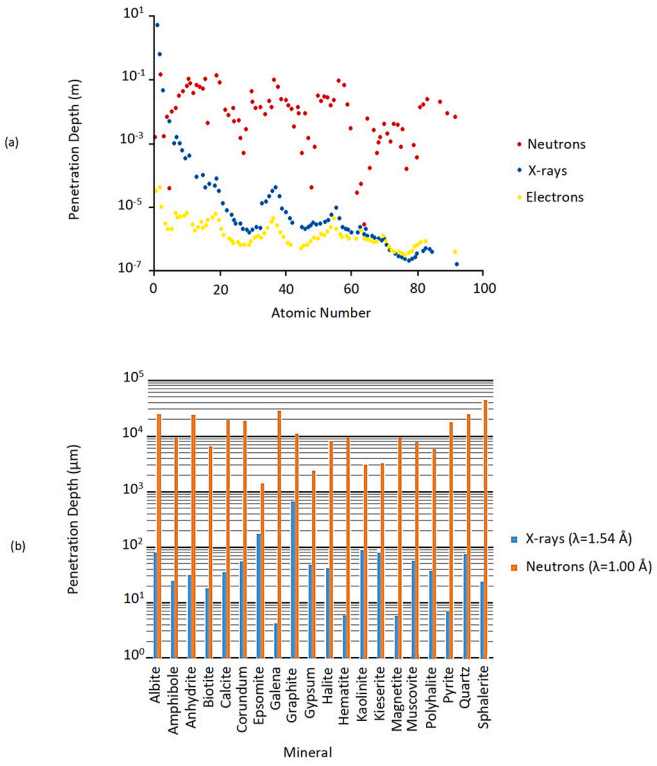

Fig. 1. Comparison of penetration depths for neutrons, X-rays, and electrons in (a) various atomic numbers [reproduced from Wenk, 2012 with permission from the Mineralogical Society of America] and (b) various minerals [reproduced from Brokmeier, 1999 with permission from the Overseas Publishers Association]

neutron properties are summarized in Table 1.

2.2. History of neutron scattering

Over history, NS technology has experienced substantial development and growth. In 1936, a radium-beryllium neutron source with low flux was used in an experiment, where it was found for the first time that neutrons could be scattered (Wenk, 2006). In 1944, the first neutron diffraction (elastic NS) experiment was implemented by Ernest Wollan on single crystals (Mason et al., 2012). By 1949, the NS application was transformed to more sophisticated architecture, where neutron diffraction was used to analyze the magnetism of various structures, from simple structures with collinear spins to complicated incommensurate structures with noncollinear spins (Shull and Smart, 1949; Berry and James, 2001). Successful neutron-based studies of material structures in high-pressure conditions began in the 1960s (Bloch et al., 1966; Lechner and Quittner, 1966; Brugger et al., 1967; Redfern, 2002). In the early part of the 1960s, the dynamic properties of atoms within solids were investigated using inelastic NS, where this research became prominent for scholars (Hertzog, 1980; Underwood and Dyos, 1986; Skipper et al., 2000; Choudhury and Chaplot, 2008; Piovano, 2015; McFarlane et al., 2016). Rietveld subsequently introduced a technique for the refinement of crystal structures from NS data, including elements such as positions and intensities of diffraction peaks (Rietveld, 1967; Rietveld, 1969). This method uses a least-squares approach to fit a theoretical line profile calculated from many parameters (e.g., reflected peak shape and intensity, unit cell parameters, and coordinates of all atoms in the crystal structure) to experimental data (Rietveld, 1969). Modern Rietveld refinement is now used as a potent tool for the study of crystal structures (Stinton and Evans, 2007; Pereira et al., 2018). In this regard, many refinement software packages are available for evaluation; e.g., the General Structure Analysis System (GSAS) (Larson and Von Dreele, 2004), graphical user interface to GSAS (EXPGUI) (Toby, 2000), FULLPROF (Rodríguez-Carvajal, 1990), and MAUD (Lutterotti et al., 1999). In the geoscience context, determination of the crystal structure of minerals was recognized as the main geoscience application of NS until 1980 (Wenk, 2012). The theory of small-angle neutron scattering (SANS), one of the most important elastic NS methods, was then developed in detail by (Crowley, 1984) and Cohen Stuart et al. (1986). SANS tests offering coverage in real space over a broader spectrum have since been implemented in major research areas including biology, chemistry, materials science, geoscience, and engineering. For example, SANS tests have been conducted to examine disordered materials with amorphous compounds like glass and short-range-order liquids like water (Wong and Howard, 1986; Menelle et al., 1989; Jenkins and Donald, 1996; Redfern et al., 1997; Eckold et al., 1998; Redfern et al., 2000; Wignall and Melnichenko, 2005; Hollamby, 2013; Hayward et al., 2018). The atomic pair distribution function (PDF), which specifies the nearest surrounding of atoms, has been used for the study of disordered materials (Proffen and Billinge, 1999). Jasti et al. (1987), features as perhaps the first instance of a study quantitatively analyzing flow imaging in porous media using neutron radiography (Tengattini et al., 2020). The first neutron tomography of rock for permanent disposal of radioactive wastes were reported by Kupperman et al. (1990) and Rhodes et al. (1992). Neutron scattering experiments have been widely used to characterize rare-earth metals (Blume et al., 1962; Kostorz, 1988; Perreault et al., 2019), polymers (Higgins, 2016), proteins (Ibrahim et al., 2017), colloids (Vrij, 2003), and other disordered materials (Wenk, 2006; Wenk, 2012; Proffen and Billinge, 1999). Some countries have placed substantial developments in neutron facilities. This has continued to today, where SNS (spallation neutron sources) at Oak Ridge, USA, features the most powerful accelerator-based neutron source facility in the world for scientific research and industrial development (Granroth et al., 2006).

2.3. Neutron interactions

Neutrons interact with atoms in two ways, via neutron–electron and

Table 1
Neutron-specific properties [reproduced from Wenk, 2006 with permission from the Mineralogical Society of America].

Physical properties	Mass (kg)	Spin	Electrical charge (C)	Magnetic dipole moment (J T^{-1})
	1.675×10^{-27}	1/2	0	1.913 μ_N*
Relation between mass (m_n , kg), velocity (v, m/sec), kinetic energy (E, meV), wave vector (k, $Å^{-1}$), wavelength (λ, Å), and temperature (T, K) of the neutron	$E = ½m_nv^2 = k_BT = (hk/2\pi)^2/(2m_n) = (\hbar^2k^2)/(2m_n)$ $k = 2\pi/\lambda = m_nv/(h/2\pi) = m_nv/\hbar$			
Approximate ranges of E and corresponding T and λ	Neutron	Temp (T/K°)	Wavelength (λ/Å)	Energy (E/meV)
	Cold	1 to 120	3 to 30	0.1 to 10
	Thermal	60 to 1,000	1 to 4	5 to 100
	Hot	1,000 to 6,000	0.4 to 1	100 to 500

* Nuclear magneton: $\mu_N = 5.051 \times 10^{-27}$ (J T^{-1})

neutron–nucleus interactions. The neutron–electron interaction is a spin–spin interaction that occurs between the magnetic moment of unpaired electrons and the magnetic moment of neutrons, where this type of interaction is called magnetic scattering. The neutron–nucleus interaction is the most probable, occurring through short-range (~ 1 fm) nuclear forces. There are four principal neutron-nucleus interactions: nuclear fission, neutron capture, inelastic neutron scattering (neutron spectroscopy), and elastic neutron scattering (neutron diffraction). In the first two interactions, known as absorption interactions, the neutron is absorbed into the nucleus and something different emerges. Nuclear fission is a process whereby an excited compound nucleus divides into two main fragments plus several neutrons. The most important cases for nuclear fission are isotopes of uranium and plutonium. A nucleus may capture a neutron and emit a proton, an alpha particle, or a gamma photon. Neutron capture can occur in almost any target nucleus (Bodansky, 2004). In the remaining interactions, known as neutron scattering interactions, a neutron emerges from the reaction due to the scattering contrast between different components within the medium (Melnichenko and Wignall, 2007; Ferrage et al., 2018). Neutron scattering is the irregular dispersion of free neutrons by a substance. In elastic NS, the neutron bounces off the bombarded nucleus without disturbing or destabilizing it (Fig. 2a). The fast neutron loses energy when it interacts elastically with the nucleus of a low-atomic-number material, such as hydrogen. In an inelastic NS, the neutron bounces off the nucleus, which excites it to rapidly emit what are considered inelastic gamma rays (Fig. 2b). An inelastic NS is only feasible when the energy of the neutron reaches the characteristic threshold of an element (Melnichenko, 2016). The neutron–nucleus scattering interaction can be described by coherent and incoherent scattering. In coherent scattering (diffraction effects), information on the relative positions of atoms can be obtained via interference between scattered neutron waves from various atoms (various scattering centres). However, in incoherent scattering, information on the relative positions of atoms is lost due to the lack of interference between the scattered neutron waves from various atoms.

The total scattering cross section (σ_{tot}), which refers to the area of an atom that effectively scatters incident particles, is defined as

$$\sigma_{tot} = 4\pi b^2, \tag{1}$$

where b is the atomic scattering length describing the dispersion of neutrons (Wenk, 2012). The attenuation of the neutron beam, passing through a homogeneous sample can be expressed by the Lambert–Beer law:

$$I(x) = I_0 e^{-\mu x}, \tag{2}$$

where $I(x)$ is the neutron beam intensity ($cm^{-2}. s^{-1}$), I_0 is the initial beam intensity ($cm^{-2}. s^{-1}$), μ is the linear attenuation coefficient, and x is the sample thickness along the beam direction (cm) (Calloway, 1997; Kocsis et al., 2006; Anderson et al., 2009). For a sample comprising n different elements, the law can be generalized as:

$$I = \int_{\lambda_{min}}^{\lambda_{max}} I_0(\lambda) e^{-\sum_{i=1}^{n} x_i \mu_i(\lambda)} d\lambda, \tag{3}$$

where x_i is the thickness of the layer i and μ_i is expressed as:

$$\mu_i(\lambda) = \left(\frac{\rho_i N_A}{M_i}\right)\sigma_i(\lambda), \tag{4}$$

where ρ_i is the density of the i^{th} layer ($g.cm^{-3}$), M_i is the molar mass of element i, N_A is Avogadro's constant, and $\sigma_i(\lambda)$ is the cross section of element i. The main causes of attenuation of neutrons are scattering (coherent and incoherent) and absorption. Therefore, $\sigma_i(\lambda)$ is the sum of the coherent scattering cross section, σ_{icoh}, the incoherent scattering cross section, σ_{inc}, and the absorption cross section, σ_{abs}. It is evident that this law depends on the characteristics of the neutron beam (i.e., wavelength).

2.4. Comparison between neutron and X-ray scattering

Neutron scattering and X-ray scattering are two of the most powerful methods available to evaluate rock and fluid properties, interactions, and structures. Since the principal diffraction geometries of these two methods are similar, the experimental set up required to perform both neutron and X-ray scattering are also similar (Fig. 3). However, there are some differences between the methods. For example, low attenuation and deeper penetration are two key features of neutrons in comparison to X-rays, which make them viable for studying thicker rock samples. Further, while X-rays assess variations in electron density, neutrons assess variations in the nuclear potentials (nuclear scattering) and magnetic fields made by unpaired electrons (magnetic scattering). The X-ray scattering cross section is directly linked to the atomic number ($\sigma_{tot} \propto Z^2$, Z: atomic number) because X-ray scattering occurs by electrons. However, NS happens by atomic nuclei, so scattering factors are influenced by nuclear forces in isotopes (Wenk, 2006; Anovitz et al., 2011). Therefore, it is easier to discriminate neighbouring elements and isotopes by neutrons compared to X-rays. Accordingly, the total NS cross section of hydrogen is greater than its total X-ray scattering cross section (Fig. 4). This has implications for rock–water interaction studies at nano to micro scales (and at different time scales), as well as for other hydrous phases using inelastic or quasi-elastic NS methods.

The number of neutrons that have interactions with atoms is low;

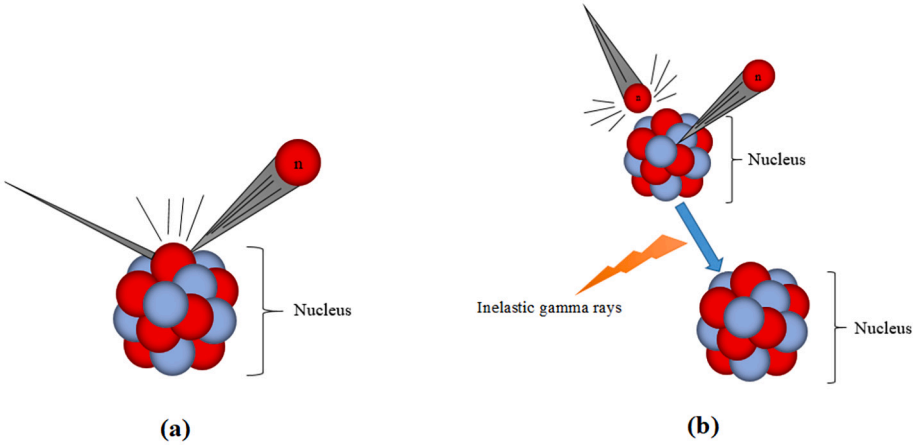

Fig. 2. Schematic illustration of neutron scattering. (a) Elastically scattered neutron. (b) Inelastically scattered neutron. [Reproduced from Schlumberger Oilfield Glossary, 2021 with permission from Schlumberger].

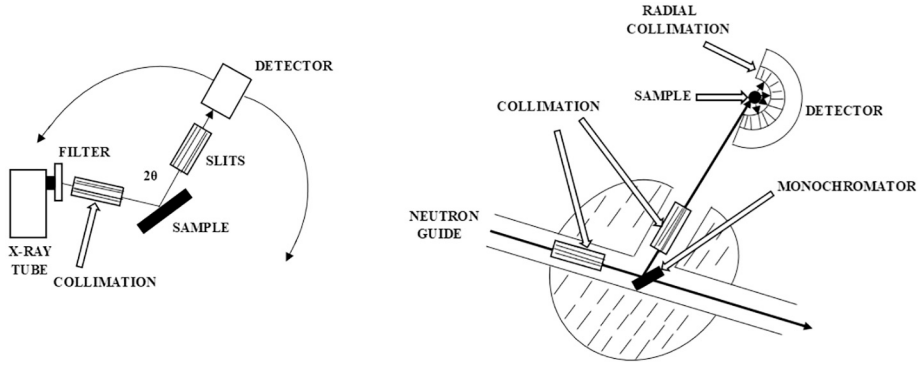

Fig. 3. Schematic of X-ray and neutron scattering geometries [reproduced from Wenk, 2006 with permission from the Mineralogical Society of America]

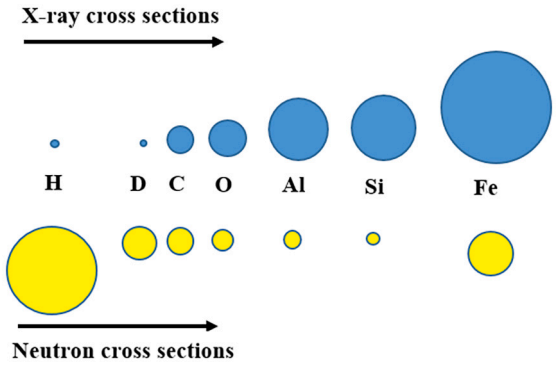

Fig. 4. X-ray and NS cross sections compared for various elements [modified from Anovitz et al., 2011]

therefore, neutrons have weak sources and/or low signals resulting in very low scattering intensities. Consequently, unlike X-rays, neutrons require long experimental time and large samples volumes for evaluation (Wenk, 2012).

2.5. Neutron scattering methods

Neutron scattering can be categorized into two groups, namely 1) neutron diffraction (elastic scattering) techniques, including SANS, neutron reflectometry, and spin-echo small-angle neutron scattering (SESANS); and 2) neutron spectroscopy (inelastic scattering) techniques, which include neutron time-of-flight scattering, neutron triple-axis spectrometry, neutron backscattering, and neutron spin echo (Zabel et al., 2000; Meyer et al., 2003; Farago, 2006; Rehm et al., 2012; Melnichenko, 2016; Hiraka et al., 2020). Table 2 presents a succinct summary of these elastic and inelastic NS methods. Also, neutron logging and imaging are other methods that use neutron scattering.

2.5.1. Elastic scattering methods

In neutron diffraction methods, the energy of the neutron does not change after scattering. SANS is a technique that uses neutron diffraction at small scattering angles and requires little sample preparation (Radlinski and Hinde, 2001). SANS is the technique of choice for characterizing nanoscale-sized structures (Hammouda, 1995). In this method, a sample (solid, crystal, powder, or aqueous solution) is targeted by an incident neutron beam (Fig. 5). The sample scatters the neutrons onto a 2-dimensional detector and the intensity of the elastically scattered neutrons is then recorded as a function of the scattering angle (Frielinghaus, 2012). In the case of isotropic scattering, information regarding the size distribution of scattering objects can be obtained by comparing the measured scattering intensity (I) to the scattering variable (Q) to determine $I(Q)$. Eq. (5) gives the scattering variable (Wenk, 2006):

$$Q = \frac{4\pi}{\lambda} sin\left(\frac{\theta}{2}\right), \tag{5}$$

where λ is the wavelength of the neutrons and θ is the scattering angle. Within the small-angle approximation (typically from 0.2° to 20°), Q simplifies to $Q = 2\pi\theta/\lambda$. The value of Q for the SANS scattering variable usually ranges from 0.001 $Å^{-1}$ to 0.45 $Å^{-1}$ (Radlinski and Hinde, 2001). For a constructive interference to occur, Q must be perpendicular to the scattering planes whilst the condition $Qd = 2\pi n$ must be satisfied, where d is the distance between two scattering planes and n is an integer. Combining this condition with Eq. (5) yields Braggs's law (Bragg et al., 1934):

$$n\lambda = 2dsin\left(\frac{\theta}{2}\right) \tag{6}$$

This equation relates the scattering angle, θ, to the inter-planar spacing in a crystalline sample and is critical in determining the structure of an unknown crystal. Using the known values of λ and θ, the plane spacing of the layer of atoms or ions can be obtained.

A typical SANS instrument includes four components i.e. the monochromation, collimation, scattering, and detection (Fig. 5). The monochromatic incident beam is collimated before it hits the sample. Scattering is performed/completed using either liquid or solid samples. Typical sample environments for in-situ SANS measurements are electromagnets, pressure cells, shear cells, and humidity cells. The SANS method has been widely applied for rock and fluid characterization (Sun et al., 2017; Yang et al., 2017; Sun et al., 2019; Neil et al., 2020b). SANS has been used for resolving porosity from micro-scale to nano-scale (Arif et al., 2020; discussed in detail in Section 3). Small angle X-ray scattering (SAXS) is another small angle scattering technique that probes the same size scale as SANS. However, the source of scattering for SANS and SAXS is different. While scattering in SANS is attributed to variations in scattering length density (discussed in detail in Section 3.3.1.1), scattering in SAXS is caused by variations in electron density.

SESANS is another neutron diffraction technique that does not require a beam stop and is not constrained by the low-Q issues of conventional SANS. Consequently, it can measure structures and porous media characteristics at scales ranging from approximately 20 to 2000 nm (Rehm et al., 2012).

In neutron reflectometry, a highly collimated beam of neutrons with wavelength on the order of 2 to 10 Å is used to measure the intensity of reflected radiation as a function of angle or neutron wavelength. The reflectivity profile is then used to test a thin-film structure (Zabel et al., 2000).

2.5.2. Inelastic/quasi-elastic scattering methods

Unlike elastic NS, inelastic NS transfers momentum and energy between the scatterer and the neutrons (Trouw, 1992; Smith and Kneller,

Table 2
Summary of neutron elastic and inelastic scattering methods

Scattering type	Technique	Application and specification	Reference
Elastic	SANS	It applies the elastic NS at small scattering angles to analyze the structure of various compounds at a mesoscopic range of approximately 1–300 nm. It is an inexpensive, noninvasive, easily accessible technique, and requires little sample preparation. If λ is the wavelength of neutrons, and θ is the scattering angle, the scattering variable is defined as $Q = \frac{4\pi}{\lambda} sin\left(\frac{\theta}{2}\right)$. The value of Q usually ranges between 0.001 $Å^{-1}$ and 0.45 $Å^{-1}$. SANS machines are designed for measurements of the scattering object sizes ranging from 1 to 300 nm. For linear sizes ranging from 300 nm to 20 μm, the ultra-small-angle machines (USANS) are designed. In other words, the SANS is applied for analyzing small pores (large θ) while the USANS method is used for investigating large pores (small θ).	Russel et al. (1988), Agamalian et al. (1997), Hainbuchner et al. (2000) Radlinski and Hinde (2001) Wenk (2006)
Elastic	SESANS	It measures structures ranging approximately 20 to 2000 nm in scale. The method provides certain benefits over SANS, but there are fewer SESANS tools usable than SANS.	Rehm et al. (2012)
Elastic	Neutron reflectometry	It is a neutron diffraction method used to test a thin-film structure. The technique offers useful knowledge on a broad variety of scientific and technical uses, including chemical accumulations, polymer and surfactant adsorption, thin-film magnetic structures composition, etc.	Zabel et al. (2000)
Inelastic	Triple-axis spectrometry (TAS)	It enables calculation of the scattering function in physically accessible space of energy and momentum by the spectrometer. Also, a focused (Q, ω) space of interest with a suitable resolution can be investigated using this method. It is mainly used to study single crystal samples.	Hiraka et al. (2020)
Inelastic	Neutron time-of-flight scattering	In this method, the initial location and velocity of the neutron pulse are set, and the final position and time after the pulse required for neutron detections are determined. This information may be used by an experimentalist to determine the energy and momentum transmitted into the sample.	Mamontov and Herwig (2011)
Inelastic	Neutron backscattering	It investigates molecular or atomic motion at a scale of nanoseconds. Monochromator and analyzer backscattering crystals are used to obtain energy resolution of the magnitude of μeV.	Meyer et al. (2003)
Inelastic	Neutron spin echo	The spin-echo spectrometer has an exceptionally high energy resolution (approximately one part in 100,000). Also, it specifies the correlation between densities. One of the possible applications of NSE is the dynamics of spin glasses in hard matter systems	Farago (2006)

1993; Corsaro et al., 2005). These methods can be used to study atomic vibrations and other excitations where atoms are elevated to high energy levels (Melnichenko, 2016).

In the triple-axis spectrometry (TAS) method, three processes produce the three axes of the spectrometer: monochromization, sample interaction, and analyzing. Calculation of the scattering function is enabled by the spectrometer in physically accessible space of energy and momentum (Hiraka et al., 2020). This is mainly used to study single crystal samples.

The Time-of-flight (TOF) technique is used for determining the kinetic energy of a neutron (see relation in Table 1) moving between two fixed points with a given distance. For a beam of neutrons, the higher their kinetic energy the shorter their wavelength (Mamontov and Herwig, 2011).

Neutron backscattering experiments can be performed to study molecular or atomic motion at a scale of nanoseconds. Backscattering refers to the reflection of particles, waves, or signals back in the direction they came from. The main idea for backscattering is using a θ close to 180°.

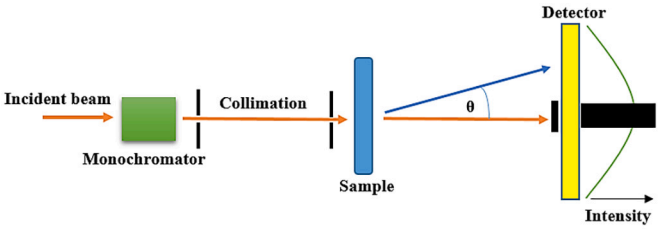

Fig. 5. Schematic of a small-angle neutron scattering system. SANS includes the four measures used in all scattering methods: monochromation, collimation, scattering, and detection. θ is the scattering angle. [Reproduced from Frielinghaus, 2012 with permission from Forschungszentrum Jülich.]

Monochromator and analyzer backscattering crystals are used to obtain energy resolutions between 10^{-3} and 10^{-4} eV (Meyer et al., 2003).

Neutron spin echo (NSE) is another inelastic method that uses the velocity change of neutrons to infer the energy transfer to achieve a high energy resolution (approximately one part in 100,000). One of the possible applications of NSE is to the dynamics of spin glasses in hard matter systems (Farago, 2006). This method has also been used to investigate dynamics of confined water in clays and silica glass (Swenson et al., 2001; Yoshida et al., 2008; Marry et al., 2011).

It is worth noting here that there is a special type of scattering called quasi-elastic NS (QENS) in which the scattering particle can perform some diffusive (translation and rotation) motions (Chen et al., 1982). QENS experiments provide essential information regarding the dynamic properties of fluids in nanopores (Wenk, 2006; Gautam et al., 2017b; Liu et al., 2020).

2.5.3. *Neutron logging method*

Neutron logging is another method where high-energy neutrons bombard the formation. After bombarding the formation by neutrons, they lose energy, where high-energy gamma rays are then produced (Baker et al., 2015; Conner et al., 2017; Mao et al., 2020). A detector measures the gamma rays emitted by neutrons' reactions with formation elements. There are three processes in neutron logging: neutron emission, neutron scattering and neutron absorption. High energy (4.5 MeV) neutrons are emitted from a radioactive source (e.g. americium-beryllium) of the neutron tool, following which they move very fast (fast neutrons), where their energy is related to their speed. The fast neutrally charged neutrons interact with positively charged nuclei of atoms. This interaction is a form of elastic scattering associated with the process of energy transfer from the neutron to the nuclei. The most efficient energy transfer is between the neutron and hydrogen as the neutron has approximately the same mass as hydrogen nuclei. The fast

neutrons lose energy rapidly and slow down, going through stages where they are intermediate neutrons (102 to 105 eV), epithermal neutrons (0.1 to 100 eV), and eventually thermal neutrons (< 0.1 eV). The nuclei of the formation atoms (typically Si, O, Ca, C, Al, Fe) can absorb thermal (and to some extent epithermal) neutrons. Neutron logging tools can measure epithermal neutrons, thermal neutrons and gamma rays emitted during neutron absorption (Baker et al., 2015). Neutron logging is widely used to determine petrophysical properties such as porosity, saturation, and mineralogy (see Section 3.3.4).

2.5.4. Neutron imaging method

Neutron imaging method is to measure the attenuation of the intensity recorded by a 2D camera-type neutron detector. Both reactor and spallation sources can be used for neutron imaging. Neutron transmission radiography (NTR) and neutron computed tomography (NCT), when applied in both research and quality control, can provide information (~ 4 μm spatial resolution with an ongoing effort to reach 1 μm and temporal resolution of milliseconds) about the composition and internal structure of macroscopic geological objects and fluid flow through rock under different pressure and temperature conditions (Middleton et al., 2001; Winkler et al., 2002; El Abd and Milczarek, 2004; de Beer et al., 2004; Schwarz et al., 2005; Vontobel et al., 2005; de Beer and Middleton, 2006; Wilding et al., 2005; Wenk, 2006; Hall, 2013; Kaloyan et al., 2014; Perfect et al., 2014; Melnichenko, 2016; Chiang et al., 2017; Pakhnevich et al., 2018; Oliveira et al., 2019; Tudisco et al., 2019; Zambrano et al., 2019; Tengattini et al., 2020). NTR is a non-destructive and noninvasive 2-dimensional (2D) imaging method based on the attenuation (absorption and scattering) of a neutron beam as it passes through a sample. By taking a series of 2D projection images acquired by rotating the sample (e.g. 0 to 360°) these images can be mathematically correlated to one other, whereby a 3D reconstruction of the object can be made, which can be then classified as NCT. Neutron imaging has broad spectrum of applications in porous media, where it can be used to determine key microstructural properties (e.g. porosity and internal structure) and fluid flow in geomaterials at high pressures and temperatures (see Section 3.3.5).

3. Applications

A wide range of subsurface applications can be investigated using NS. For instance, reservoir or rock evaluation scenarios such as: shale microstructural properties (and the associated impact on hydrocarbon recovery from unconventional reservoirs); structures of microemulsion systems for enhanced oil recovery (EOR); CO_2 and methane adsorption in organic pores (nanopores) for enhanced gas recovery as well as sequestration purposes; which can be investigated by both inelastic and elastic neutron scattering (Alvarez et al., 2009; Grimaldi et al., 2017; Stefanopoulos et al., 2017; Mulder et al., 2019; Neil et al., 2020a, 2020b). Moreover, NS can be used for crystal structure analysis, texture and strain analysis, as well as investigation of other rock and fluid characteristics (e.g. porosity, pore size, connectivity, mineralogy, and phase behaviour of confined reservoir fluids in rock matrix under prevailing pressures and temperatures) [e.g. Pefoute et al., 2017; Zhao et al., 2017a, 2017b, 2017c; Zambrano et al., 2019; Zucali et al., 2020; Neil et al., 2020a, 2020b; Urakawa et al., 2020].

3.1. Crystal structure and mineral analysis

The ability of elastic NS to determine the location of an atomic nucleus is a crucial point for its application in molecular structural analysis of minerals and fluids (Artioli et al., 1993; Bhattacharyya et al., 2006). Several existing studies in the earth science domain have utilised neutrons to analyse the structure of water-containing crystals and minerals (Fitch et al., 1986; Czjzek et al., 1991a, 1991b; Parise et al., 1994; Schofield et al., 1996; Leventouri et al., 2001; Meyer et al., 2001; Swainson and Hammond, 2003; Giustetto and Chiari, 2004; Lennie et al., 2004; Pefoute et al., 2017; Jensen, 2018; Carvalho et al., 2019; Urakawa et al., 2020).

Recall that a crystal structure is defined as the ordered arrangement of atoms, molecules, or ions throughout a crystalline material (Hook and Hall, 1991). The crystal structure analysis of geomaterials is important in geosciences because it provides crucial information about the reservoir, e.g. mineralogy, gas hydrate formation/decomposition kinetics, or how elements are stacked together in a mineral (Wenk, 2006).

Modern electron microscopy can be used to attain atomic resolution (Kogure, 2013; Song et al., 2020). However, X-rays or NS methods are required to acquire more specific and analytical knowledge of 3D magnetic structures, spin densities, and 3D atomic structures within crystals. This is of key importance in multi-phase flow through porous media – which highly depends on the spatial dimension, e.g. the percolation threshold is much lower in 3D than in 2D (Stauffer, 1979).

As mentioned above in Section 2.4, X-ray scattering leads to the total distribution of a crystal's electron density; however, the distribution of a crystal's nuclei density and unpaired electron density are obtained by nuclear NS and magnetic NS, respectively (Young and Wiles, 1982; Artioli et al., 1993; Berry and James, 2001). In principle, the structural data such as position, identity, magnetic spin orientations, and thermal vibrations of atoms in the structure from neutron experiments are precise. This is because NS power is independent of the scattering angle and small corrections are required to convert the integrated intensities into structure factors (Wenk, 2012). Structural analysis using neutrons can be completed on either single crystals or powders. However, there are two reasons why powders are increasingly adopted. First, powders are easier to prepare than a single crystal. Additionally, structural phase transitions (resulted from heating/cooling) that destroy single crystals (e.g. due to large thermal expansions) can be easily investigated using powders (Wenk, 2006).

Structural analysis of hydrogen-containing crystals via NS is quite efficient as neutrons have larger total scattering cross sections for hydrogen than X-rays (see Section 2.4 above). For example, gas hydrate formation and decomposition kinetics have been measured via NS, which is important in the context of unconventional fuel resource recovery (Kuhs, 2004), gas storage and transport (Ikeda et al., 1999), and the hydrate gun hypothesis (Kennett et al., 2003). The time–temperature dependency of the decomposition of metastable gas hydrates has been quantified through in-situ experiments (Halpern et al., 2001). NS tests can be conducted at elevated gas pressures (typically 5 to 35 MPa) which prevail in typical gas hydrate formations (Thompson et al., 2006).

Table 3 summarizes some studies on gas hydrate structure using NS. For instance, Kuhs et al. (2004) have used time-resolved neutron diffraction experiments to investigate gas hydrate decomposition. Their results detail the effects of ice perfection on the anomalous preservation of methane gas hydrate, showing that the onset of anomalous preservation occurs with the transformation and annealment of hexagonal ice (I_h) at approximately 240 K (Fig. 6). Everett et al. (2013) have applied low-temperature X-ray powder diffraction to analyze the decomposition kinetics of three methane hydrate samples. Their results identified two temperature ranges of anomalous preservation (Fig. 7), identifying anomalous preservation as beginning at 230 K. Additionally, Everett et al. (2015) have applied high-resolution neutron powder diffraction to examine mixed CO_2–CH_4 gas hydrates.

Furthermore, the Rietveld method has been applied for quantitative analysis of neutron powder diffraction data to ascertain crystal structures of gas hydrates. For instance, Everett (2013) refined phase fractions of hydrate and I_h using GSAS along with EXPGUI. Similarly, Carvalho et al. (2019) have used GSAS for Rietveld refinement to remove contaminant peaks in NS data.

Neutrons can be used to investigate minerals containing light elements such as hydrogen, lithium, and deuterium (e.g. water-containing minerals). They can also be used to determine the exact positions of light elements in the presence of heavy elements like uranium in mineral structures (Berry and James, 2001). Further, some elements in a mineral

structure have nearly the same number of electrons, resulting in very similar scattering power, whereby they are easily distinguished by neutrons (Wenk, 2012). Table 4 illustrates some examples of water-containing minerals studied by neutron powder diffraction, where it is evident from the table that NS application can detect several minerals on all types of rock. A high-pressure (up to 9.3 GPa) study of brucite, $Mg(OD)_2$, as shown in Fig. 8, illustrates its crystal structure. It can be observed from the figure that when pressure increased up to 9 GPa, the D-O hydrogen bond length (shown in Fig. 8) decreased more than 15%. Additionally, the O-D-O angle has been shown to increase from 148° to 156° when the threefold deuterium split-site varied by an increase in pressure (Parise et al., 1994).

In addition to natural zeolite, the structures of benzene (Fitch et al., 1986), xylene [Czjzek et al., 1991a], or aniline [Czjzek et al., 1991b] in zeolite–Y have widespread applications for petroleum refinement and have been investigated using neutron diffraction.

In summary, NS has frequently been used in past studies to determine the structure of water-containing crystals and minerals, albeit the accuracy of these measurements is an area of continuing investigation.

3.2. Texture and strain analysis

Neutron scattering is increasingly used to investigate texture and the associated stress–strain analysis of geomaterials (Walther et al., 1995; Kocks et al., 1998; Nikitin et al., 2004; Hall et al., 2012; Wensrich et al., 2012; Athanasopoulos et al., 2017; Athanasopoulos et al., 2018), as evident in Table 5. This is due in part to the low absorption and high penetration of samples associated with neutrons (Fig. 1b). Another advantage of neutrons is that some intensity corrections are not necessary, especially for minerals with low-angle reflections where intensity corrections for X-rays are crucial (Wenk et al., 1984). Pole figures for two different rock samples, a deformed marble and a quartzite, are shown in Fig. 9. Fig. 9a shows that neutrons have a better distribution pattern than that of X-rays for the sample. This is because instead of surfaces, large volumes are averaged by the neutron diffraction signal (Schafer, 2002; Ghildiyal et al., 1999).

From a fundamental material science and engineering geology perspective, texture and strain refer to the crystallographic preferred orientation (direction of the crystal lattice) and shape or size deformation of a material (direction of anisotropic grains) under applied forces, respectively (Brokmeier, 1997; Brokmeier, 1999; Bhattacharyya et al., 2006). Texture and strain can be considered as fingerprints for the history of the earth because essential information about anisotropies of physical (e.g. elastic, magnetic and thermal) properties (e.g. shape, size, and arrangement of grains and homogeneity) of rock, constituting the crust and upper mantle, are provided using these two parameters (Wenk, 1985; Ertel et al., 1989; Feldmann, 1989; Kocks et al., 1998; Rinaldi, 2002). For example, the elastic properties of the individual components of polymineralic materials has been studied by strain measurements (Allen et al., 1992; Hauk, 1997; Daymond et al., 1997; Daymond et al., 1999; Santisteban et al., 2002; Schafer, 2002; Webster et al., 2002).

The analysis of neutron diffraction texture is based on Bragg's law (Wenk, 2012), conducted either by a steady flux of thermal and cold neutrons at reactors or by pulsed neutrons at spallation sources. The reliability of these techniques have been tested by Wenk (2012) to determine textures on a single sample (Fig. 10a). A key feature of the calcite's texture visible in Fig. 10 is its symmetrical distribution of the neutron pole figure. This is an index of the bulk deformation geometry of calcite. Similar results have been reported in other observations (Wenk, 1991; Walther et al., 1995; Zucali et al., 2020). For instance, the textures of naturally deformed calcite at various depths in the earth's crust were collected by Zucali et al. (2020). This study recognized different texture patterns that may produce unique seismic velocity patterns.

Additionally, by correlating diffraction peak position to variations in the lattice parameter, elastic strains can be interpreted. These strains can then be used to quantify stress using the appropriate elastic stiffness (Brown et al., 2016; Masoomi et al., 2017; Jacob et al., 2018). These stresses are essential in predicting rock failure, rock deformation, and

Table 3
Summary of studies on gas hydrate structure using NS

Sample	Neutron technique	Scattering parameters and features	Key findings	Reference
Tetrahydrofuran (THF) clathrate hydrate (CH)	Time-of-flight neutron diffraction	The neutron structure factor functions S(Q) of the amorphous samples were derived from the collected scattering data. Contaminant peaks were removed from all patterns using their profile fits obtained from Rietveld refinement.	Local water structures in amorphous ices and amorphous clathrate hydrates at in situ conditions are similar. At the pressures and temperatures of amorphization, THF molecules are immobilized in CH amorphs.	Carvalho et al. (2019)
Tetrahydrofuran (THF) clathrate hydrate (CH)	Quasi-elastic neutron scattering	θ ranged from 14° to 132°. For $\lambda = 5$ Å, the energy resolution was $\Delta E \sim 90$ μeV.	A detailed model of the THF dynamics was obtained by combining molecular dynamics and QENS. At each θ, elastic scattering was obtained from the experiments to investigate the structure.	Pefoute et al. (2017)
Three hydrate samples synthesized from hex-agonal ice, liquid water, and gas (CO_2 and CH_4)	Neutron powder diffraction	For $\lambda = 1.333$ Å and 2.665 Å, the separation of the crystal plane ranged from 0.42 Å to 6.18 Å. High Q data were used to resolve the low separation of the crystal plane.	Avrami[a] constants and activation energies were determined for various temperature ranges. The decomposition of methane hydrate and the anomalous preservation[b] effect were studied.	Everett et al. (2013), Everett et al. (2015)
10% propane–methane gas and D_2O ice and liquid water	Neutron powder diffraction	The scattering intensity ratio was calculated using crystallographic models of methane hydrate.	An alternative experimental approach was presented that included the formation of hydrates from ice and liquid water phases (melted ice).	Klapproth et al. (2011)
Two isotopic compositions: CD_4–D_2O and CH_4–D_2O	SANS	S(Q) were converted to the pair correlation functions $g(r)$ using a convolution function.	The local water structure is affected by the presence of hydrate crystallites. For example, melting hydrate is much faster than producing hydrate from a fresh water–gas mixture.	Thompson et al. (2006)
Hydrate with ice (hexagonal ice and cubic ice), liquid water, and gas (CO_2 and CH_4)	Time-resolved neutron diffraction	A high-resolution scanning powder diffractometer ($\lambda = 1.6$ Å) and a high-intensity powder diffractometer ($\lambda = 2.4$ Å) were used for the experiments.	The onset of anomalous preservation occurs with the transforming and annealing of hexagonal ice at approximately 240 K.	Kuhs et al. (2004)

[a] The Avrami equation describes how materials transform from one phase to another at constant temperature. The constants in the equation are the overall rate constant (k), and the Avrami exponent indicative of process mechanism (n).

[b] Gas hydrate anomalous preservation (also known as self-preservation) is related to ice perfection formed during decomposition (Stern et al., 2001). This refers to the slow decomposition of gas hydrate, which is caused when pressure drops below the equilibrium pressure of a gas–ice–hydrate system at temperatures below 271 K (Istomin et al., 2006). This phenomenon is of great theoretical and practical importance, especially for the use of the hydrate-based method in the petroleum industry; e.g., for gas storage and transportation plans.

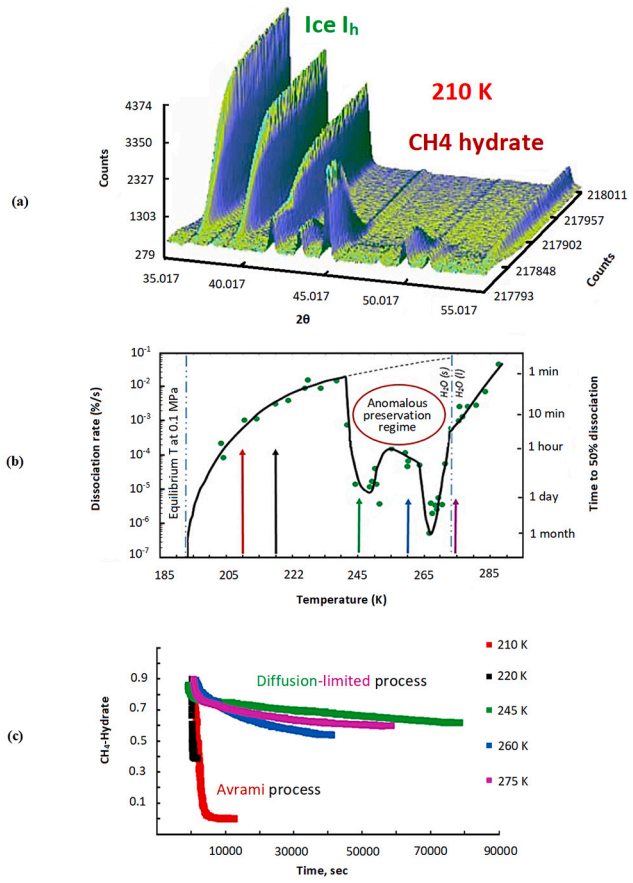

Fig. 6. Decomposition of CH_4 gas hydrates with related anomalous preservation phenomena using neutron diffraction experiments. (a) CH_4 gas hydrate decomposition by decreasing pressure at 210 K. (b) Temperature dependency of the CH_4 gas hydrate decomposition rate showing anomalous preservation area at P = 0.1 MPa (1 bar). (c) Time dependency of CH_4 hydrate decomposition into ice for various temperatures. As a result of the anomalous preservation, the decomposition becomes slow at higher temperatures. [Reproduced from Kuhs et al., 2004 with permission from the Royal Society of Chemistry.]

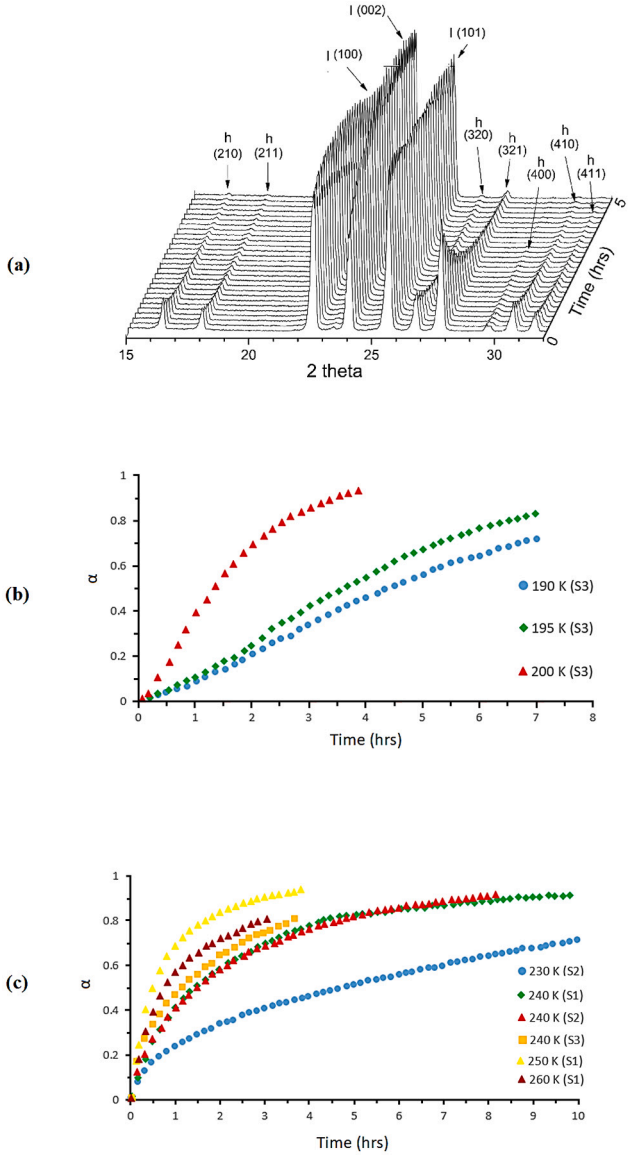

Fig. 7. Decomposition of three CH_4 gas hydrate samples (S_1, S_2, S_3) with related anomalous preservation phenomena using in situ low-temperature X-ray powder diffraction. (a) CH_4 gas hydrates (S_1) decomposition at 250 K. (b) Time dependency of the CH_4 gas hydrate (S_3) decomposition rate for temperature range 190 to 200 K showing anomalous preservation, where α is the weight percent of the converted phase (increasing ice phase). (c) Time dependency of CH_4 gas hydrate (S_1, S_2, S_3) decomposition into ice for temperature range 230 to 260 K. [Reproduced from Everett et al., 2013 with permission from the American Chemical Society.]

fracture strength.

It is evident from Fig. 10a that the position-sensitive detector and time-of-flight (TOF) methods give robust statistics for low diffraction peaks. This is because these two methods determine integrated intensities (area under the peak) rather than peak intensities (e.g., peak height). Further, for TOF tests, the Rietveld approach offers the most efficient study of texture. Similarly, Wenk et al. (2019) have used TOF (analyzed by the Rietveld approach in MAUD) and electron backscatter diffraction (EBSD) methods to analyze textures of quartzite and marble samples. Their results demonstrate that marble may absorb a significant portion of the strain and have local heterogeneities, as expressed in calcite and dolomite pole figures (Fig. 10b).

Abe et al. (2014) have effectively applied an integration of acoustic emission (AE) signal measurements and neutron diffraction to analyze the deformation mechanisms of sandstone and carbonate samples. The effects of an incident neutron beam and gauge volume on the strain of three sandstone samples has also been assessed by Abe et al. (2018). Their results demonstrate that increasing the height of the incident neutron beam can increase the neutron intensity. Additionally, the peak position depends on the rock type instead of the gauge volume height.

There are some important contributions of NS for stress and strain measurements in granular geomaterials (e.g. Hall et al., 2011; Hall et al., 2012; Wensrich et al., 2012; Athanasopoulos et al., 2017; Athanasopoulos et al., 2018; Athanasopoulos et al., 2019). For example, spatially-resolved neutron and X-ray diffractions have been used by Hall et al. (2011) to measure internal strains of sand grains under load and thus, investigate the mechanics of granular media. With these types of measurements, each grain could be thought of as acting as a local (3D) strain gauge. Subsequently, Wensrich et al. (2012) have used a technique based on neutron powder diffraction to produce in-situ mappings of stress distribution in a copper powder die compaction. Exponential decay in axial stress was one of the interesting features observed in this distribution. Similarly, in a new experimental approach, Athanasopoulos et al. (2019) have used a combination of neutron strain scanner (NSS) and digital image correlation (DIC) of quartz sand under load to map the changes of grain strains under the effect of loading and thus, determine the mechanical behaviour of granular media at multiscale. The multiscale analyses included the characterization of the strain field using DIC at mesoscale and the stress distribution using NSS at microscale. A more

Table 4
Examples of water-containing minerals studied by the neutron powder diffraction method

Rock sample	Mineral resolved	Chemical or structural formula	Temperature	Scattering parameters and features	Key findings	Reference
Silicate	Hydrous silica glass	$SiO_2 \cdot nD_2O$	300 K	The time-of-flight (TOF) method under pressure was used for the experiment. The data were obtained at a proton beam power of 300 kW. The neutron structure factor functions S(*Q*) and pair correlation functions *g(r)* were assessed.	Most of D_2O molecules were in the small domains of the D_2O-rich phase and hardly penetrated into the void space in the ring consisting of SiO_4 tetrahedral of SiO_2-rich glass part.	Urakawa et al. (2020)
Carbonate	Amorphous calcium carbonate or amorphous magnesium carbonate	ACC, $CACO_3.nH_2O$ AMC, $CACO_3.nH_2O$	5 to 300 K	The QENS measurement allowed for the *Q* resolved dynamic structure. The measurements were done for $\omega = -0.4$ to 0.4 and $Q =$ 0.42 to 1.85 $Å^{-1}$.	The structural analysis showed that the amorphous phases are well mixed but highly inhomogeneous phase with a broad distribution in coordination numbers around the various species.	Jensen (2018)
Shale	Swelling clay	$[(Mg_{4.92}Fe_{0.44}Al_{0.60}Ti_{0.04})(Si_{5.66}Al_{2.34})O_{20}(OH)_4]M^{+}_{1.64}$	300 K	The SANS with $\lambda = 4.752$ Å was used to extract one dimensional scattered intensity curves I(Q).	A good fit between the experimental and calculated scattering/diffraction profiles were obtained suing the evaluation of the effects of different microstructural parameters on power law exponents.	Ferrage et al. (2018)
Carbonate	Amorphous calcium carbonate	ACC, $CACO_3.nH_2O$	273 to 1,073 K	The neutron PDF data were used for analysis. The simulated pattern based on available molecular dynamic models is quite similar to the PDF data at all wavelengths.	A monohydrocalcite-like local structure moiety was suggested for the resulting d-A(B)CC sample.	Wang et al. (2017)
Silicate	Hydrous wadsleyite	$(Mg, Fe^{2+})_2SiO_4.nH_2O$	100 and 295 K	The time-of-flight (TOF) method was used for the experiments and the datasets were then analyzed using the GSAS program.	The method of hydrogen incorporation into the wadsleyite were qualitatively different from that of its denser polymorph, ringwoodite, in the wet mantle.	Purevjav et al. (2016)
Silicate	Brucite	$Mg(OH)_2$	1,373 K	The powdered neutron diffraction was used for the experiment. The diffraction intensity was normalized and the crystal structure was refined using the Rietveld method.	Hydrogen bonding associated with tilting of the O–D dipole was observed in a layered hydrous silicate mineral under ambient conditions.	Tomioka et al. (2016)
Calcium silicate	Thaumasite	$Ca_3Si(OH)_6(CO_3)(SO_4)\cdot 12H_2O$	300 and 22 K	The numbers of measured reflections were 2,512 at 300 K and 2,825 at 22 K. Also, the applied wavelengths were $\lambda = 0.8381(2)$ Å at both temperatures.	The stability of the structure of thaumasite under non-ambient conditions is mainly governed by the hydrogen-bonding geometry, because all of the major structural units are held together by hydrogen bonds.	Gatta et al. (2012)

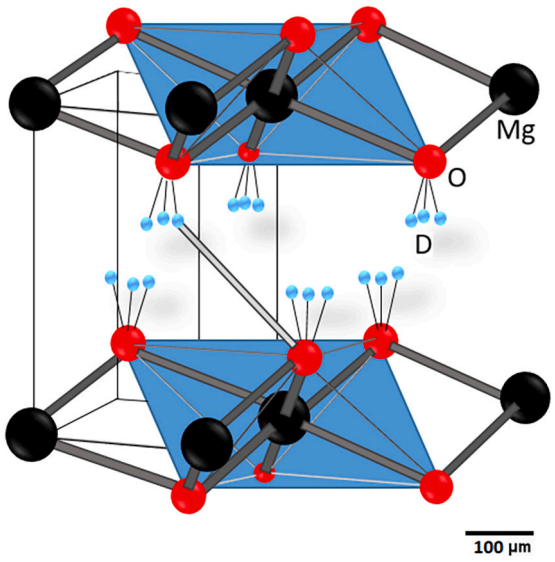

Fig. 8. Crystal structure of brucite, $Mg(OD)_2$. [Reproduced from Parise et al., 1994 with permission from the Mineralogical Society of America.]

detailed description of the loading apparatus can be found in Athanasopoulos et al. (2018).

The relative contribution of all components of rock to a rock's geomechanical properties can be established, as shown in Fig. 11. The figure shows that the elastic strain partitioning curve is independent of composition.

In summary, texture analysis and determination of geomechanical properties such as stress and strain in various geomaterials have become increasingly important applications of NS.

3.3. Rock and fluid characterization

To identify and simulate fluid flow in porous media, a comprehensive insight into pore geometry is required that allows quantification of both the smallest and largest pore-length scales. For instance, porosity is a key parameter for hydrocarbon storage calculation and is a function of pore size and volume. Further, an understanding of the thermodynamic and structural properties of an adsorbed phase (fluid) under various conditions is essential. Neutron scattering is a key and rapidly growing technique for rock and fluid characterization in hydrocarbon and geothermal reservoirs (Wong and Howard, 1986; Radlinski et al., 2000; Radlinski and Hinde, 2001; Radlinski et al., 2002; Radlinski et al., 2004; Alvarez et al., 2009; Melnichenko et al., 2009; Clarkson et al., 2012; Hall, 2013; Bahadur et al., 2014; Perfect et al., 2014; Baker et al., 2015;

Table 5
Summary of studies on texture and strain analysis using NS.

Sample analyzed	Aim	Scattering parameters and features	Key findings	Reference
Marble	Strain	Neutron diffraction measurements of the d-spacing for the sample were obtained at three points on a plane perpendicular to the sample axis, with and without a confining pressure.	Further evaluation of the lattice strains requires identification of the diffraction elastic constants such as Young's moduli and the Poisson ratio.	Carmichael et al. (2020)
Eight limestone and marble samples	Texture/ strain	Quantitative texture analysis was used for the evaluation of the texture of the samples by neutron diffraction. Three different beamlines with different wavelengths (2.52 Å, 0.8 to 2.4 Å, 1.4 to 2.1 Å) were used for the coverage of samples.	Textures of naturally deformed calcite at various depths in the crust were collected, and various texture patterns were recognized that may produce unique seismic velocity patterns.	Zucali et al. (2020)
Forty-seven quartzite and 8 marble samples	Texture	TOF was used for the measurements with $\lambda = 0.2$ to 6 Å by 30 detectors at 2θ to 40°, 90°, and 150°.	The study shows good agreement between neutron diffraction and EBSD.	Wenk et al. (2019)
Granular quartz sand	Stress/ strain	A polychromatic (i.e. wide wavelength) neutron beam dispersing in relation to its TOF from the source was used for the experiment.	The combination of NSS and DIC techniques in a single experimental approach can provide novel insight into the coupled evolution of stress-strain distributions throughout granular media.	Athanasopoulos et al. (2019)
Three sandstone samples	Strain	White-pulsed diffracted neutrons were detected by two detectors at $2\theta = \pm 90°$ to the incident beam.	By increasing the height of the incident neutron beam size, neutron intensity can be increased without introducing pseudostrain. Also, the peak position depends on rock type instead of gauge volume height.	Abe et al. (2018)
Two sandstone and carbonate samples	Strain	Diffraction patterns were measured using the TOF technique. The TOF and d-spacing ranges were 25 to 65 ms and 1.4 to 4.2 Å respectively.	A combination of AE signal measurements and neutron diffraction is a potent tool for analyzing the deformation mechanisms of rock samples.	Abe et al. (2014)
Three samples of eclogite, marble, and artificial rock (MIX) created by seven mineral phases	Texture	Rietveld texture analysis and TOF neutron diffraction were used for MAUD software analysis. In this regard, the peak shape, the crystal lattice parameters, the temperature coefficient, and the phase fractions are useful parameters for Rietveld refinement.	To characterize the texture of a mono-mineralic sample and a four-phase sample, 150 and 350 diffraction spectra respectively are sufficient.	Keppler et al. (2014)
Near spherical monodisperse copper powder	Stress/ strain	Neutrons with $\lambda = 0.22$ nm were used to measure variations in the 200 reflections of the sample under load. The preferred direction of the scan was 45° to the axial direction. The maximum attainable angle for the additional scan was 28° (incident beam obscured at the preferred direction).	The exponential decay in axial stress, a reduction in three normal stress components near the wall, and highly localised regions of high shear stress were interesting features in the stress distribution.	Wensrich et al. (2012)
Three ultramafic samples	Texture/ strain	The wavelength for the used beamline was 1.46 Å. Intensity and localisation corrections and combined analysis were done during the experiment.	Various texture types were identified based on the lattice orientations of olivine. The results also suggest a mantle origin with T >800°C for the activation of slip systems in olivine.	Zucali et al. (2012)
Granular quartz sand	Strain	A Bragg peak at $2\theta \approx 86.8°$ ($\lambda = 1.64$ Å) was measured with a Q-vector (strain measurement direction) along the sample axis.	With such measurements, each grain could be thought of as acting as a local (3D) strain gauge.	Hall et al. (2011)

Mouzakis et al., 2016; Cordonnier et al., 2019; Rezaeyan et al., 2019; Xu, 2019). In comparison with other rock characterization methods, including petrographic analyses, helium pycnometer, gas (CO_2 and N_2) adsorption, and mercury injection capillary pressure (MICP), NS with high penetration power is particularly useful for investigating pores smaller than the intruding molecule (Ruppert et al., 2013). The other associated applications specific to SANS include analyses of effective porosity from pore size, pore connectivity, bulk volume on relatively large samples, and investigation of fluid–rock and fluid–fluid interactions for several fluid pairs (water, oil, CO_2, etc.). These applications and related examples are detailed in the following sections.

3.3.1. Rock characterization

Pore characteristics of rocks, such as porosity, specific surface area (SSA), pore (body and throat) size distribution (PSD), tortuosity, and connectivity can significantly affect the mechanisms of fluid flow and gas storage in geological formations. Amongst varied elastic and inelastic neutron techniques, modern SANS instruments provide access to petrophysical properties in rocks (e.g. structure, size, volume and connectivity of pores) at a mesoscopic scale of approximately 1 to 100 nm (Radlinski et al., 2002; Avdeev et al., 2009; Anovitz et al., 2011; Melnichenko et al., 2009; Clarkson et al., 2013; Ruppert et al., 2013; Bahadur et al., 2015a, 2015b; Bahadur et al., 2016; Melnichenko, 2016; Sun et al., 2017; Yang et al., 2017; Zhao et al., 2017a, 2017b, 2017c; Sun et al., 2019). Also, SANS is a valuable technique for probing both open and closed porosity of shales and confined fluid behaviour at relevant pressure and temperature conditions (Ruppert et al., 2013; Bahadur et al., 2014; Bahadur et al., 2015a, 2015b; Stefanopoulos et al., 2017; Bahadur et al., 2018). These studies on shale rocks are particularly important for evaluating CO_2 geo-storage and enhanced hydrocarbon recovery as these rocks are potential candidate for storage and have low recoveries due to their small porosity and low permeability (Xu, 2019).

3.3.1.1. Scattering length density. A source of scattering (e.g., rock or fluid) has a specific scattering length density (SLD) that adequately explains how well the scattering molecule scatters the incident radiation. The scattering intensity has a contrast term that is defined as the square of the differences in SLD between two sources of scattering. The contrast term is influenced by the strength of the radiation–matter interaction, which depends on averaging all of a pseudomolecule's nuclei. The chemical composition of the pseudomolecule represents the average compositions for each of the two phases of rock: the fluid phase (the pore space content) and the solid phase (the rock matrix) (Wenk, 2006). Eq. (7) can be used to obtain the SLD for every single phase of the pseudo-molar mass (Wenk, 2012):

$$SLD_n = \frac{N_A d}{M} \sum_j P_j \left(\sum_i s_i b_i \right)_j \quad (7)$$

where N_A is Avogadro's number (6.022×10^{23} mol^{-1}), d is grain density (g/cm^3), M is a mineral component molecular weight (g/mol), p_j is phase j's fraction in the matter, b_i is nucleus i's coherent scattering

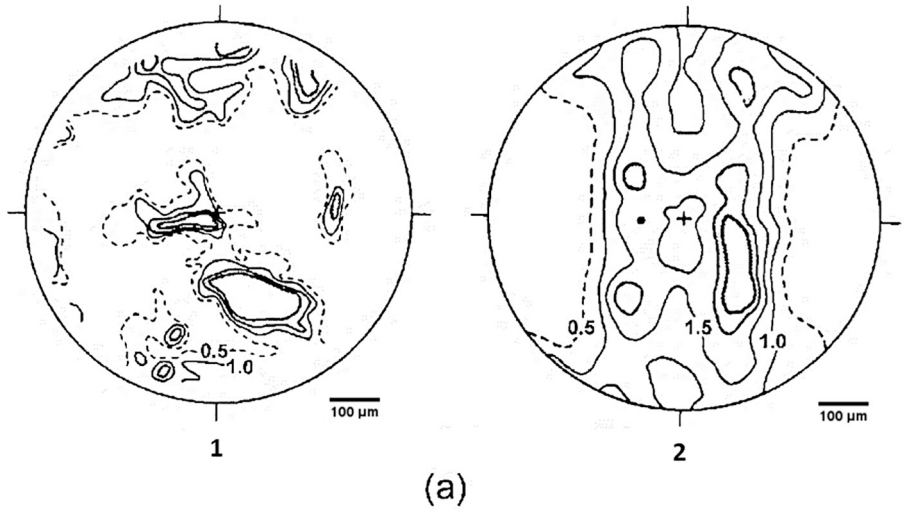

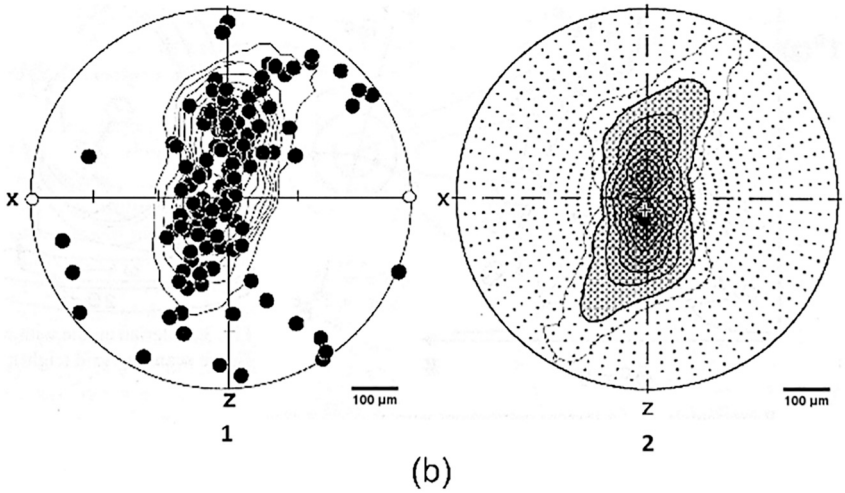

Fig. 9. (a) Pole figures for a coarse-grained deformed marble using X-rays and neutron diffraction for peak 0006 (where neutrons are stronger than X-rays) at $T = 400$ °C and $P = 100$ MPa, 1: determined by X-ray diffraction in reflection geometry, 2: determined by monochromatic neutron radiation. Neutrons have a symmetrical distribution pattern. [Reproduced from Wenk et al., 1984 with permission from Elsevier.] (b) Pole figures for a deformed quartzite using a petrographic microscope and neutron diffraction, 1: determined by a universal stage petrographic microscope over 100 grains, 2: determined by monochromatic neutron radiation in a neutron diffractometer conducted over 1 million grains. Neutrons have better statistics. [Reproduced from Ghildiyal et al., 1999 with permission from the Overseas Publishers Association.]

amplitude, and s_i is nucleus i's abundance in phase j. Table 6 lists the neutron SLDs for specific minerals and organic matter or total organic carbon (TOC) (Bahadur et al., 2014). Fig. 12 graphically presents the values of the neutron SLD for individual inorganic minerals and organic compounds (coals, fractions of crude oil, and pure hydrocarbons). The value of SLDs for organic compounds is primarily determined by the hydrogen-to-carbon ratio as hydrogen and carbon are two dominant elements in organic matter. The average solid-matrix SLD of a rock sample can be obtained by

$$SLD_{rock} = \frac{\sum_1^n vol\%(k)SLD(k)}{100} \tag{8}$$

where k and n refer to a component (e.g., mineral or organic matter) and the total number of components in the rock, respectively (Zhao et al., 2017a, 2017b, 2017c). In cases of rocks comprising organic or inorganic solid matter (e.g., rocks with hydrocarbons, ashy coals), the prevailing scattering contrast is between the pore space and the solid matrix. This is because the neutron contrast between the two solid components of the rock (organic or inorganic) is slight. Therefore, regardless of the content of organic matter, sedimentary rocks are characterized by neutrons as a scattering system with two phases. At the temperature (65-150 °C) and depth (2000-5500 m) of an oil generation window, the solid organic matter within hydrocarbon source rocks will progressively disintegrate into viscous bitumen, then crude oil, and finally break down into light hydrocarbons and gas (Hyne, 2012). This increases volume, leading to primary drainage in which liquid hydrocarbons displace the formation water (Radlinski et al., 2000).

3.3.1.2. Microstructural calculations from SANS/USANS. In SANS and ultra-small-angle neutron scattering (USANS) instrument techniques, the alteration of scattering intensity, $I(Q)$, provides information on the microstructural properties of a rock. The polydispersed spheres (PDSP) model assumes a random spread of spheres with radius r ($V_r = (4/3)\pi r^3$) for the pore system (Radlinski and Hinde, 2001; Liu et al., 2019). The scattering intensity fitted to the PDSP model is given by Eq. (9) (Radlinski et al., 2002):

$$I(Q) = \left(\rho_1^* - \rho_2^*\right)^2 \frac{\phi}{\overline{V_r}} \int_{R_{min}}^{R_{max}} f(r) V_r^2 F_S(Qr) \mathrm{d}r \tag{9}$$

where ρ_1* is the SLD of phase 1 (matrix), ρ_2* is the SLD of phase 2 (pore content), ϕ is the total porosity, $\overline{V_r}$ is the mean pore volume, R_{min} is the minimum pore radius, R_{max} is the maximum pore radius, $f(r)$ is the probability density of the pore size distribution, Q is the scattering variable, and $F_S(Qr)$ is the sphere form factor that is determined as (Zhao et al., 2017a, 2017b, 2017c)

$$F_S(Qr) = 9\left[\frac{sin(Qr) - Qrcos(Qr)}{(Qr)^3}\right]^2 \tag{10}$$

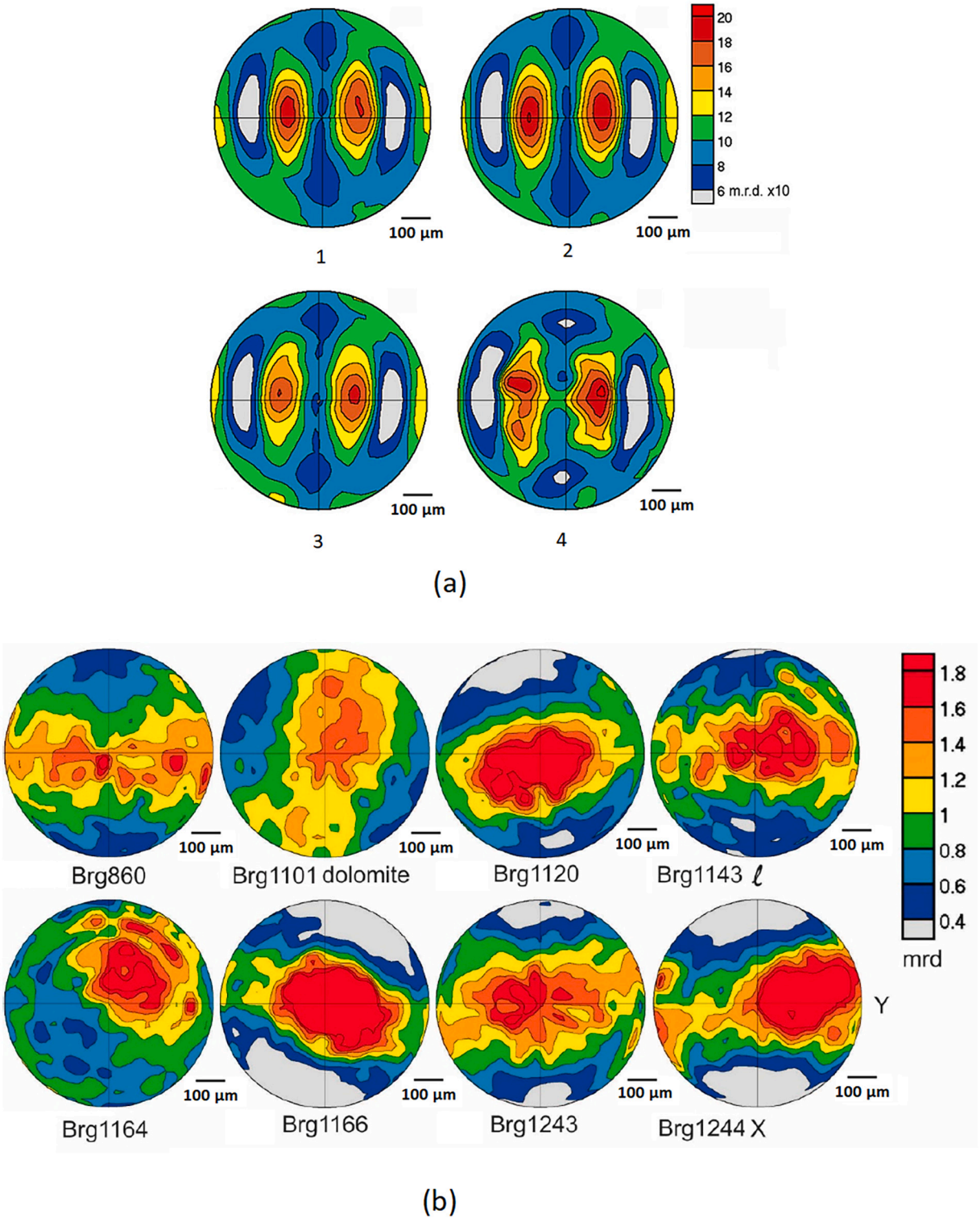

Fig. 10. (a) Polycrystalline calcite 0001 neutron pole figures. A round-robin was applied to test the measurement precision of the neutron diffraction texture. Four different neutron diffraction laboratories were selected for the investigation, 1: monochromatic neutrons at a conventional reactor (Julios at KFA, Jülich), 2: monochromatic neutrons at a reactor with a position-sensitive detector (D1B at Institut Laue-Langevin, Grenoble), 3: TOF tests and single peak extraction at a pulsed reactor (SKAT at Dubna, Russia), 4: spallation neutrons with 30 detectors and OD measured by the Rietveld method (high-pressure preferred orientation at the Los Alamos Neutron Science Center, Los Alamos). [Reproduced from Wenk, 2012 with permission from Springer Nature.] (b) Calcite and dolomite 0001 neutron pole figures for Triassic marbles. All samples were calcite except Brg1101, which was dolomite. Numbers at the top right of the pole figures show which pole density scale was applied (in mrd). [Reproduced from Wenk et al., 2019 with permission from the Multidisciplinary Digital Publishing Institute.]

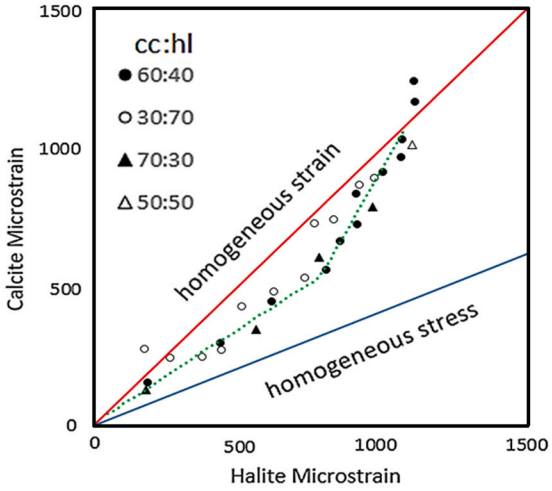

Fig. 11. Calcite and halite axial elastic strains at various applied loads. The elastic limit of the halite is at a halite strain of approximately 350 μstrain. Above a calcite elastic strain of approximately 550 μstrain, the strain partitioning between the two phases starts to tend towards homogeneous elastic strain. [Reproduced from Schafer, 2002 with permission from Copernicus GmbH on behalf of the Deutsche Mineralogische Gesellschaft.]

Table 6
Neutron SLDs for specific minerals and TOC. [Reproduced from Bahadur et al., 2014 with permission from the American Chemical Society.]

Mineral	Formula	Density (g/cm^3)	SANS SLD (10^{10} cm^{-2})	$\sum_i s_i b_i$
Quartz	SiO_2	2.700	4.264	1.5755
Albite	$NaAlSi_3O_8$	2.610	3.950	6.5950
Hematite	Fe_2O_3	5.200	7.156	3.6489
Orthoclase	$KAlSi_3O_8$	2.600	3.710	6.6030
Pyrite	FeS_2	5.000	3.620	1.5234
Carbonates	$CaCO_3$	2.800	3.760	2.2309
Clays	$Al_2Si_2O_5(OH)_4$	2.630	3.160	5.2467
TOC	Coal analogue	1.300	2.500	–

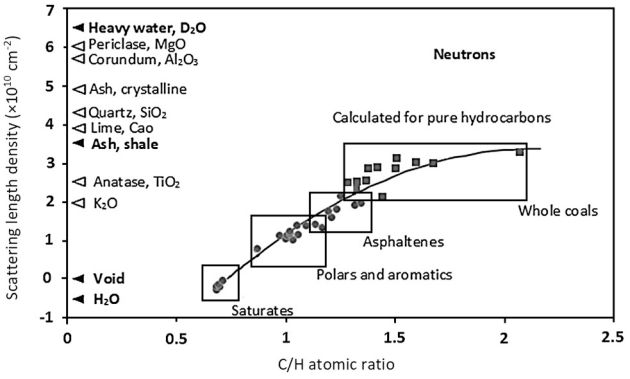

Fig. 12. Neutron SLD for individual inorganic minerals and organic compounds. [Reproduced from Radlinski et al., 2000 with permission from Elsevier.]

The correlation function, $R_z(r)$, is derived from the inverse Fourier transform of $I(Q)$ data as follows (Radlinski et al., 2002):

$$R_z(r) = \frac{1}{2\pi^2(\rho_1^* - \rho_2^*)^2\phi(1-\phi)}\int_0^\infty Q^2 I(Q)\frac{sin(Qr)}{Qr}dQ \quad (11)$$

For pores with radii $>r$, the SSA, $S(r)$, is identified from the pore size distribution (PSD) (Wenk, 2006):

$$\frac{S(r)}{V} = n_v\int_r^{R_{max}} A_r f(r')dr' \quad (12)$$

where $n_v = \phi/\overline{V_r} = I(0)/\left[(\rho_1^* - \rho_2^*)^2\overline{V_r^2}\right]$ is the mean number of pores per unit volume, and $A_r = 4\pi r^2$.

The PSD from the SANS data can be calculated by PRINSAS software using the PDSP model (Hinde, 2004). By adjusting PSD, the software matches the experimental scattering profile via the specified value of SLD for the rock matrix. Using the PDSP model and the Porod invariant (PI) technique, total porosity characterizing the pore space can be identified from the PSD. For a two-phase system, the PI or Q_{inv} is equivalent to (Zhao et al., 2017a, 2017b, 2017c)

$$Q_{inv} = \int_0^\infty Q^2 I(Q)dQ = 2\pi^2(\rho_1^* - \rho_2^*)^2\phi(1-\phi) \quad (13)$$

3.3.1.3. Studies assessment. The microstructures of various sedimentary rocks, such as sandstones, carbonates, and coals, have been characterized using the SANS method (Radlinski and Hinde, 2001; Radlinski et al., 2002; Radlinski et al., 2004; Bahadur et al., 2016). For example, Radlinski et al. (2004) have used a combination of $I(Q)$ data for back-scattering scanning electron microscopy (BSEM), where SANS/USANS were calibrated to the PDSP and Mildner–Hall models (Hall et al., 1983; Mildner and Hall, 1986) in a sandstone sample (Fig. 13a). The fit to the models was evidenced as ideal. However, as shown in Fig. 13b, at larger r these two models do not accurately describe the $R_z(r)$. The SSA and PSD for the sample are also shown in Fig. 13c. Regardless of pore size, the pore body (measured by neutron scattering) to throat size ratio (measured by mercury intrusion porosimetry) was approximately 3.5. Capillary pressures calculated from the Young-Laplace equation, $P_c = 2\sigma cos\theta/r_t$, for surface tension $\sigma = 485$ mN/m, receding contact angle $\theta = 40°$, and pore throat size $r_t = r/3.5$, possessed good compatibility with capillary pressures obtained from experimental mercury intrusion.

However, nanopore structure analysis of shale, when compared to other sedimentary rocks using NS, has recently become more common amongst researchers (Table 7). It is evident that pore characteristics of shale including SSA, PSD, porosity, tortuosity, and connectivity have been investigated using SANS/USANS methods (Table 7).

For SSA analysis, Clarkson et al. (2012) have used the PI method and the PDSP model at ambient conditions to perform/conduct multipoint Brunauer–Emmett–Teller (BET) low-pressure (N_2 and CO_2) adsorption experiments on three samples from a tight gas reservoir. The SSA calculated from gas adsorption was shown to be substantially less than when calculated via the PI method and the PDSP model (Clarkson et al., 2012), which is probably attributable to the limited accessibility of the gases to all pores. Similarly, Yang et al. (2017) have applied the same methods to analyze the SSA in four shale samples of varying mineralogy and organic content. The SSA values of the PDSP model were slightly higher than those of the PI method, but lower than those of the N_2 BET analysis (Yang et al., 2017), suggesting disagreement with earlier observations (Clarkson et al., 2012). This shows that although some pore spaces are not accessible to N_2, a significant amount of pores with diameters of <5 nm exist in these shale samples.

For PSD analysis, Clarkson et al. (2013) compared pore volume distributions (dV/dr) using three methods including SANS/USANS, MICP and combined CO_2/N_2 adsorption. Their results showed good agreement between the SANS/USANS and adsorption methods in the overlap region (pore radii ranged in 100–1000 Å). However, disagreement was observed amongst results of PSD from MICP and adsorption tests (Clarkson et al., 2013). This can be attributed to the fact that interconnected pore volume throughout a related pore throat size is equivalent to the incremental mercury volume at a given pressure during a MICP test (Klaver et al., 2015). Similarly, Sun et al. (2017) have demonstrated that there is reasonable agreement amongst SANS, MICP, and gas (N_2 and CO_2) adsorption techniques applied for PSD analysis,

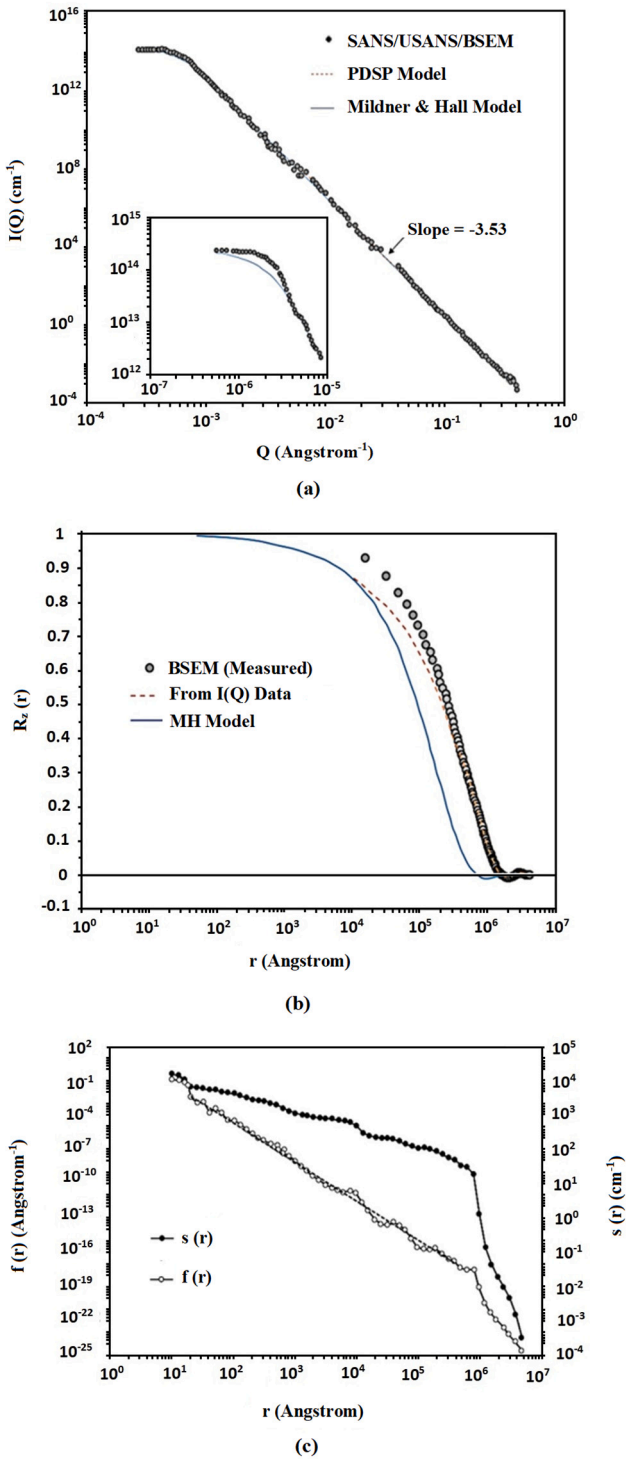

Fig. 13. Microstructure of a sandstone sample investigated with SANS. (a) Experimentally measured SANS scattering intensity, I(Q), and its fit to the PDSP and Mildner–Hall models for a coarse sandstone. (b) Correlation function $R_z(r)$ obtained from integrated SANS/USANS/BSEM models and data. (c) Specific surface area $S(r)$, and pore size distribution, $f(r)$. [Reproduced from Radlinski et al., 2004 with permission from Elsevier.]

indicating the consistency of these methods (Fig. 14). However, analogous to the study by Clarkson et al. (2013), inconsistency between MICP and gas adsorption data in most of the overlap region may exist. It is argued that MICP test tends to overestimate small pores and underestimates large pores in fine-grained rocks (Abell et al., 1999; Dewhurst et al., 1998; Hildenbrand and Urai, 2003). For instance, a peak at approximately 4 nm for the N_2 adsorption data was found (probably due to an artefact caused by the tensile strength effect), but the same result was not evident for SANS (Sun et al., 2017).

In terms of porosity, scattering techniques are extensively applied to evaluate both accessible and closed pores in conventional rocks (Radlinski and Hinde, 2001; Radlinski et al., 2002; Radlinski et al., 2004; Bahadur et al., 2016); however, relatively few studies have utilized SANS in porosity and mineralogy evaluation of shale rocks (Bahadur et al., 2014; Bahadur et al., 2015a, 2015b; Bahadur et al., 2018; Neil et al., 2020a). For example, Bahadur et al. (2015a, 2015b) have compared porosity values obtained using various methods (Table 8). The results of this study demonstrated that porosities calculated by matching the PDSP model to the background-subtracted scattering profile (Q >0.2 Å^{-1}) are more aligned with related helium porosities. This also indicates that porosity values obtained by the PDSP model and PI method for the same Q values (last two columns in Table 8) are similar.

Furthermore, Bahadur et al. (2014) have used SANS/USANS techniques to investigate nano-porosities of three shale samples with different mineral compositions from carbonate-rich to quartz–feldspar rich sources. The authors determined the fractions of closed pores from differences in SANS/USANS porosity (total porosity) and helium pycnometry (open porosity), showing that closed pores had strong correlation with major mineral contents. Most recently, Neil et al. (2020a) have provided SANS porosity measurements under simulated overburden pressures on two clay-rich and carbonate-rich shale samples. The study's results showed that comparing pore accessibility to water in samples (Fig. 15) could be used to estimate the responses of different shales to elevated pressures during hydraulic fracturing operations.

To analyze interpore connectivity, Sun et al. (2017) have used information about closed pores obtained by SANS as well as effective tortuosity obtained by MICP data. The authors showed that geometrical tortuosity L_e/L ratios in effective tortuosity $\tau = (1/\varphi)\,(L_e/L)^2$ (where φ is porosity and L_e and L are actual and straight-line distances between two points respectively, travelled by a fluid molecule) are indices for the connectivity of a porous media. A higher portion of closed porosity would result in increased tortuosity L_e/L ratios, leading to lower flowability or lower matrix permeability (Fig. 16). Similarly, Sun et al. (2019) have studied the multiscale pore connectivity of shale using pore structures distinguished by the SANS method. Their results demonstrate that shale pore connectivity can be directly affected by a change in pore structure. For example, connectivity tends to decrease with decreasing illite crystallinity and increasing maturity.

3.3.2. *Geo-fluids characterization*

Geo-fluids, which often contain substantial amounts of suspended and dissolved compounds including colloids, nanoparticles, organic macromolecules, and complex hydrocarbons, all play a pivotal role in porous media and are crucial sinks and origins of greenhouse gases. The geo-fluids such as brines and those with light C-O-H-N-S species, i.e., H_2, H_2O, CH_4, H_2S, N_2, and CO_2 are of particular interest to petroleum engineering, geoscience, and earth science communities (Wenk, 2006). The fundamental concepts of geo-fluid characterizations include understanding of molecule-scale interactions and how some parameters, such as pressure, temperature, and composition, influence these interactions. Scrutiny of these concepts assists in predicting the phase behaviour of fluids, reactivity, and element partitioning between phases. This can be achieved using advancements in experimental methodologies and instrumentation, with developments in recent simulations of simple and complex geo-fluids. For example, the advent of new generation neutron sources such as the SNS (spallation neutron sources) at Oak Ridge, USA offers significant opportunities for the study of fluids. This can be done by providing more neutrons with improved cost and energy efficiency. Moreover, advanced computing power makes it possible to perform molecular dynamic (MD) simulations of fluids (Steriotis et al., 2004; Corsaro et al., 2005; Melnichenko et al., 2006).

Table 7
Summary of studies on shale microstructure characterization using SANS method

Characteristics analyzed	Rock samples	Scattering features	Key findings	Reference
Porosity and PSD	Two clay-rich and carbonate-rich shale samples	SANS with $\lambda = 5$ Å ($\Delta\lambda/\lambda \sim 0.13$); Q ranging from 0.003 to 0.2 $Å^{-1}$	Shale responses to the elevated pressures during hydraulic fracturing operations can be estimated using SANS measurements.	Neil et al. (2020a)
Connectivity and tortuosity	Four overmature marine shale samples	SANS with $\lambda = 12$ Å and $\lambda = 4.57$ Å ($\Delta\lambda/\lambda \sim 0.15$); Q ranging from 0.001 to 0.5 $Å^{-1}$	Shale pore connectivity can be directly affected by a change in pore structure.	Sun et al. (2019)
Nanoporosity	Three Marcellus shale samples	SANS with Q ranging from 0.002 to 0.3 $Å^{-1}$	The scattering vector range has an impact on measured pore sizes and porosity and pores as small as 2.5 nm were detected.	Bahadur et al. (2018)
PSD, SSA, and porosity	Four organic rich Longmaxi shale samples	SANS (PI method and PDSP model) with $\lambda = 12$ Å and $\lambda = 4.72$ Å ($\Delta\lambda/\lambda \sim 0.15$); Q ranging from 0.001 to 0.5 $Å^{-1}$	Samples with higher TOC content demonstrated greater absolute scattering intensities. Surface area, PSD, and porosity estimated using SANS were larger than those estimated using mercury intrusion porosimetry (MIP).	Yang et al. (2017)
PSD, porosity, SSA, tortuosity, and connectivity	Four Lower Cambrian Niutitang shale samples	SANS with $\lambda = 12$ Å and $\lambda = 4.72$ Å ($\Delta\lambda/\lambda \sim 0.15$); Q ranged from 0.001 to 0.5 $Å^{-1}$.	The results of PSD showed a good agreement between the methods. Also, a higher portion of the closed porosity results in increased geometrical tortuosity ratios (L_e/L), leading to lower flow ability or matrix permeability.	Sun et al. (2017)
Nanoporosity	Five New Albany shale samples	SANS and USANS with $\lambda = 2.4$ Å The porosity was calculated using PI and PDSP methods.	Porosities calculated by matching the PDSP model to the background-subtracted scattering profile ($Q > 0.2$ $Å^{-1}$) were comparable to helium porosities. Also, the porosity values obtained by the PDSP model and PI method for the same Q values (last two columns in Table 8) are similar.	Bahadur et al. (2015a, 2015b)
Nanoporosity	Three cretaceous shale powder samples	SANS and USANS with Q ranged from 0.002 to 0.5 $Å^{-1}$	The fractions of closed pores were determined from differences in SANS/USANS porosity (total porosity) and He pycnometry (open porosity). The closed pores were strongly correlated with major mineral contents.	Bahadur et al. (2014)
PSD, nanoporosity	Seven US shale samples	SANS/USANS (with PDSP model), low-pressure (N_2 and CO_2) adsorption, and high-pressure mercury intrusion	Pore volume distributions derived from SANS/USANS had good compatibility with those from gas adsorption. Moreover, PSD derived from gas adsorption did not agree with mercury intrusion results.	Clarkson et al. (2013)
Surface area, porosity, PSD	Three core plugs from Montney tight gas reservoir	SANS/USANS and low-pressure (N_2 and CO_2) adsorption experiments	Surface area calculated from gas adsorption was substantially less than surface area calculated from SANS/USANS - attributed to limited accessibility of the gases to all pores.	Clarkson et al. (2012)

Neutron scattering provides a framework by which we can investigate the molecular structures and dynamics of fluids, including how fluids interact with solids under various pressure–temperature conditions (Trouw, 1992; Smith and Kneller, 1993; Corsaro et al., 2005; Avdeev et al., 2009; Melnichenko et al., 2009; Bahadur et al., 2016; Benedetto and Ballone, 2018,). This is because unlike X-rays, neutrons have wavelengths and energies that are similar to the frequencies of molecular movements within a sample. Molecular modelling, which includes a numerical solution of the equations of motion for molecules, provides microscopic information regarding experimental outputs resulting from NS techniques. Inelastic spectroscopy, QENS, and SANS are NS techniques that can assess the structural and dynamic properties of geo-fluids (Bellissent-Funel and Teixeira, 1991; Chialvo et al., 1998; Benes et al., 2001; Beta et al., 2003). Incoherent inelastic/QENS are ideal for the study of hydrogen-containing fluids (e.g., water, methane, ethane) due to the large incoherent NS cross section of the hydrogen atom (Bellissent-Funel and Teixeira, 1991; Liu et al., 2020). Moreover, information on scattering density variations (e.g. magnitude and spatial distribution) and gas (e.g., CO_2) adsorption can be obtained from SANS analysis. This is because SANS measures neutron intensities at very low values of the scattering vector, Q (i.e., at small angles). Further, for a two-phase system, SANS intensity is proportional to the contrast term, i.e., the square of the difference in SLD between the two phases (Frisken et al., 1995; Knudsen et al., 2003; Steriotis et al., 2004).

Various geo-fluids have been investigated by NS methods in terms of characteristics such as structure, dynamics, and adsorption, as a function of pressure and temperature (summarized in Table 9).

Methane, one of the most important geo-fluids, has recently been investigated in detail using NS measurements. For example, Chiang et al. (2016) have investigated methane adsorption behaviours on porous silica surfaces using the SANS method. At $T < T_c$ (capillary condensation temperature) = 119 K, the estimated mass densities of confined solid or liquid methane were less than those of corresponding bulk solid or liquid methane. Their theoretical and experimental analysis also showed that at $T > Tc$, SANS patterns were very sensitive to a change in the excess adsorption of methane (Fig. 17). Moreover, recently Neil et al. (2020b) have integrated the SANS method with MD modelling to examine the phase behaviour of methane in shale nanopores at elevated pressures. An increased methane retention in low peak pressure (3,000 psi) drawdown was observed. They also noticed a greater decrease in SANS intensity for this low-pressure scenario – suggesting a higher residual methane in the pore spaces (Fig. 18).

Furthermore, the structure and dynamics of water have been investigated with high accuracy using NS measurements. For example, Bove et al. (2013) have investigated translational and rotational diffusion in water in a GPa range using QENS measurements. The translational diffusion along the 400-K isotherm strongly decreased as pressure increased. However, the rotational diffusion at this isotherm was almost insensitive to pressure (Fig. 19). Similarly, the diffusive (translational and orientational) dynamics of water in carbon nanotubes from 300 K down to 10 K has been investigated using QENS measurements (Briganti et al., 2017). The results indicated: a) an active rotational dynamic for water even at low temperatures and b) good compatibility between translational dynamics and rotational forms. In addition to dynamics, NS techniques provided insights into water structure using the intermolecular pair correlation function (Fig. 20). The pair correlation function $g(r)$, which reflects the structures and dynamics of fluids, is related to the probability of finding the centre of an atom placed at a given distance from the centre of another atom. Water structure analysis have implications for evaluating geomaterials and underground physical and chemical processes (e.g. mantle convection, melting, and the chemistry of melts generated from the earth's mantle).

The structure and adsorption of CO_2, one of the most critical geo-fluids for geo-storage and enhanced hydrocarbon recovery, has been studied using NS measurements. For example, Stefanopoulos et al. (2012) have studied the structure and adsorption of supercritical carbon

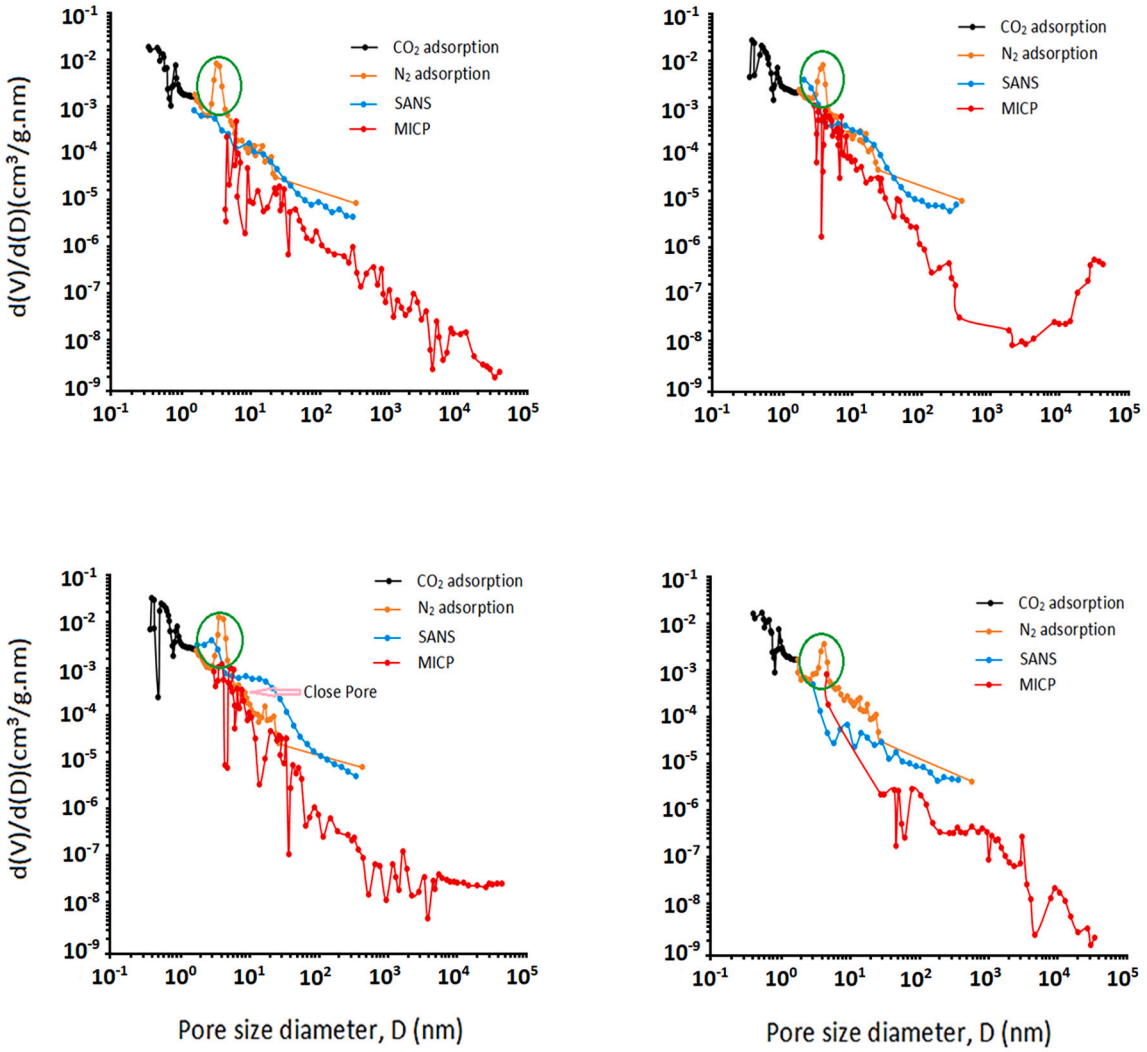

Fig. 14. Distribution of pore volume with pore sizes obtained from gas (CO_2 and N_2) adsorption, MICP, and SANS results for four shale samples. The peak at approximately 4 nm for the N_2 adsorption data is probably due to an artefact caused by the tensile strength effect. [Reproduced from Sun et al., 2017 with permission from Elsevier.]

Table 8
Comparison of porosities measured using different techniques for five samples. [Reproduced from Bahadur et al., 2014 with permission from the American Chemical Society.]

Sample	He porosity (%)	Hg intrusion porosity (%)	PDSP porosity (Q <0.5 Å^{-1}) (%)	PDSP porosity (Q <0.2 Å^{-1}) (%)	PI porosity (%)
1	9.1	5.6	82.8	0.47	0.699
2	4.1	2.7	55.7	4.4	4.05
3	5.1	4.1	55.7	2.64	3.22
4	1.5	0.8	20.4	1.66	1.58
5	3.5	1.4	21.8	1.79	1.92

dioxide in nano-porous silica using neutron diffraction measurements at a temperature slightly above $T_c = 308$ K and a pressure range of 30 to 125 bar. Their results showed that confined CO_2 had liquid-like properties; however, some differences in orientational correlations in pores were related to the confinement of the CO_2 or its strong interactions with the silica walls. Similarly, Bahadur et al. (2015a, 2015b) have investigated high-pressure adsorption behaviour of CO_2 at T = 296 K in microporous carbon, finding that the solvation pressure-induced strain and strong densification of confined CO_2 led to adsorption-induced deformation of micropores. Furthermore, SANS analysis of the phase behaviour of adsorbed CO_2 in a mesoporous silica revealed that by cooling the confined CO_2 below a critical point, fluid molecules escaped from the pores instead of freezing or remaining in a liquid phase (Stefanopoulos et al., 2016).

Hydrogen, as an attractive renewable energy source and geo-fluid for storage, has been examined using NS measurements (Ramirez-Cuesta et al., 2009). For example, Bahadur et al. (2017a, 2017b) have used SANS and inelastic/quasi-elastic methods to investigate the adsorption and diffusive dynamics of hydrogen in ultra-microporous carbon. They observed that the deconvolution of elastic and quasi-elastic signals at 77 K (when bulk H_2 is a gas) provide evidence of pressure-dependent fractions of immobile and partially mobile hydrogen, which can be correlated with excess adsorption (Fig. 21). Further, ethane and propane are two important C-O-H-bearing hydrocarbon geo-fluids that have been investigated using NS measurements. Liu et al. (2020) have investigated the structure and dynamics of ethane confined in silica nanopores in the presence of CO_2 using QENS experiments. Their results suggest stronger adsorption of CO_2 molecules to the pore surface than those of C_2H_6. While Gautam et al. (2017a) have examined the diffusivity of propane in mesoporous silica aerogel using QENS measurements and molecular dynamic simulations. QENS measurements were particularly useful in identifying the origin of anomalous pressure dependent propane

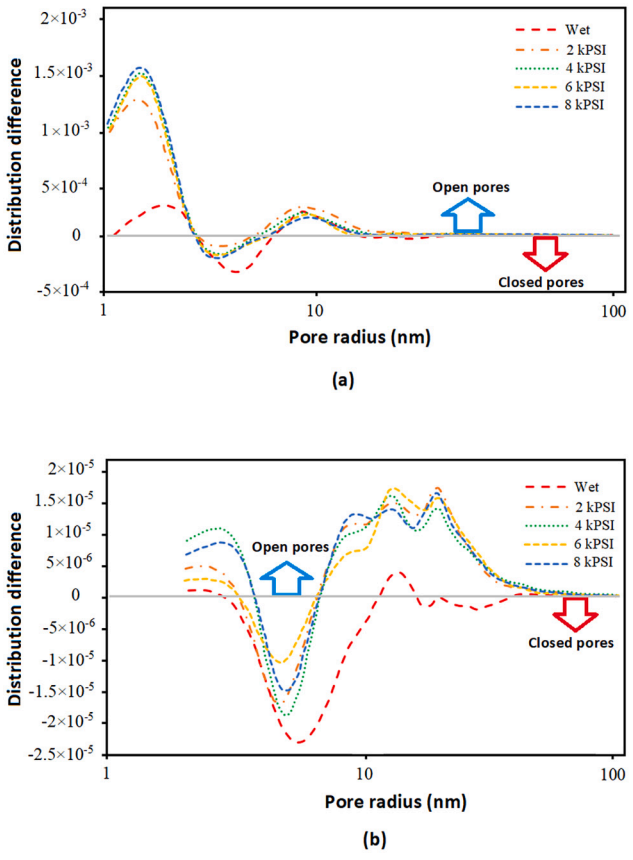

Fig. 15. Differences in pore size distributions for two shales with different mineralogies. (a) Clay-rich shale. (b) Carbonate-rich shale. Note that different curves represent different operating pressures, while red dotted curve represents wet sample. Open pores correspond to positive values while closed pores correspond to negative values of distribution difference. [Reproduced from Neil et al., 2020a with permission from the American Chemical Society.]

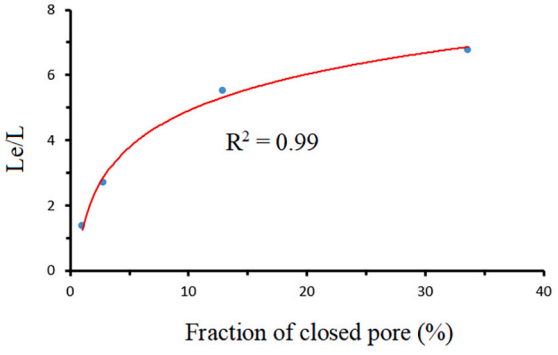

Fig. 16. Variation in the closed-pore fraction with L_e/L ratios. [Reproduced from Sun et al. (2017) with permission from Elsevier.]

diffusivity.

3.3.3. CO_2 geo-sequestration

CO_2 geo-sequestration involves injecting CO_2 into depleted hydrocarbon reservoirs or deep saline aquifers to permanently immobilize CO_2. The key trapping mechanisms that enable CO_2 trapping are structural trapping (Andrew et al., 2014; Iglauer et al., 2015; Arif et al., 2016; Arif et al., 2017; Iglauer, 2018), residual trapping (Iglauer et al., 2019), mineral trapping (Liu and Maroto-Valer, 2011), dissolution trapping (Iglauer, 2011), and adsorption trapping in coals and shales (Arif et al., 2017).

In this context, a quantitative evaluation of the CO_2 trapping capacity of a geological formation is required, which features as a rather challenging task. This task requires precise characterization of the pore system in addition to rock wettability and interfacial tension. Many studies have focussed on investigating pore system characterization (e.g., pore size, porosity, and connectivity) in various potential geological formations using the NS method (Melnichenko et al., 2009; Bahadur et al., 2016; Melnichenko, 2016; Stefanopoulos et al., 2017).

A crucial factor regarding pore systems is accessible and inaccessible porosity, which can be calculated using SANS methods like contrast-matching SANS (CM-SANS) processes (Brumberger, 1995). To calculate accessible and inaccessible pore volume fractions, fluid invasion into pores can be continued until the SLDs of the two components (filling phase and matrix) become the same. This condition is identified as the contrast-matching condition or zero average contrast. In this scenario, high gas pressures of the order of kilobars are required to evaluate accessible and inaccessible porosity through the CM-SANS process, which in turn can influence the morphology of pores at high gas pressure (Pollock et al., 2011).

Melnichenko et al. (2012) have used SANS/USANS techniques to evaluate accessible and inaccessible pore volume fractions of methane and carbon dioxide as a function of pore size in three coals from the Illinois Basin, USA, and the Bowen Basin, Australia. The authors used the relation between scattering intensities and the volume fraction of accessible pores in addition to the relation between real and inverse space dimensions to investigate differences in scattering intensities measured by SANS/USANS techniques at zero average contrast pressure and under vacuum, and determine the variation of the volume fraction of accessible pores as a function of pore sizes in coal samples. Similarly, He et al. (2012) have used SANS/USANS techniques to determine the inaccessible pore volume fraction of methane and carbon dioxide in four bituminous (middle-rank) coals and related this inaccessibility to physical or chemical properties of the coal matrix. Their results demonstrated strong densification, condensation, or both, of the invading subcritical CO_2 in small pores.

Other potential storage reservoirs for CO_2 geo-sequestration are deep saline aquifers. The pore systems of these reservoirs can be analyzed by SANS method to predict storage capacity. For example, Bahadur et al. (2016) have applied a method for determining accessible and inaccessible porosities that do not require the attainment of zero average contrast. The authors took the ratio of intensities at specific values of Q and, by knowing the ratio of their contrasts, the ratio of the fractions of closed and open pores could be obtained. These researchers have shown that scattering intensity rises at a high Q and decreases at a low Q when CO_2 pressure is increased (Fig. 22). This method can be used to determine the fraction of closed and open pores using different fluids such as methane and carbon dioxide at lower pressures.

Shale is another target for CO_2 geo-sequestration (Kang et al., 2010; Levine et al., 2016; Pearce et al., 2018) where large volumes of CO_2 can potentially be rendered immobile via adsorption trapping. For this purpose, SANS measurements can assist in terms of estimating the fraction of pores accessible for CO_2 adsorption. A study by Stefanopoulos et al. (2017) has shown that CO_2 densification occurred within accessible pores at all investigated pore sizes; however, increased Q led to increasingly inaccessible pores. At $Q > 1$ Å^{-1} (radius = 0.25 nm), no accessible pores could be found (Fig. 23). This is because CO_2 molecules with kinetic diameters of 0.33 nm cannot penetrate pores with radii of <0.25 nm. Therefore, despite the abundance of nanopores in shale, they are inaccessible for CO_2 geo-sequestration.

3.3.4. Formation evaluation

Some well-logging tools such as pulsed neutron (PN) and NES are based on NS and are routinely applied for formation evaluation. The neutron-based logs can be used to estimate petrophysical parameters such as porosity, saturation, and lithology. Table 10 summarizes recent

Table 9
Summary of recent studies on geo-fluid characterization using NS techniques

Geo-fluid analyzed	Chemical formula	Characteristics analyzed	Scattering features	Key findings	Reference
Methane	CD_4	Phase behaviour and retention of methane in nanopores	SANS with λ = 6 Å (Δλ/λ~0.13) and *Qs* ranging from 0.003 to 0.43 $Å^{-1;}$ and MD simulation	Increased methane retention was predicted using MD modelling in low (3,000 psi) pressure. Also, as a result of a higher peak pressure, dense or liquid-like methane was trapped in sub-2-nm-radius nanopores.	Neil et al. (2020b)
Methane	CD_4	Adsorption on porous silica surface	SANS with λ = 5 to 6 Å and *Qs* ranging from 0.01 to 0.5 $Å^{-1}$	At T >Tc, SANS patterns were very sensitive to the change in the excess adsorption of methane.	Chiang et al. (2016)
Water	H_2O	Diffusive dynamics (translational and orientational) of water in carbon nanotubes	QENS with λ = 5.1 to 6 Å and *Qs* ranging from 0.38 to 2 $Å^{-1}$ at T = 300 K down to 10 K	The translational dynamic was compatible with the rotational one. There was an active rotational dynamic for water even at low temperatures.	Briganti et al. (2017)
Water	H_2O	Translational and rotational diffusion in water	QENS with *Qs* ranging from 0.4 to 1.4 $Å^{-1}$ translational and rotational diffusion in water in the GPa range.	The translational diffusion strongly decreased with pressure while the rotational diffusion was almost insensitive to pressure.	Bove et al. (2013)
Carbon dioxide	CO_2	Structure, adsorption	Scattered neutrons at *Qs* ranging from 0.02 to 40 $Å^{-1}$ were counted as a function of neutron TOF.	Confined CO_2 had liquid-like properties; however, some differences in orientational correlations in the pores can be related to the confinement of the CO_2 or its strong interactions with the silica walls.	Stefanopoulos et al. (2012)
Carbon dioxide	CO_2	High pressure adsorption	SANS with λ = 4.72 Å (Δλ/λ~0.13) and *Qs* ranging from 0.005 to 1 $Å^{-1}$ at T = 296 K.	The solvation pressure-induced strain and strong densification of confined CO_2 resulted in adsorption-induced deformation of micropores.	Bahadur et al. (2015a, 2015b)
Hydrogen	H_2	Adsorption, diffusive dynamics	SANS and inelastic/quasielastic methods with *Qs* = 1.3 to 30 $Å^{-1}$ that corresponded to wavelengths from 0.2 to 4.2 Å	Deconvolution of an elastic/quasielastic signal at 77 K related fractions of immobile and partially mobile hydrogen to pressure, which can be correlated with the excess adsorption.	Bahadur et al. (2017a, 2017b)
Ethane	C_2H_6	Structure, dynamics in silica nanopores	QENS with λ = 4.8 Å in the presence of CO_2 at different pressures (30, 65, and 100 bar) at 323 K	CO_2 molecules were more strongly adsorbed to the pore surface than C_2H_6 molecules.	Liu et al. (2020)
Propane	C_3H_8	MD simulation	QENS compared to the MD simulation. QENS signal was fitted with the molecular structure factor of the scattering intensity, $S_M(Q)$.	MD simulation supplemented the QENS data to identify the origin of anomalous pressure dependence of propane diffusivity.	Gautam et al. (2017a)

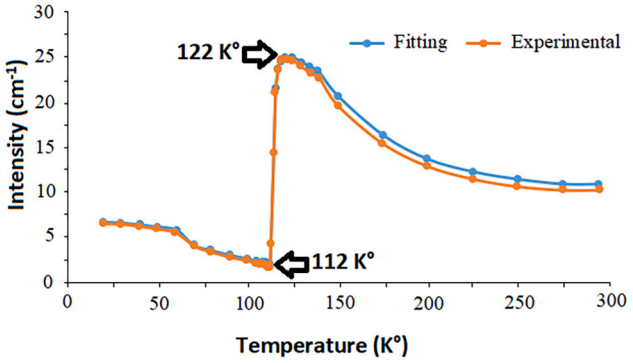

Fig. 17. First-order peak intensity of experimental and fitting data for porous silica material with CD_4 as a function of temperature (loading pressure was approximately 100 kPa and T_c = 119 K). [Reproduced from Chiang et al., 2016 with permission from the American Chemical Society.]

investigations of these logs used for formation evaluation.

A neutron log is sensitive mainly to concentration of hydrogen atoms in formation, where its primary use is in estimating a formation's porosity (Baker et al., 2015). For example, Guo (2019) has developed a porosity measurement using a pulse neutron generator (PNG), and the proposed algorithm used inelastic-to-capture ratio to enhance porosity measurement sensitivity considering borehole effects. The algorithm overcame: 1) the limitation of low sensitivity to formation porosity of traditional neutron logs and 2) the dependency of tools on americium–beryllium (AmBe) and Cf-252 radiological sources that have health and safety problems. Similarly, Mao et al. (2020) have presented a neutron-porosity logging-while-drilling tool using a PNG source, with results showing that the tool could be very helpful in reservoir monitoring and evaluation at high-pressure and high-temperature conditions.

A neutron log can often be affected by the hydrocarbon saturation of a formation. The effect of oil is small as its hydrogen content is similar to that of water. However, since gas has low hydrogen content, this can lead to lower neutron counts and underestimated porosity. Moreover, shale tends to absorb neutrons and therefore has high apparent neutron porosity (Baker et al., 2015).

Another application of a neutron log is to determine fluid saturation. Conner et al. (2017) have used pulsed-neutron-capture (PNC) logs to evaluate oil and gas saturations, with their results revealing PNC logging to be well-suited to CO_2 monitoring (for storage or EOR purposes), where traditional tools could not effectively distinguish between oil, gas, and water in cased CO_2 injection and monitoring wells. Critical factors, such as mud filtrate affecting fluid saturation as calculated by pulse neutron spectral carbon or oxygen logging, have been analyzed by Eltaher et al. (2018), with results demonstrating that saturations from shallow zones may not represent reservoir saturation due to mud filtrate invasion. Further, cement quality, tools used, and other borehole conditions were also shown to potentially affect reservoir saturation monitoring.

The main application of an NES (also known as element capture spectroscopy) log is the identification of precise mineral fractions by converting elemental dry weights to mineral dry weights. For example, Zhao et al. (2017a, 2017b, 2017c) have applied NES logs and an optimization method to solve NES mineral inversion problems. Their results were shown to be in good agreement with XRD data, indicating the robustness and accuracy of the optimization method for mineral inversion based on NES. Similarly, Hosseini (2018) has used NES logs to 1) compensate for the deficiency of logs required for petrophysical modelling, and 2) conduct reliable formation evaluation using accurate mineralogy. The author's results showed that a precise mineralogy using NES logs can influence fluid saturation and porosity.

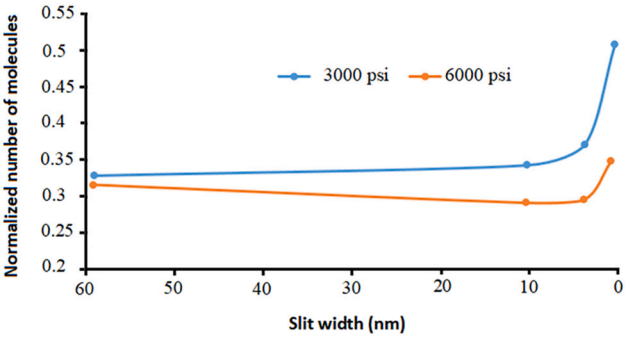

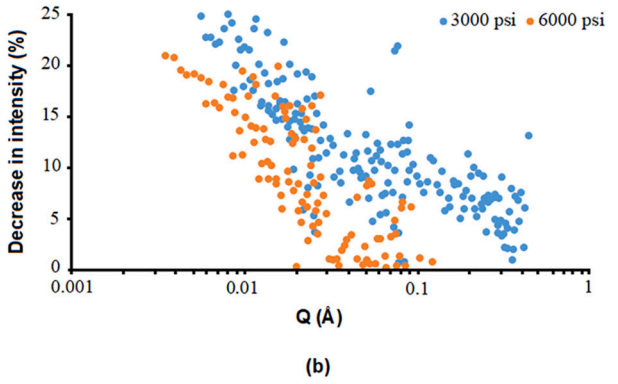

Fig. 18. Molecular modelling results of methane. (a) Molecular dynamics modelling predicts increased methane retention in a low (3,000 psi) pressure drawdown scenario. (b) There is a greater decrease in SANS intensity for the low (3,000 psi) pressure drawdown scenario, indicating that more methane remained in the pore spaces. [Reproduced from Neil et al., 2020b with permission from Springer Nature.]

3.3.5. *Neutron imaging (radiography and tomography)*

Imaging technologies have continually improved our ability to visualize the internal structures of geological objects and fluid flow through rock (Fusseis et al., 2014). In this context, neutron imaging has demonstrated results comparable to X-ray imaging and magnetic resonance imaging (MRI) and the latter still remain subject to some limitations. For example, X-ray imaging differentiates between air and water using tracers; however, this is ideally done by neutrons due to their strong attenuation by hydrogen in water. Moreover, MRI is limited by the presence of iron in a solid matrix, whereas neutrons are relatively insensitive to both fluid in pores and solid constituents, such as iron (Perfect et al., 2014).

One interesting development in tomography techniques has been the improvement in tools enabled by using combined X-ray CT (XCT) and neutron CT (NCT) or by resolution. In this method, neutron and X-ray systems can be placed at perpendicular angles so that a sample sits at the intersection of the beams (Fig. 24), as demonstrated by recent investigations (Sinha et al., 2013a, 2013b; Kaestner et al., 2016; Chiang et al., 2017; LaManna et al., 2017; Chiang et al., 2018; Stavropoulou et al., 2019).

Useful synergies can be found based in similarities and overlaps (e.g. in probing size range) for neutron scattering and imaging methods (Lehmann et al., 2017). For example, Zhou et al. (2016) have shown how neutron scattering and imaging data can be efficiently combined on a scattering vector scale in order to cover an extended size range from microscopic to macroscopic length scales. A review of the application of small angle scattering data in neutron imaging, given by Strobl et al. (2017), similarly underlines the potential of good spatial resolution.

Table 11 summarizes recent studies on subsurface applications of neutron imaging. Neutron imaging provides information about the composition and internal structure of a sample. For example, Kaloyan et al. (2017) have used a neutron tomograph to construct a contrast scale

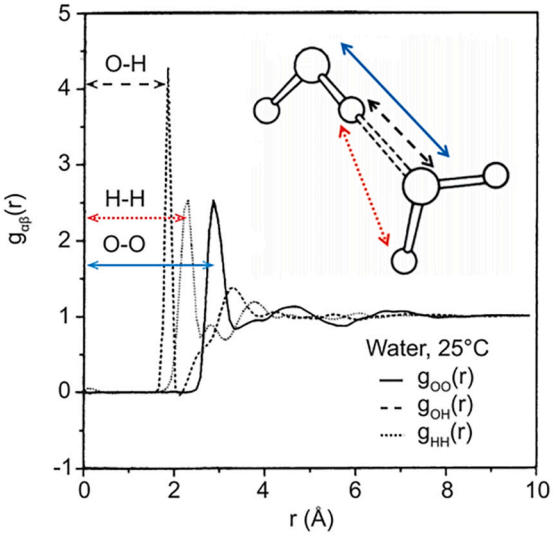

Fig. 20. Partial pair correlation functions for water molecules at 25°C obtained from the NS method. [Reproduced from Amann-Winkel et al., 2016 with permission from the American Chemical Society.]

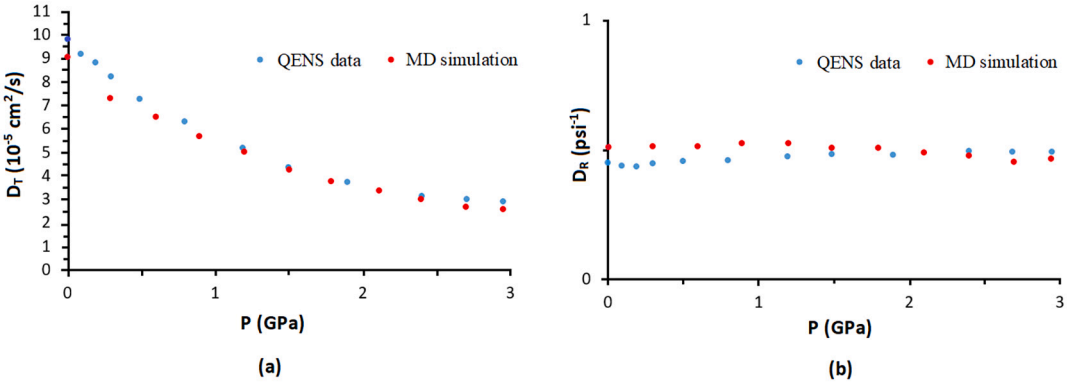

Fig. 19. Pressure dependence of the diffusion coefficients for water along the 400-K isotherm measured by QENS and MD simulations. (a) Translational (D_T). (b) Rotational (D_R). [Reproduced from Bove et al., 2013 with permission from the American Physical Society.]

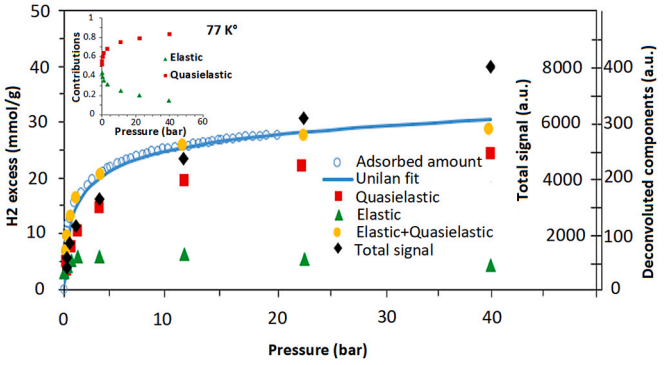

Fig. 21. Comparison of H_2 excess adsorption and deconvoluted component variations with pressure at a 77-K isotherm for elastic, quasi-elastic, and total inelastic NS (INS) signals. [Reproduced from Bahadur et al., 2017a, 2017b with permission from Elsevier.]

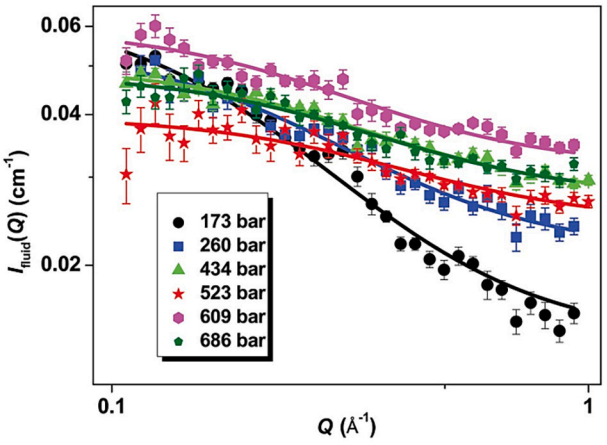

Fig. 22. The scattering intensity $I_{fluid}(Q)$ at various measured pressures. The $I_{fluid}(Q)$ is calculated by deducting the under-vacuum sample scattering profile from the high-pressure SANS profiles. [Reproduced from Bahadur et al., 2016 with permission from the International Union of Crystallography.]

of mineral and rock samples for thermal-neutron tomography. These authors showed that a constructed neutron contrast scale could be used to garner the most detailed information about the internal structure of samples. A simultaneous neutron and X-ray tomography system used by

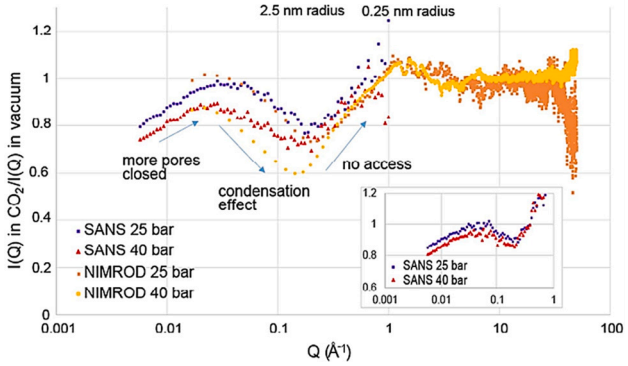

Fig. 23. Comparison of CO_2 scattering intensity ratio at T = 22°C and P = 25 and 40 bar with vacuum conditions (SANS and a near- and intermediate-range-order diffractometer instrument) for Marcellus shale. The flat background is omitted. The inset curve is the same done at T = 60°C. [Reproduced from Stefanopoulos et al., 2017 with permission from the American Chemical Society.]

Table 10
Summary of some recent neutron-based log studies on formation evaluation

Neutron log	Property estimated	Key findings	Reference
PN	Porosity	The tool is helpful in reservoir monitoring and evaluation at high-pressure, high-temperature conditions.	Mao et al. (2020)
PN	Porosity	The algorithm used the inelastic-to-capture ratio to enhance porosity measurement sensitivity considering borehole effects.	Guo (2019)
PN	Saturation	Saturations from a shallow zone may not represent reservoir saturation due to mud filtrate invasion. Also, cement quality, tools used, and other borehole conditions may also affect reservoir saturation monitoring.	Eltaher et al. (2018)
NES	Mineralogy	The precise mineralogy using NES logs had many effects on the values of petrophysical parameters such as fluid saturation and porosity.	Hosseini (2018)
NES	Mineralogy	The results had good agreement with X-ray diffraction data.	Zhao et al. (2017a, 2017b, 2017c)
PN	Saturation	Pulsed-neutron-capture (PNC) logging is a tool for CO_2 monitoring for storage or EOR purposes.	Conner et al. (2017)

LaManna et al. (2017) has been shown to offer the potential of identification of composition as well as improvements in the strength and durability of concrete. Similarly, Oliveira et al. (2019) have applied a combination of neutron tomography and high-resolution X-ray to investigate the mineralogical heterogeneity of oil reservoir rocks at the pore scale. Their results showed, for the first time, the 3D distribution of asphaltenes and their strong preference for mica grains (Figs. 25 and 26).

Additionally, neutron image techniques have been used to visualize the flow and velocity of fluids in bulk rocks. For example, Cordonnier et al. (2019) have used 2D NTR and 3D NCT to visualize cadmium sorption and transport in limestone samples (Fig. 27). Their results showed the local preferences of hydraulic properties regarding the transportation or adsorption of cadmium in samples. Tudisco et al. (2019) have conducted a flow experiment on a rock sample where in the upper part of the sample, water imbibition was the only active driving force (Fig. 28). They used digital volume correlation to provide full 3D deformation and shear-strain measurements to compare with flow

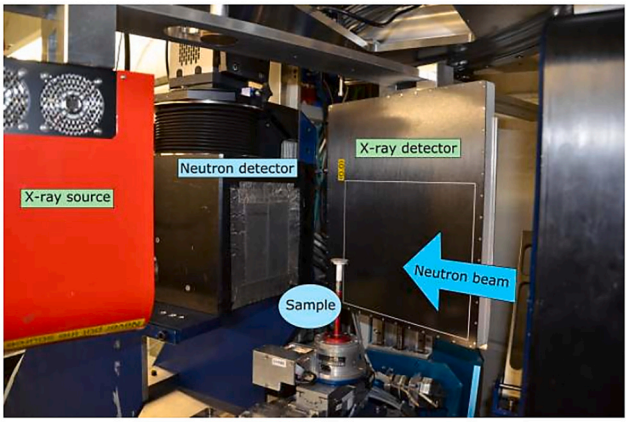

Fig. 24. A combined XCT and NCT. [Reproduced from Kaestner et al., 2016 with permission from Nondestructive Testing (NDT).]

Table 11
Summary of some recent neutron imaging studies on subsurface applications

Properties analyzed	Imaging techniques	Neutron features	Key findings	Reference
Composition, internal structure	NCT, XCT	A neutron tomography (neutron beam with $\lambda = 1.56$ Å monochromatized by the reflection from a Cu (111) single crystal)	An experimental scale of neutron contrast for minerals or rock objects was constructed that could be used to get the most detailed information about the internal structures of the samples.	Kaloyan et al., 2017
Composition, internal structure	NCT, XCT	A thermal neutron beam (controlling the geometric blurriness and fluence rate by the neutron imaging facility)	A simultaneous neutron and X-ray tomography system helped to identify the unwanted phases formation and understand how to improve the strength and durability of concrete.	LaManna et al., 2017
Composition, internal structure	NCT, XCT	A cold monochromatic neutron beam (pixel size = 11.2 μm, exposure time = 15 s/projection, $\lambda = 2$ to 6 Å)	The 3D distribution of asphaltenes and their strong preference for the mica grains were shown for the first time by the combined use of neutron tomography and high-resolution X-ray.	Oliveira et al., 2019
Fluid flow	NCT, NTR	A high and very stable neutron flux by the cold neutron source (pixel sizes = 110, 165 μm, exposure time = 0.2 s)	The results obtained for a quick wetting of a rooted soil and subsequent root water uptake. They showed the ability of their method for 3D water uptake modelling.	Tötzke et al., 2017
Fluid flow	NCT, XCT	High-speed neutron tomography (acquisition = 300 projections in 1 min, pixel size = 100 μm)	In situ analysis could be done regarding the local preferences of hydraulic properties of rocks due to mechanical deformation.	Tudisco et al. 2019
Fluid flow	NCT, NTR	Two different neutron sources including a fission type (neutron flux = 1.5×10^{15} n/cm^2/s) and a spallation type (neutron flux = 10^{14} n/cm^2/s)	Local preferences could be imaged of hydraulic properties regarding the transportation or adsorption of cadmium in limestone samples.	Cordonnier et al., 2019
Fluid flow, internal structure	NTR, NCT, XCT	Two-dimensional NTR and 3D NCT (neutron intensity = 1.3×10^7 n/cm^2/s/mA, exposure time = 80 s)	The combination of NCT and XCT provided more information regarding the contribution of effective pore space to fluid flow.	Zambrano et al., 2019

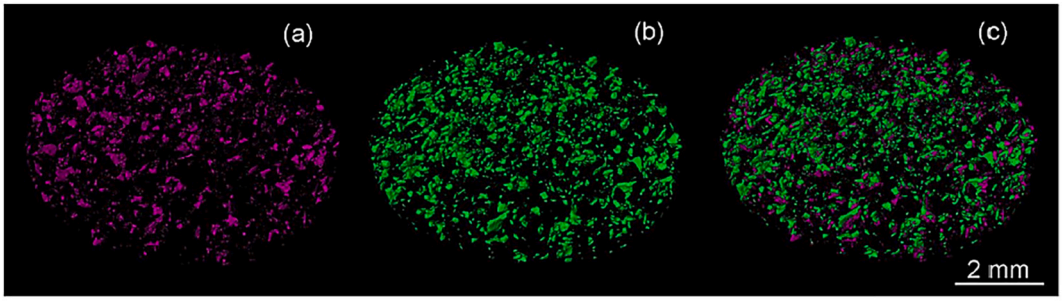

Fig. 25. Interaction of mica grains and crude oil components shown by 3D images of a slab of sandstone rock. (a) Distribution of the mica grains using XCT. (b) Distribution of aggregated asphaltenes in crude oil. (c) Superimposed (a) and (b) to show that the points with good matching suggest a mica–oil interaction. [Reproduced from Oliveira et al., 2019 with permission from Nature Research.]

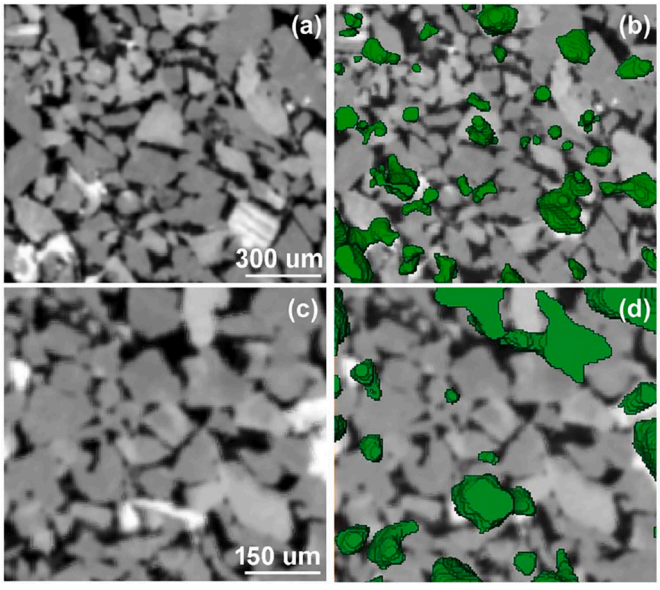

Fig. 26. Mica–asphaltene interactions in pores filled with oil. (a) XCT showing pores. (b) Overlaid (a) by aggregated oil extracted from NCT. (c) Higher magnification of (a). (d) Higher magnification of (b). [Reproduced from Oliveira et al. (2019) with permission from Nature Research.]

measurements. Similarly, Zambrano et al. (2019) have shown that the integrated utilisation of NCT and XCT provides further evidence regarding the effects of effective pore network on fluid flow. These authors simulated fluid dynamics and 3D interpretations of the pore networks using the combined XCT and NCT (Fig. 29). Tötzke et al. (2017) have used high-speed neutron tomography to capture 3D water flow in rooted soil, showing the capability of their method for 3D water uptake modelling.

There are comprehensive review papers that have been published regarding the application of neutron imaging in earth science issues. For example, Perfect et al. (2014) have conducted a review of neutron imaging of hydrogen-rich fluids in geomaterials and engineered porous media. Further, the geomechanical applications of neutron imaging has been comprehensively reviewed by Tengattini et al. (2020).

3.3.6. *Enhanced geothermal systems*

Enhanced geothermal systems (EGSs) are used for extracting heat from porous and permeable geothermal resources. The neutron-based methods (e.g. SANS, USANS, and neutron imaging) have been effectively used to analyze EGSs at different scales (Table 12). For instance, neutron tomographic analyses can help provide 3D images of pore networks and extend scattering curves to lower Q in an even more quantitative manner (Bingham et al., 2015).

Neutron imaging has been used in EGSs to characterize internal structure and fluid flow through rock. For example, Polsky et al. (2013a,

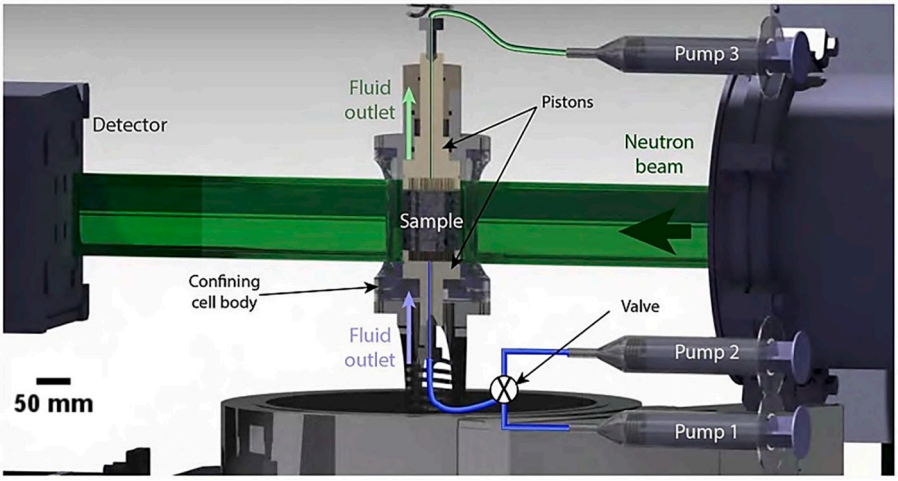

Fig. 27. An experimental setup for NS during injection. A core holder is pressurized with N_2 and is located on the neutron beamline rotary stage. One of the two injection pumps fills the sample from its bottom side. The third pump attached to the top of the sample recovers the fluid. [Reproduced from Cordonnier et al., 2019 with permission from Frontiers Media SA.]

2013b) have used neutron imaging to investigate fluid flow through fractures in EGS-representative conditions. The proof-of-principle measurements of their study included imaging of water–air and H_2O–D_2O flow fronts in addition to measuring the 3D structure of precipitation deposits on fracture surfaces. Using these measurements, the structure of flow moving through a fracture could be quantitatively and qualitatively described. Similarly, Bingham et al. (2015) have applied neutron imaging to test the flow of bubbles of Fluorinert, an electronics coolant liquid, through water-filled cracks under environmental conditions that are found in EGSs. Their results showed that tracking one phase flow through a manufactured crack using a tracking algorithm for correlating the positions of individual bubbles was successful.

Moreover, NS has been applied to characterize rock pore features in EGS reservoirs. For example, Anovitz et al. (2011) have used SANS/USANS techniques to examine the relationship between pore features and water vapour–rock interaction processes in a commercial geothermal system. Their results demonstrated that a vapour-dominated sample of the system had a large fraction of smaller pores with smooth or

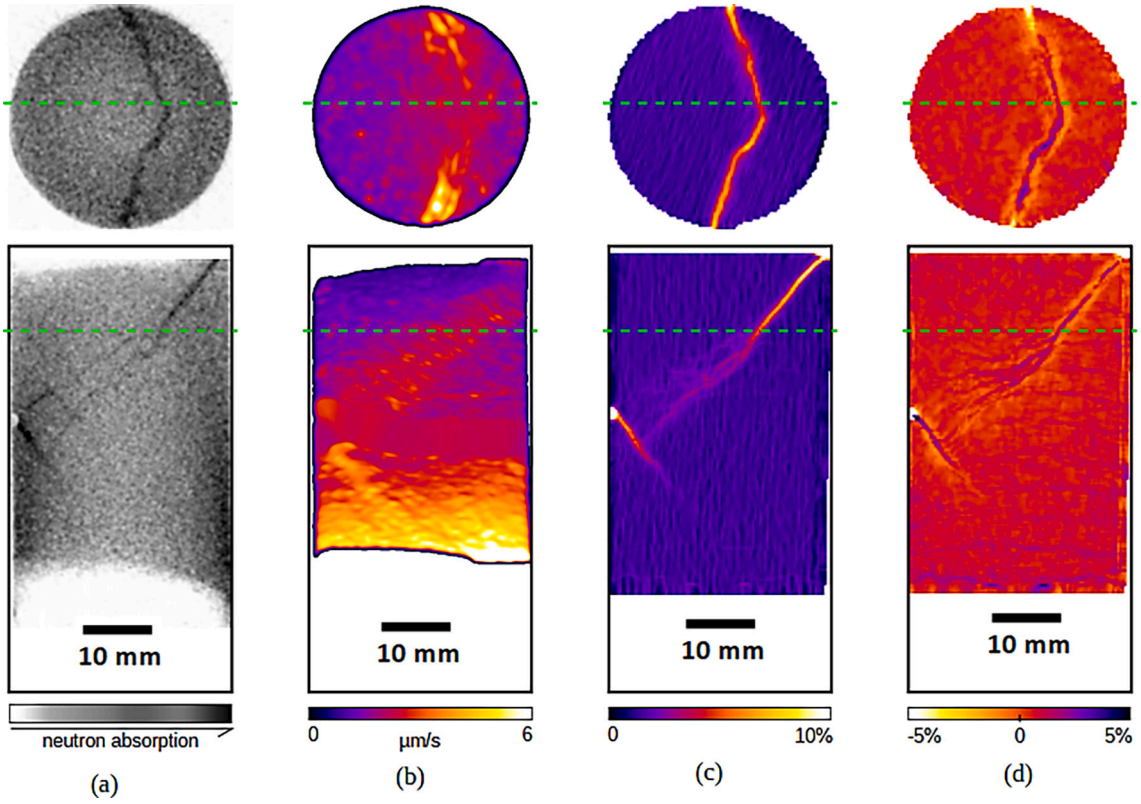

Fig. 28. Vertical and horizontal slices through (a) the neutron tomography image at the end of the flow test, (b) the volume of water speed, (c) the volume of maximum shear strain, and (d) the volume of volumetric-strain (positive values refer to compression). The strain fields were obtained from digital volume correlation used by X-ray tomography taken before and after triaxial deformation. [Reproduced from Tudisco et al. (2019) with permission from the American Geophysical Union.]

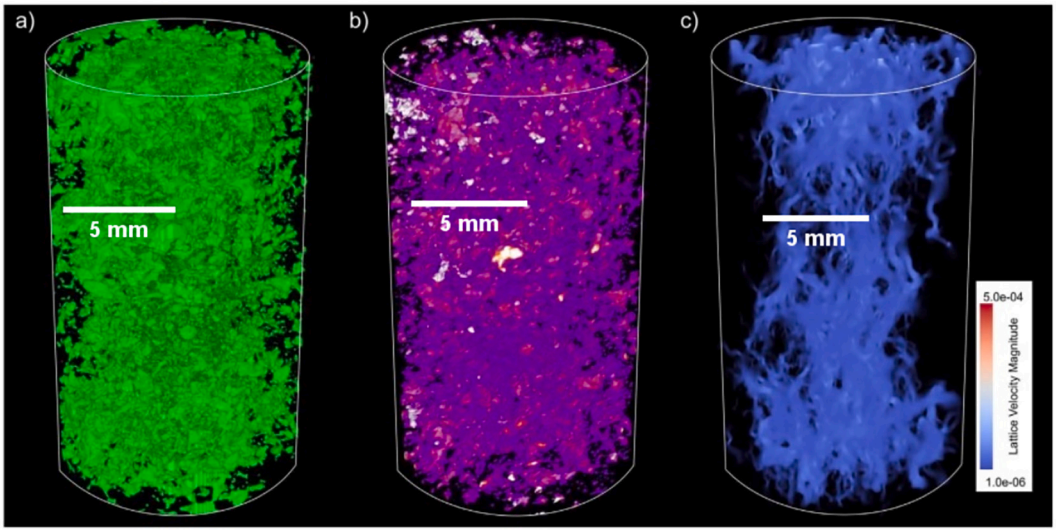

Fig. 29. 3D interpretations of a pore network. (a) XCT. (b) NCT. (c) Velocity image obtained from the Lattice–Boltzmann method. The sample size was 10 mm × 20 mm (diameter × height). The pixel size was set to 13.5 mm. [Reproduced from Zambrano et al., 2019 with permission from Frontiers Media SA.]

fractal pore walls. The overall microporosities of the vapour- and liquid-dominated samples were similar. There were also significant differences in the pore structure of normal (240 °C) and high-temperature (260 to 360 °C) zones. Similarly, Anovitz et al. (2013) have used a combination of NS (SANS/USANS) and imaging analysis to quantify the microporosity of samples from a well, showing that pore morphology provides a detailed statistical description of PSD that can be used to assess enhanced heat extraction in geothermal reservoirs. Moreover, Polsky et al. (2013a, 2013b) have used neutron diffraction-based strain measurement techniques to investigate the internal volumes of sandstone, limestone, and marble geological core samples. Their study effectively provided a better understanding of deformation-related behaviours and hydraulically induced fractures, which can be applied to rock mechanics.

4. Technical limitations

Neutron scattering is the preferred technique for investigating geomaterials and filling fluids due to its unique features i.e. the interactions between neutrons and matter. However, these features can cause some limitations. One of the primary NS limitations is that unlike X-ray sources (synchrotrons), neutron sources (spallation sources using cold-source moderators or nuclear reactors) are characterized by relatively low fluxes and have limitations for observing fast, time-dependent processes. X-rays are often preferred to neutrons to investigate small samples at a very high resolution (El Abd and Milczarek, 2004). In accordance, relatively large samples (typically a diameter of 1 cm and a thickness of 1 mm) are required for SANS tests. Other limitations of NS (some may be also true for other techniques) include problems with: 1) the accessibility of neutron sources (e.g. nuclear processes for neutron

Table 12
Summary of some recent neutron-based studies on EGS.

Experimental conditions	Aim and neutron features	Key findings	Reference
Confinement pressure = up to 69 MPa, flow pressure = 34.5 MPa, temperature = up to 350 °C	Neutron imaging with a tracking algorithm was applied to test the flow of Fluorinert bubbles through water-filled cracks under environmental conditions found in EGS. The thicknesses of the scintillator and exposures of imaging were 150 μm and 10 ms respectively.	Tracking of one phase flow through a manufactured crack in a core sample (1.5-inch diameter) was successful.	Bingham et al. (2015)
Confinement pressure = up to 69 MPa, flow pressure = 34.5 MPa, temperature = up to 350 °C	Neutron imaging was used to investigate fluid flow through fractures in EGS-representative conditions. The thicknesses of scintillator, exposures of imaging, and neutron fluence rate were 100 μm, 10 ms, and 1.4×10^{7} neutrons/cm^2/s respectively.	The proof-of-principle measurements that were successfully done by the system included imaging of the water–air and H_2O–D_2O flow fronts and measuring the 3D structure of precipitation deposits on fracture surfaces.	Polsky et al. (2013a, 2013b)
Confinement pressure = up to 69 MPa, flow pressure = 34.5 MPa, and temperatures = up to 350 °C	Neutron diffraction-based strain measurement techniques were used to interrogate the internal volumes of sandstone, limestone, and marble geological core samples. Neutron chopper settings of 20 Hz and 30 Hz were used to define incident beam wavelengths of 4.32 Å and 2.88 Å respectively.	The study provided a better understanding of deformation-related behaviours and hydraulically induced fractures.	Polsky et al. (2013a, 2013b)
Not reported	A combined NS (SANS /USANS) and imaging analysis was used to quantify microporosity of samples from a well. The *Q* ranges covered by the SANS and USANS techniques were $1*10^{-3}$ to 0.7 Å^{-1} and $4*10^{-5}$ to $1*10^{-3}$ Å^{-1} respectively.	The characterized pore morphology provided a detailed statistical description of the PSD that could be used to understand enhanced heat extraction in geothermal reservoirs.	Anovitz et al. (2013)
Normal-temperature sample = 240 °C, high-temperature sample = 260 °C to 360 °C.	SANS/USANS techniques were used to characterize rock pore features in an EGS reservoir. The *Q* ranges covered by the SANS and USANS techniques were $1*10^{-3}$ to 0.7 Å^{-1} and $4*10^{-5}$ to $1*10^{-3}$ Å^{-1} respectively.	The vapour-dominated sample of the system had a large fraction of smaller pores with smooth or fractal pore walls. The overall submicron porosities of the vapour- and liquid-dominated samples were similar. There were significant differences between the pore structures of the normal and high-temperature zones.	Anovitz et al. (2011)

production); 2) strong absorption of neutron signals by elements like Cd, B, and Gd; 3) low access of neutrons to all transfers of energy and momentum (kinematic restrictions); 4) necessary corrections of instrument effects; and 5) difficulty in interpreting single physical phenomena (Wenk, 2006). It should also be noted here that preparing and maintaining neutron sources involves a very high cost, where operating a nuclear research reactor costs millions of USD annually. Many of these expenses are due to the cost of electricity alone for running a spallation neutron source. One reason why the neutron field has experienced serious setbacks and delays in recent decades is the high operational cost. For example, the Advanced Neutron Source project was cancelled in the mid-1990s because of its high cost, which had amounted to billions of USD (Rush, 2015). Therefore, running successful neutron projects requires considerable support and hosting of large facilities by funding entities.

5. Future work

Whilst real-time in-situ neutron experiments have been developed, there is still large potential for future developments. Future work could include studies of systems using high neutron flux sources. Some of the key areas of future research on applications of NS in petroleum engineering and geoscience fields are summarized below:

1. Spontaneous imbibition of a fluid into a reservoir rock core sample is important to determine displacement characteristics such as wettability, capillary uptake height and rate, and sorptivity. Recently, a few works (e.g. DiStefano et al., 2017; Brabazon et al., 2019; Zhao et al., 2019; Perfect et al., 2020) have considered spontaneous imbibition along fractures using neutron imaging, where further investigations will be required to fully explore this application.
2. Given the recent availability of high flux sources in neutron imaging facilities, the geomaterials and geofluid systems have been (and will be) investigated using these sources (Tengattini et al., 2020). This will facilitate an ongoing effort towards reaching a resolution of 1 μm. To achieve this high flux, a wide *Q* range is required, particularly down to 5×10^{-4} Å^{-1}. This may also make it possible to investigate texture and anisotropy in more detail, even in small samples.
3. In order to achieve superior spatio-temporal resolution in neutron imaging, some developments have been (and will be) considered using the combination with X-ray imaging. Moreover, in order to cover an extended size range, the synergy between neutron scattering and imaging should be further improved.
4. Further investigations will be directed toward conducting more in-situ experiments at high-pressure elevated temperature conditions. For example, until now, the number of studies examining PSD and porosity changes in shale as a function of pressure (Ruppert et al., 2013; Neil et al., 2020a) are very limited. Moreover, SANS studies addressing how cycling pressure affects methane retention and nanopore structure are scarce (Neil et al., 2020b). In addition, there are limited tomographic investigations at elevated temperatures. Tomographic investigations at high-pressure elevated temperature conditions; however, have been applied to date for concrete (Dauti et al., 2018; Yehya et al., 2018).
5. The understanding of rock-fluid inactions and associated interface behaviour (e.g. incorporation of simple molecules in gas hydrates) is important for interpreting the molecular dynamic simulations of interfacial phenomena. Thus, a molecular-level knowledge of how fluids (H_2O, CH_4, CO_2, higher hydrocarbons, etc.) interact with rock at various pressure–temperature conditions needs to be coupled with NS observations –thus constituting an area for future research.
6. Asphaltene deposition and mitigation is another key challenge in the oil and gas industry. Accordingly, the precise characterization of asphaltenes using the SANS/USANS techniques would be interesting/impacting/useful (Knudsen et al., 2020).
7. Finally, further studies are required on the applicability of SANS/USANS methods to investigate EOR processes; e.g., phase changes in oil and brine CO_2 systems at a nanometre scale and their relative permeabilities, and the accurate study of more complicated systems like rocks saturated with brine–gas condensate on low-permeability rock samples and sandy oil reservoirs. Efficient characterization of rocks and fluids by the SANS method would be constructive for more detailed predictive models, which are essential for: primary production, enhanced hydrocarbon recovery, geothermal engineering, and CO_2 sequestration plans.

6. Conclusions

In this paper, the applications of NS techniques in various areas of geosciences (geology, geothermal, environmental, and petroleum engineering) have been critically reviewed. The published datasets suggest that NS is a powerful method for rock and fluid characterization, providing essential information about the structure, texture, rock petrophysical parameters, and phase behaviours of fluids – which in turn underpins reservoir scale applications (e.g. EOR, CO_2 geo-storage, etc.).

More specifically, it can thus be concluded that NS has been frequently used to investigate the crystal structures and minerals, rock texture and the associated geo-mechanical properties – this is attributed to low adsorption and high penetration of neutrons. Furthermore, the data analysed here demonstrate that there is a growing interest in NS applications to resolve rock microstructural features including porosity, pore size and connectivity. In comparison with other rock characterization methods, such as helium pycnometer, gas (CO_2 and N_2) adsorption, and mercury injection capillary pressure (MICP), NS with high penetration power is a very useful method for investigating closed pores (pores smaller than the intruding molecule). This is particularly the case for shale rocks which exhibit microstructural heterogeneities at multiple length scales – thus the inclusion of SANS/USANS in multiscale correlative imaging can help resolve shale microstructure – and in turn contribute towards improved shale reservoir characterization. Notably, previous studies have also applied NS technique for exploring phase behaviour and the associated fluid-fluid and rock-fluid interactions for several geo-fluids including, but not limited to, methane, CO_2, water, crude oil, hydrogen etc.

However, certain challenges do exist in terms of NS applications. For instance, focusing only on samples with small sizes (low signal), low water contents (detrimental scattering effects on detector), and low matrix hydrogen (calibrated for fluid hydrogen) are a few of the technological barriers that need to be accounted for in conducting new configurations and calibrations. In terms of new developments, there is the enhanced desire for increased resolution, which has recently reached close to 4 μm, where there is considerable push to reach 1 μm. In this regard, high flux neutron sources have facilitated the ongoing effort towards reaching a resolution of 1 μm. However, even 1 μm resolution will be insufficient to visualize finer details in nanopores. In this context, resolution in sub-μm range is a target for the NS community, although it is unclear if such an objective will be attained in the near future. One of the recently used techniques to achieve a superior resolution for images is the combination of the neutron with X-ray, where the associated images are likely to be very valuable in studies of multiphase flow and transport.

Furthermore, while the status of NS suggests its effectiveness in several earth science applications, still several questions remained unaddressed, which thus opens various avenues for technological and scientific research in future. For instance, there is a clear lack of data in terms of NS application at high pressure and elevated temperature conditions (e.g., by 3D neutron tomography) to explore rock-fluid interactions at pore-scale and molecular scale, characterize geo-fluids, analyse phase behaviour changes; and characterize asphaltene deposition – which thus constitute areas of future investigation. Moreover, the use of NS for CO_2 and hydrogen studies can also assist towards

geological storage of CO_2 and hydrogen.

In summary, the datasets reviewed here, *albeit* limited, provide sufficient evidence of the effectiveness of NS for a range of applications. Specifically, reservoir and geo-fluid characterization using NS is helpful in making meaningful reservoir scale (hectometre-scale) predictions. These predictions will in turn be beneficial to primary production, enhanced oil and gas recovery, geothermal engineering, H_2 geo-storage and CO_2 sequestration projects.

Declaration of Competing Interest

The authors and their employers have no conflict of interest with other organizations, or with the people working with them.

References

Abdoulghafour, H., Sarmadivaleh, M., Hauge, L.P., Fernø, M., Iglauer, S., 2020. Capillary pressure characteristics of CO_2-brine-sandstone systems. Int. J. Greenhouse Gas Control. 94, 102876.

Abe, J., Sekine, K., Harjo, S., Gong, W., Alizawa, K., 2014. Strain analysis in geological materials using neutron diffraction and AE signal measurement at J-PARC/BL19 "TAKUMI". Mater. Sci. Forum 777, 219–224.

Abe, J., Sekine, K., Harjo, S., Kawasaki, T., Aizawa, K., 2018. Effect of gauge volume on strain measurement in rock materials using time-of-flight neutron diffraction. Phys. B Condens. Matter. https://doi.org/10.1016/j.physb.2018.01.062.

Abell, A.B., Willis, K.L., Lange, D.A., 1999. Mercury intrusion porosimetry and image analysis of cement-based materials. J. Colloid Interface Sci. 211, 39–44.

Agamalian, M., Wignall, G.D., Triolo, R., 1997. Optimization of a bonse-hart ultra-small angle neutron scattering facility by elimination of the rocking-curve wings. J. Appl. Crystallogr. 30, 345–352.

Alao, P.A., Olabode, S.O., Opeloye, S.A., 2013. Integration of seismic and petrophysics to characterize reservoirs in "ALA" oil field, Niger Delta. Sci. World J. https://doi.org/10.1155/2013/421720.

Al-Enezi, H., AlMuhaimeed, I., Al-Mutairi, M., Al-Senafi, M., AlKhalid, A., AlFahad, K., 2018. Designing of a Groundwater Production Scheme for the Northern Oil Fields, Kuwait. In: SPE International Heavy Oil Conference and Exhibition, Kuwait City, Kuwait, December 10-12.

Allen, A.J., Bourke, M.A.M., Dawes, S., Hutchings, M.T., Withers, P.J., 1992. The analysis of internal strains measured by neutron diffraction in Al/SiC metal matrix composites. Acta Metall. Mater. 40, 2361–2373.

Alvarez, G., Jestin, J., Argillier, J.F., Langevin, D., 2009. Small-Angle Neutron Scattering study of crude oil emulsions: Structure of the oil-water interfaces. Langmuir. 25, 3985–3990.

Amann-Winkel, K., Bellissent-Funel, M.C., Bove, L.E., Loerting, T., Nilsson, A., Paciaroni, A., Schlesinger, D., Skinner, L., 2016. X ray and neutron scattering of water. Chem. Rev. 116, 7570–7589.

Anderson, I.S., McGreevy, R.L., Bilheux, H.Z. (Eds.), 2009. Neutron imaging and applications:A reference for the imaging community. Springer.

Andrew, M., Bijeljic, B., Blunt, M.J., 2014. Pore-scale imaging of trapped supercritical carbon dioxide in sandstones and carbonates. Int. J. Greenhouse Gas Control. 22, 1–14.

Anovitz, L.M., Rother, G., Cole, D.R., 2011. Characterization of rock pore features in geothermal systems using Small Angle Neutron Scattering (SANS). In: 36th Workshop on Geothermal Reservoir Engineering, Stanford University, Stanford, California, January 31 – February 2.

Anovitz, L.M., Cole, D.R., Faulder, D.D., Sheets, J., Wang, H.W., Rother, G., Wasbrough, M., Hjelm, R., Hartl, M., Pipich, V., Fu, Z., 2013. Analysis of multiscale porosity a the Cosco geothermal field. In: 38th Workshop on Geothermal Reservoir Engineering, Stanford University, Stanford, California, February 11-13.

Aragón-Aguilar, A., Izquierdo-Montalvo, G., López-Blanco, S., Arellano-Gómez, V., 2017. Analysis of heterogeneous characteristics in a geothermal area with low permeability and high temperature. Geosci. Front. 8, 1039–1050.

Arif, M., Barifcani, A., Lebedev, M., Iglauer, S., 2016. Structural trapping capacity of oil-wet caprock as a function of pressure, temperature and salinity. Int. J. Greenhouse Gas Control. 50, 112–120.

Arif, M., Lebedev, M., Barifcani, A., Iglauer, S., 2017. Influence of shale-total organic content on CO_2 geo-storage potential. Geophys. Res. Lett. 44, 8769–8775.

Arif, M., Mahmoud, M., Zhang, Y., Iglauer, S., 2020. X-ray tomography imaging of shale microstructures: A review in the context of multiscale correlative imaging. Int. J. Coal Geol. 233, 103641.

Artioli, G., Rinaldi, R., Stahl, K., Zanazzi, P.F., 1993. Structure refinements of beryl by single-crystal neutron and X-ray diffraction. Am. Mineral. 78, 762–768.

Athanasopoulos, S.D., Hall, S.A., Pirling, T., Hektor, J., 2017. In-situ grain-strain mapping of quartz sand using neutron diffraction scanning. ALERT Geomaterials Workshop, October.

Athanasopoulos, S.D., Hall, S.A., Kelleher, J.F., Pirling, T., Engqvist, J., Hekto, J., 2018. Mapping grain strains in sand under load using neutron diffraction scanning. https://doi.org/10.1007/978-3-319-99474-1_3.

Athanasopoulos, S.D., Hall, S.A., Kelleher, J.F., 2019. A novel multiscale neutron-diffraction-based experimental approach for granular media. Géotechn. Letters. 9, 284–289.

Avdeev, M.V., Dubois, D., Meriguet, G., Wandersman, E., Garamus, V.M., Feoktystov, A. V., Perzynski, R., 2009. Small-angle neutron scattering analysis of a water based magnetic fluid with charge stabilization: contrast variation and scattering of polarized neutrons. J. Appl. Crystallogr. 42, 1009–1019.

Bahadur, J., Melnichenko, Y.B., Mastalerz, M., Furmann, A., Clarkson, C.R., 2014. Hierarchical pore morphology of cretaceous shale: A Small-Angle Neutron Scattering and Ultra Small-Angle Neutron Scattering study. Energy Fuel 28, 6336–6344.

Bahadur, J., Radlinski, A.P., Melnichenko, Y.B., Mastalerz, M., Schimmelmann, A., 2015a. Small-angle and ultrasmall-angle neutron scattering (SANS/USANS) study of new Albany shale: A treatise on microporosity. Energy Fuel 29 (2), 567–576.

Bahadur, J., Melnichenko, Y.B., He, L., Contescu, C.I., Gallego, N.C., Carmichael, J.R., 2015b. SANS investigations of CO_2 adsorption in microporous carbon. Carbon. 95, 535–544.

Bahadur, J., Medina, C.R., He, L., Melnichenko, Y.B., Rupp, J.A., Blachd, T.P., Mildnere, D.F.R., 2016. Determination of closed porosity in rocks by small angle neutron scattering. J. Appl. Crystallogr. 49, 2021–2030.

Bahadur, J., Contescu, C.I., Rai, D.K., Gallego, N.C., Melnichenko, Y.B., 2017a. Clustering of water molecules in ultramicroporous carbon: In-situ small-angle neutron scattering. Carbon. 111, 681–688.

Bahadur, J., Contescu, C.I., Ramirez-Cuesta, A.J., Mamontov, E., Gallego, N.C., Cheng, Y., Daemen, L.L., Melnichenko, Y.B., 2017b. Properties of immobile hydrogen confined in microporous carbon. Carbon. 117, 383–392.

Bahadur, J., Ruppert, L.F., Pipich, V., Sakurovs, R., Melnichenko, Y.B., 2018. Porosity of the Marcellus Shale: A contrast matching small-angle neutron scattering study. Int. J. Coal Geol. 188, 156–164.

Baker, R.O., Yarranton, H.W., Jensen, J.L., 2015. Practical reservoir engineering and characterization. Elsevier.

Balcewicz, M., Ahrens, B., Lippert, K., Saenger, E.H., 2021. Characterization of fractures in potential reservoir rocks for geothermal applications in the Rhine-Ruhr metropolitan area (Germany). Solid Earth 12, 35–58.

Basavaraj, M.G., Gupta, G.S., 2004. New calibration technique for X-ray absorption in single and multiphase flow in packed beds. ISIJ Int. 44, 50–58.

Bellissent-Funel, M.C., Teixeira, J., 1991. Dynamics of water studied by coherent and incoherent inelastic neutron scattering. J. Mol. Struct. 250, 213–230.

Benedetto, A., Ballone, P., 2018. An overview of neutron scattering and molecular dynamics simulation studies of phospholipid bilayers in room-temperature ionic liquid/water solutions. Phys. B Condens. Matter 551, 227–231.

Benes, N.E., Jobic, H., Verweij, H., 2001. Quasi-elastic neutron scattering study of the mobility of methane in microporous silica. Microporous Mesoporous Mater. 43, 147–152.

Berry, A.J., James, M., 2001. Refinement of hydrogen positions in synthetic hydroxyl-clinohumite by powder neutron diffraction, 86, pp. 181–184.

Beta, I.A., Li, J.C., Bellissent-Funel, M.C., 2003. A quasi-elastic neutron scattering study of the dynamics of supercritical water. Chem. Phys. 292, 229–234.

Bhattacharyya, D., Viswanathan, G.B., Vogel, S.C., Williams, D.J., Venkatesh, V., Fraser, H.L., 2006. A study of the mechanism of a to b phase transformation by tracking texture evolution with temperature in Ti–6Al–4V using neutron diffraction. Scr. Mater. 54, 231–236.

Bingham, P., Polsky, Y., Anovitz, L., Carmichael, J., Bilheux, H., Jacobsen, D., Hussey, D., 2015. Neutron radiography of fluid flow for geothermal energy research. Phys. Procedia 69, 464–471.

Bloch, D., Chaissé, F., Pauthenet, R., 1966. Effects of hydrostatic pressure on the magnetic ordering temperatures and the magnetization of some ionic compounds. J. Appl. Phys. 37 (1401), 1966.

Blume, M., Freeman, A.J., Watson, R.E., 1962. Neutron magnetic scattering from rare earth ions. J. Appl. Phys. 33, 1242.

Blunt, M.J., Bijeljic, B., Dong, H., Gharbi, O., Iglauer, S., Mostaghimi, P., Paluszny, A., Pentland, C., 2013. Pore-scale imaging and modelling. Adv. Water Resour. 51, 197–216.

Bodansky, D., 2004. Neutron reactions. In: Nuclear Energy. Springer, New York, NY. https://doi.org/10.1007/0-387-26931-2_5.

Bove, L.E., Klotz, S., Strassle, Th., Koza, M., Teixeira, J., Saitta, A.M., 2013. Translational and rotational diffusion in water in the GigaPascal range. Phys. Rev. Lett. 111, 185901.

Brabazon, J.W., Perfect, E., Gates, C.H., Santodonato, L.J., Dhiman, I., Bilheux, J.-C., Mckay, L.D., 2019. Spononeous imbibition of a wetting fluid into a fracture with opposing fractal surfaces: Theory and experimental validation. Fractals. 27, 1940001.

Bragg, W.H., Bragg, W.L., James, R.W., Lipson, H., 1934. The crystalline state. MacMillan Company.

Briganti, G., Rogati, G., Parmentier, A., Maccarini, M., De Luca, F., 2017. Neutron scattering observation of quasi-free rotations of water confined in carbon nanotubes. Sci. Rep. 7, 45021.

Brokmeier, H.G., 1997. Neutron diffraction texture analysis. Physica B 234-236, 977–979.

Brokmeier, H.G., 1999. Advances and applications of neutron texture analysis. Text. Microstruct. 33, 13–33.

Brown, D.W., Bernardin, J.D., Carpenter, J.S., Clausen, B., Spernjak, D., Thompson, J.M., 2016. Neutron diffraction measurements of residual stress in additively manufactured stainless steel. Mater. Sci.Eng A. 678, 291–298.

Brugger, R.M., Bennion, R.B., Worlton, T.G., 1967. The crystal structure of bismuth-II at 26 kbar. Phys. Lett. 24A, 714–717.

Brumberger, H., 1995. Modern aspects of Smaii-Angle Scattering. Springer Science+ Business Media, New York, USA. https://doi.org/10.1007/978-94-015-8457-9.

Bust, V.K., 2002. Case studies using reservoir characterization to improve remediation system design and operation. In: SPE Annual Technical Conference and Exhibition, San Antonio, Texas, 29 September-2 October.
Calloway, D., 1997. Beer-lambert law. J. Chem. Educ. 74 (7), 744.
Carmichael, J.R., Polsky, Y., An, K., Anovitz, L.M., Bingham, P., Dessieux, L., Ekici, K., Frost, M., Pemberton, S., 2020. A high-pressure flow through test vessel for neutron imaging and neutron diffraction-based strain measurement of geological materials. Rev. Sci. Instrum. 91, 084502.
Carvalho, P.H.B.B., Mace, A., Bull, C.L., Funnell, N.P., Tulk, C.A., Andersson, O., Häussermann, U., 2019. Elucidation of the pressure induced amorphization of tetrahydrofuran clathrate hydrate. J. Chem. Phys. 150, 204506.
Chadwick, J., 1932. Possible existence of a neutron. Nature. 129, 312.
Chen, S.-H., Teixeira, J., Nicklow, R., 1982. Incoherent quasielastic neutron scattering from water in supercooled regime. Phys. Rev. A 26, 3477–3482.
Chen, Q., Gingras, M.K., Balcomb, B.J., 2003. A magnetic resonance study of pore filling processes during spontaneous imbibition in Berea sandstone. J. Chem. Phys. 119, 9609–9616.
Chialvo, A.A., Cummings, P.T., Simonson, J.M., Mesmer, R.E., Cochran, H.D., 1998. Interplay between molecular simulation and neutron scattering in developing new insights into the structure of water. Ind. Eng. Chem. Res. 37, 3021–3025.
Chiang, W.S., Fratini, E., Baglioni, P., Georgi, D., Chen, J.-h., Liu, Y., 2016. Methane adsorption in model mesoporous material, SBA-15, studied by small-angle neutron scattering. J. Phys. Chem. 120 (8), 4354–4363.
Chiang, W.-S., LaManna, J.M., Katsevich, A., Hussey, D.S., Jacobson, D.L., Frenkel, M., Georgi, D.T., Sun, Q., Liu, Y., Chen, J.-H., 2017. Joint x-ray and neutron tomography of shale cores for characterizing structural morphology. In: International Symposium of the Society of Core Analysts. Vienna, Austria, August 27 – September 1.
Chiang, W.-S., LaManna, J.M., Hussey, D.S., Jacobson, D.L., Liu, Y., Zhang, J., Georgi, D. T., Kone, J.R., Chen, J.-H., 2018. Simultaneous neutron and X-ray imaging of 3D structure of organic matter and fracture in shales. Petrophysics. 59, 153–161.
Choudhury, N., Chaplot, S.L., 2008. Inelastic neutron scattering and lattice dynamics of minerals. Pramana J. Phys. 71, 819–828.
Clarkson, C.R., Freeman, M., He, L., Agamalian, M., Melnichenko, Y.B., Mastalerz, M., Bustin, R.M., Radlinski, A.P., Blach, T.P., 2012. Characterization of tight gas reservoir pore structure using USANS/SANS and gas adsorption analysis. Fuel. 95, 371–385.
Clarkson, C.R., Solano, N., Bustin, R.M., Bustin, A.M.M., Chalmers, G.R.L., He, L., Melnichenko, Y.B., Radlinski, A.P., Blach, T.P., 2013. Pore structure characterization of North American shale gas reservoirs using USANS/SANS, gas adsorption, and mercury intrusion. Fuel. 103, 606–616.
Cohen Stuart, M.A., Cosgrove, T., Vincent, B., 1986. Experimental aspects of polymer adsorption at solid/solution interfaces. Adv. Colloid Interf. Sci. 24, 143–239.
Collins, A.G., Wright, C.C., 1985. Chapter 6 enhanced oil recovery injection waters. Dev. Pet. Sci. 17, 151–221.
Conner, A., Chace, D., Abou-Saleh, J., Kim, Y., McNeil, C., Gerst, J., Kelley, M., Place, M., Pardini, M., Gupta, N., 2017. Developing best practices for evaluating fluid saturations with pulsed neutron capture logging across multiple active CO_2-EOR fields. Energy Procedia 114, 3636–3648.
Cordonnier, B., Pluymakers, A., Tengattini, A., Marti, S., Kaestner, A., Fusseis, F., Renard, F., 2019. Neutron imaging of cadmium sorption and transport in porous rocks. Front. Earth Sci. 7, 1–11.
Cornelissen, G., Kruså, M.E., Breedveld, G.D., Eek, E., Oen, A.M.P., Arp, H.P.H., Raymond, C., Samuelsson, G., Hedman, J.E., Stokland, Ø., Gunnarsson, J.S., 2011. Remediation of contaminated marine sediment using thin-layer capping with activated carbon-A field experiment in Trondheim Harbor, Norway. Environ. Sci. Technol. 45 (14), 6110–6116.
Corsaro, C., Crupi, V., Longo, F., Majolino, D., Venuti, V., Wanderlingh, U., 2005. Mobility of water in Linde type A synthetic zeolites: an inelastic neutron scattering study. J. Phys. Condens. Matter 17, 7925–7934.
Crowley, T.L., 1984. Neutron scattering studies of chemical species. Ph.D. thesis, Oxford University, England.
Czjzek, M., Fuess, H., Vogt, T., 1991a. Structural evidence for π complexes in catalytically active Y zeolites with o-, m-, and p-xylene. J. Phys. Chem. 95, 5255–5261.
Czjzek, M., Vogt, T., Fuess, H., 1991b. Aniline in Yb, Na-Y: A neutron powder diffraction study. Zeolites. 11, 832–836.
Dauti, D., Tengattini, A., Dal Pont, S., Toropovs, N., Briffaut, M., Weber, B., 2018. Analysis of moisture migration in concrete at high temperature through in-situ neutron tomography. Cem. Concr. Res. 111, 41–55.
Daymond, M.R., Bourke, M.A.M., Von Dreele, R.B., Clausen, B., Lorentzen, T., 1997. Use of Rietveld refinement for elastic macrostrain determination and for evaluation of plastic strain history from diffraction spectra. J. Appl. Phys. 82, 1554–1562.
Daymond, M.R., Bourke, M.A.M., Von Dreele, R.B., 1999. Use of Rietveld refinement to fit a hexagonal crystal structure in the presence of elastic and plastic anisotropy. J. Appl. Phys. 85, 739–747.
de Beer, F.C., Middleton, M.F., 2006. Neutron radiography imaging, porosity and permeability in porous rocks. S. Afr. J. Geol. 109, 525–534.
de Beer, F.C., Middleton, M.F., Hilson, J., 2004. Neutron radiography of porous rocks and iron ore. Appl. Radiat. Isot. 61, 487–495.
Dewanckele, J., De Kocka, T., Fronteaub, G., Derluync, H., Vontobeld, P., Dierickx, M., Van Hoorebekee, L., Jacobsa, P., Cnuddea, V., 2014. Neutron radiography and X-ray computed tomography for quantifying weathering and water uptake processes inside porous limestone used as building material. Mater. Charact. 88, 86–99.
Dewhurst, D.N., Aplin, A.C., Sarda, J.P., Yang, Y., 1998. Compaction-driven evolution of porosity and permeability in natural mudstones- An experimental study. J. Geophys. Res. 103, 651–661.
DiStefano, V.H., Cheshire, M.C., McFarlane, J., 2017. Spontaneous imbibition of water and determination of effective contact angles in the Eagle Ford Shale Formation using neutron imaging. J. Earth Sci. 28, 874–887.
Eckold, G., Hagen, M., Steigenberger, U., 1998. Kinetics of phase transitions in modulated ferroelectrics: Time-resolved neutron diffraction from Rb2ZnCl4. Phase Transit. 67 (1), 219–244.
El Abd, A.E.G., Milczarek, J.J., 2004. Neutron radiography study of water absorption in porous building materials: anomalous diffusion analysis. J. Phys. D. Appl. Phys. 37, 2305–2313.
Eltaher, Y., Ma, S., AlNasser, M., 2018. Critical factors affecting pulsed neutron saturation monitoring in carbonate reservoirs. In: SPE kingdom of Saudi Arabia Annual Technical Symposium and Exhibition, Dammam, Saudi Arabia, April 23-26.
Ertel, A., Betzl, M., Kaempf, H., 1989. Texture investigation of natural rock-salt by neutron diffraction. In: Hašek, J. (Ed.), X-ray and neutron structure analysis in materials science. Springer, Boston, MA.
Everett, S.M., 2013. Structural and kinetic studies of structure I gas hydrates via low temperature X-ray diffraction and high resolution neutron diffraction. PhD diss. University of Tennessee, Knoxville. https://trace.tennessee.edu/utk_graddiss/1718.
Everett, S.M., Rawn, C.J., Keffer, D.J., Mull, D.L., Payzant, E.A., Phelps, T.J., 2013. Kinetics of methane hydrate decomposition studied via in situ low temperature X-ray powder diffraction. J. Phys. Chem. A 117, 3593.
Everett, S.M., Rawn, C.J., Chakoumakos, B.C., Keffer, D.J., Huq, A., Phelps, T.J., 2015. Insights into the structure of mixed CO_2/CH_4 in gas hydrates. Am. Mineral. 100, 1203–1208.
Fan, J., Ju, Y., Hou, Q., Wu, Y., Li, X., 2012. Characterization of coal reservoirs in two major coal fields in Northern China: Implications for coalbed methane development. J. Geol. Res. https://doi.org/10.1155/2012/701306.
Farago, B., 2006. Neutron spin echo study of well-organized soft matter systems. Physica B 385-386, 688–691.
Feldmann, K., 1989. Texture investigations by neutron Time-of-Flight diffraction. Text. Microstruct. 10, 309–323.
Ferrage, E., Hubert, F., Baronnet, A., Grauby, O., Tertre, E., Delville, A., Bihannic, I., Pret, D., Michote, L.J., Levitz, P., 2018. Influence of crystal structure defects on the small-angle neutron scattering/diffraction patterns of clay-rich porous media. J. Appl. Crystallogr. 51, 1311–1322.
Fitch, A.N., Jobic, H., Renouprez, A., 1986. Localization of benzene in Sodium-Y zeolite by powder neutron diffraction. J. Phys. Chem. 90, 1311–1318.
Fraiese, A., Cesaro, A., Belgiorno, V., Sanromán, M.A., Pazos, M., Naddeo, V., 2020. Ultrasonic processes for the advanced remediation of contaminated sediments. Ultrason. Sonochem. 67, 105171.
Frielinghaus, H., 2012. Scattering Methods for Condensed Matter Research: Towards Novel Applications and Future Sources. In: Lecture Notes of the 43rd IFF Spring School. Julich, Forschungszentrum. https://www.researchgate.net/publication/259601518.
Frisken, B.J., Cannell, D.S., Lin, M.Y., Sinha, S.K., 1995. Neutron-scattering studies of binary mixtures in silica gels. Phys. Rev. E 51, 5866–5879.
Fusseis, F., Xiao, X., Schrank, C., De Carlo, F., 2014. A brief guide to synchrotron radiation-based microtomography in (structural) geology and rock mechanics. J. Struct. Geol. 65, 1–16.
Gatta, G.D., McIntyre, G.J., Swanson, J.G., Jacobsen, S.D., 2012. Minerals in cement chemistry: A single-crystal neutron diffraction and Raman spectroscopic study of thaumasite, $Ca_3Si(OH)_6(CO_3)(SO_4)\cdot 12H_2O$. Am. Mineral. 97, 1060–1069.
Gautam, S., Le, T., Striolo, A., Cole, D., 2017a. Molecular dynamics simulations of propane in slit shaped silica nano-pores: direct comparison with quasielastic neutron scattering experiments. Phys. Chem. Chem. Phys. 19 (48).
Gautam, S.S., Ok, S., Cole, D.R., 2017b. Structure and dynamics of confined C-O-H fluids relevant to the subsurface: Application of magnetic resonance, neutron scattering, and molecular dynamics simulations. Front. Earth Sci. 5, 43.
Ghildiyal, H., Jansen, E., Kirfel, A., 1999. Volume texture of a deformed quartzite observed with u-stage microscopy and neutron diffractometry. Text. Microstruct. 31, 239–248.
Giustetto, R., Chiari, G., 2004. Crystal structure refinement of palygorskite from neutron powder diffraction. Eur. J. Mineral. 16, 521–532.
Granroth, G.E., Vandergriff, D.H., Nagler, S.E., 2006. SEQUOIA: A fine resolution chopper spectrometer at the SNS. Physica B 385–386, 1104–1106.
Green, D.W., Willhite, G.P., 1998. Enhanced Oil Recovery, SPE Textbook Series, Volume 6. Society of Petroleum Engineers, Richardson, Texas.
Grimaldi, N., Rojas, P.E., Stehle, S., Cordoba, A., Schweins, R., Sala, S., Luelsdorf, S., Piña, D., Veciana, J., Faraudo, J., Triolo, A., Braeuer, A.S., Ventosa, N., 2017. Pressure-responsive, surfactant-free CO_2 -based nanostructured fluids. ACS Nano 11, 10774–10784.
Guo, W., 2019. Porosity measurement in oil-well logging using a pulsed-neutron tool. AIP Conf. Proceed. 2160, 050002 https://doi.org/10.1063/1.5127694.
Hainbuchner, M., Villa, M., Kroupa, G., Bruckner, G., Baron, M., Amenitsch, H., Seidl, E., Rauch, H., 2000. The new high resolution ultra-small-angle neutron scattering instrument at the High Flux Reactor in Grenoble. J. Appl. Crystallogr. 33, 851–854.
Hall, S.A., 2013. Characterization of fluid flow in a shear band in porous rock using neutron radiography. Geophys. Res. Lett. 40, 2613–2618.
Hall, P.L., Mildner, D.F.R., Borst, R.L., 1983. Pore size distribution of shaly rock by small angle neutron scattering. Appl. Phys. Lett. 43, 252–254.
Hall, S.A., Wright, J., Pirling, T., Andò, E., Hughes, D.J., Viggiani, G., 2011. Can intergranular force transmission be identified in sand? Granul. Matter 13, 251–254.
Hall, S.A., Desrues, J., Viggiani, G., Bésuelle, P., Andò, E., 2012. Experimental characterisation of (localised) deformation phenomena in granular geomaterials from sample down to inter- and intra-grain scales, 4, 54–65.

Halpern, Y., Thieu, V., Henning, R.W., Wang, X., Schultz, A.J., 2001. Time-resolved in situ neutron diffraction studies of gas hydrate: Transformation of structure II (sII) to structure I (sI). J. Am. Chem. Soc. 123, 12826–12831.
Hammouda, B., 1995. A tutorial on small-angle neutron scattering from polymers. NIST Center for Neutron Research Report.
Hauk, V., 1997. Structural and Residual Stress Analysis by Nondestructive Methods. Elsevier.
Hayward, D.W., Chiappisi, L., Prévost, S., Schweins, R., Gradzielski, M., 2018. A small-angle neutron scattering environment for in-situ observation of chemical processes. Sci. Rep. 8, 7299.
He, L., Melnichenko, Y.B., Mastalerz, M., Sakurovs, R., Radlinski, A.P., Blach, T., 2012. Pore accessibility by methane and carbon dioxide in coal as determined by neutron scattering. Energy Fuels 26, 1975–1983.
Hemme, C., Van Berk, W., 2018. Hydrogeochemical modeling to identify potential risks of underground hydrogen storage in depleted gas fields. Appl. Sci. 8 (11), 2282. https://doi.org/10.3390/app8112282.
Hertzog, R.C., 1980. Laboratory and field evaluation of an inelastic neutron scattering and capture gamma ray spectrometry tool. In: Paper SPE 7430, 53rd Annual Technical Conference and Exhibition, Houston, Texas, Oct. 1-4.
Higgins, J.S., 2016. Neutron scattering from polymers: Five decades of developing possibilities. Annu. Rev. Chem. Biomol. Eng. 7, 1–28.
Hildenbrand, A., Urai, J.L., 2003. Investigation of the morphology of pore space in mudstones-first results. Mar. Pet. Geol. 20, 1185–1200.
Hinde, A.L., 2004. PRINSAS – a Windows-based computer program for the processing and interpretation of small-angle scattering data tailored to the analysis of sedimentary rocks. J. Appl. Crystallogr. 37, 1020–1024.
Hiraka, H., Lee, J., Jeon, B., Seong, B.S., Cho, S., 2020. Commissioning of neutron triple-axis spectrometers at HANARO. In: Nuclear Engineering and Technology (in preparation).
Hollamby, M.J., 2013. Practical applications of small-angle neutron scattering. Phys. Chem. Chem. Phys. 15, 10566–10579.
Hook, J.R., Hall, H.E., 1991. Solid state physics, 2nd Edition. Wiley.
Hosseini, M., 2016. Estimation of mean pore-size using formation evaluation and Stoneley slowness. J. Nat. Gas Sci. Eng. 33, 898–907.
Hosseini, M., 2018. Formation evaluation of a clastic gas reservoir: presentation of a solution to a fundamentally difficult problem. J. Geophys. Eng. 15, 2418–2432.
Hosseini, M., Javaherian, A., Movahed, B., 2014. Determination of permeability index using Stoneley slowness analysis, NMR models, and formation evaluations: a case study from a gas reservoir, south of Iran. J. Appl. Geophys. 109, 80–87.
Huang, T., Xie, B., Ran, Q., Zou, D., Zhong, G., 2015. Geophysical evaluation technology for shale gas reservoir: A case study in Silurian of Changning Area in Sichuan Basin. Energy Explor. Exploit. 33, 419–438.
Hyne, N.J., 2012. Nontechnical guide to petroleum geology, exploration, drilling & production, 3rd edition. PennWell Corp.
Ibrahim, Z., Martel, A., Moulin, M., Kim, H.S., Härtlein, M., Franzetti, B., Gabel, F., 2017. Time-resolved neutron scattering provides new insight into protein substrate processing by a AAA + unfoldase. Sci. Rep. 7, 40948.
Iglauer, S., 2011. Dissolution trapping of carbon dioxide in reservoir formation brine – A carbon sorage mechanism, Mass Transfer - Advanced Aspects, Hironori Nakajima. IntechOpen. https://doi.org/10.5772/20206.
Iglauer, S., 2018. Optimum storage depths for structural CO_2 trapping. Int. J. Greenhouse Gas Control. 77, 82–87.
Iglauer, S., Paluszny, A., Pentland, C.H., Blunt, M.J., 2011. Residual CO_2 imaged with X-ray micro-tomography. Geophys. Res. Lett. 38 (21).
Iglauer, S., Yaseri, A.Z., Rezaee, R., Lebedev, M., 2015. CO_2 wettability of caprocks: Implications for structural storage capacity and containment security. Geophys. Res. Lett. 42 (21), 9279–9284.
Iglauer, S., Paluszny, A., Rahman, T., Zhang, Y., Wülling, W., Lebdev, M., 2019. Residual trapping of CO_2 in an oil-filled, oil-wet sandstone core: results of three-phase pore scale imaging. Geophys. Res. Lett. 46, 11146–11154.
Iglauer, S., Abid, H., Al-Yaseri, A.Z., Keshavarz, A., 2021a. Hydrogen adsorption on sub-bituminous coal: Implications for hydrogen geo-storage. Geophys. Res. Lett. https://doi.org/10.1029/2021GL092976.
Iglauer, S., Ali, M., Keshavarz, A., 2021b. Hydrogen wettability of sandstone reservoirs: Implications for hydrogen geo-storage. Geophys. Res. Lett. https://doi.org/10.1029/2020GL090814.
Ikeda, T., Yamamuro, O., Matsuo, T., Mori, K., Torii, S., Kamiyama, T., Izumi, F., Ikeda, S., Mae, S., 1999. Neutron diffraction study of carbon dioxide clathrate hydrate. J. Phys. Chem. Solids 60, 1527–1529.
IPCC, 2005. In: Metz, B., Davidson, O., de Coninck, H.C., Loos, M., Meyer, L.A. (Eds.), IPCC Special Report on Carbon Dioxide Capture and Storage. Prepared by Working Group III of the Intergovernmental Panel on Climate Change. Cambridge University Press, Cambridge, United Kingdom and New York, NY, USA.
Istomin, V., Yakushev, V., Makhonina, N., Kwon, V.G., Chuvilin, E.M., 2006. Self-preservation phenomenon of gas hydrate (Published in Russian). Gas Indust. Russia. Digest 4, 16–27.
Ito, T., Nakajima, T., Xue, Z., 2017. Geological reservoir characterization and modelling of a CO_2 storage aquifer: A case study of the Nagaoka site. Energy Procedia. 114, 2792–2798.
Jacob, A., Mehmanparast, A., Kelleher, J., Burca, G., 2018. Neutron diffraction and neutron imaging residual strain measurements on offshore wind monopole weldments. Procedia Structural Integrity 13, 517–522.
Jasti, J.K., Lindsay, J.T., Fogler, H.S., 1987. Flow Imaging in Porous Media Using Neutron Radiography. 62nd Annual Technical Conference and Exhibition of the Society of Petroleum Engineers held in Dallas, Texas, September 27-30.
Jenkins, P.J., Donald, A.M., 1996. Application of small-angle neutron scattering to the study of the structure of starch granules. Polymer. 37, 5559–5568.
Jensen, A.C.S., 2018. Structure and dynamics of amorphous carbonates related to biomineralization: A neutron diffraction study. PhD diss. Universität Potsdam. https://publishup.uni-potsdam.de/frontdoor/index/index/docId/42169.
Johann, P.R.S., Monteiro, R.C., 2016. Geophysical reservoir characterization and monitoring at Brazilian pre-salt oil fields. In: Offshore Technology Conference, Houston, Texas, May 2-5.
Kaestner, A., Mannes, D., Hovind, J., Boillat, P., Lehmann, E., 2016. Combined neutron and X-ray imaging on different length scales. In: In proceedings of the 6th Conference on Industrial Computed Tomography, Wels, Austria.
Kaloyan, A.A., Kovalenko, E.S., Pakhnevich, A.V., Podurets, K.M., Rozhnov, S.V., Somenkov, V.A., 2014. Synchrotron and neutron tomography for the investigation of paleontological objects. Journal of Surface Investigation. X-ray, Synchrotron Neutron Tech. 8, 1093–1099.
Kaloyan, A.A., Kovalenko, E.S., Pakhnevich, A.V., Podurets, K.M., 2017. The contrast scale of minerals for neutron tomography of paleontologic and geologic objects. Russ. Geol. Geophys. 58, 1435–1440.
Kang, S.M., Fathi, E., Ambrose, R.J., Akkutlu, I.Y., Sigal, R.F., 2010. Carbon dioxide storage capacity of organic-rich shales. In: SPE Annual Technical Conference and Exhibition, Florence, Italy, September 19-22.
Kennett, J.P., Cannariato, K.G., Hendy, I.L., Behl, R.J., 2003. Methane hydrates in quaternary climate change: The clathrate gun hypothesis, volume 54. In: Special Publications Series, American Geophysical Union, Washington, D.C.
Keppler, R., Ullemeyer, K., Behrmann, J.H., Stipp, M., 2014. Potential of full pattern fit methods for the texture analysis of geological materials: implications from texture measurements at the recently upgraded neutron time-of-flight diffractometer SKAT. J. Appl. Crystallogr. 47, 1520–1534.
Klapproth, A., Piltz, R.O., Peterson, V.K., Kennedy, S.J., 2011. Neutron scattering studies on the formation and decomposition of gas hydrates near the ice point. In: Proceedings of the 7th International Conference on Gas Hydrates (ICGH 2011), Edinburgh, Scotland, United Kingdom, July 17-21.
Klaver, J., Hemes, S., Houben, M., Desbois, G., Radi, Z., Ural, J.L., 2015. The connectivity of pore space in mudstones: insights from high-pressure Wood's metal injection, BIB-SEM imaging, and mercury intrusion porosimetry. Geofluids. https://doi.org/10.1111/gfl.12128.
Knudsen, K.D., Fossum, J.O., Helgesen, G., Bergaplass, V., 2003. Pore characteristics and water absorption in a synthetic smectite clay. J. Appl. Crystallogr. 36, 587–591.
Knudsen, K.D., Simon, S., Geue, T., Cooper, J.F., Sjoblom, J., 2020. Interactions between asphaltenes and a model demulsifier in bulk and at an interface studied by small-angle neutron scattering (SANS) and neutron reflectometry. Energy Fuel 34 (6), 6768–6779.
Kocks, U.F., Tomé, C.N., Wenk, H.-R., 1998. Texture and Anisotropy: Preferred orientations in polycrystals and their effect on materials properties. Cambridge University Press.
Kocsis, L., Herman, P., Eke, A., 2006. The modified Beer–Lambert law revisited. Phys. Med. Biol. 51 (5), N91.
Kogure, T., 2013. Electron microscopy. In: Bergaya, F., Lagaly, G. (Eds.), Handbook of clay science (2nd Edition) Part B: Techniques and Applications, Developments in Clay Science, 5, pp. 275–317.
Kostorz, G., 1988. Small angle neutron scattering - Metallurgical applications. Mater. Sci. Forum 27-28, 325–344.
Kuang, Y., Lei, X., Yang, L., Zhao, Y., Zhao, J., 2018. Observation of in-situ growth and decomposition of Carbon dioxide hydrate at gas-water interfaces using MRI. Energy Fuel 32, 6964–6969.
Kuhs, W.F., 2004. The high pressure crystallography of gas hydrates. In: Katrusiak, A., Mcmillan, P. (Eds.), High-Pressure Crystallography. NATO Science Series (Series II: Mathematics, Physics and Chemistry), vol. 140. Springer, Dordrecht.
Kuhs, W.F., Genov, G., Staykova, D.K., Hansen, T., 2004. Ice perfection and onset of anomalous preservation of gas hydrates. Phys. Chem. Chem. Phys. 6, 4917–4920.
Kupperman, D.S., Hitterman, R.L., Rhodes, E., 1990. Energy Dependent Neutron Imaging. Tech. Rep. Argonne National Lab, IL (United States).
Lake, L.W., Johns, R., Rossen, B., Gary, P., 2014. Fundamentals of Enhanced Oil Recovery. Prentice Hall, Englewood Cliffs, NJ.
LaManna, J.M., Hussey, D.S., Baltic, E., Jacobson, D.L., 2017. Neutron and X-ray Tomography (NeXT) system for simultaneous, dual modality tomography. Rev. Sci. Instrum. 88, 113702.
Larson, A.C., Von Dreele, R.B., 2004. General Structure Analysis System (GSAS). Los Alamos National Laboratory Report LAUR 86–748.
Le Floch, S., Balima, F., Pischedda, V., Legrand, F., 2015. Small angle scattering methods to study porous materials under high uniaxial strain. Rev. Sci. Instrum. 86, 023901.
Lechner, R., Quittner, G., 1966. Pressure-Induced phonon frequency shifts in lead measured by inelastic neutron scattering. Phys. Rev. Lett. 17, 1259–1261.
Lehmann, E.H., Peetermans, S., Trtik, P., Betz, B., Grünzweig, C., 2017. New neutron imaging techniques to close the gap to scattering applications. J. Phys. Conf. Ser. 746, 012070.
Lennie, A.R., Tang, C.C., Thompson, S.P., 2004. The structure and thermal expansion behaviour of ikaite, $CaCO_3.6H_2O$, from T = 114 to T = 293 K. Mineral. Mag. 68, 135–146.
Leventouri, Th., Chakoumakos, B.C., Papanearchou, N., Perdikatsis, V., 2001. Crystal structure studies of natural and synthetic apatites by neutron powder diffraction. Mater. Sci. Forum 378-381, 517–522.
Levine, O.S., Fukai, I., Soeder, D.J., Bromhal, G., Dilmore, R.M., Guthrie, G.D., Rodosta, T., Sanguinito, S., Frailey, S., Gorecki, C., Peck, W., Goodman, A.L., 2016. U.S. DOE NETL methodology for estimating the prospective CO_2 storage resource of shales at the national and regional scale. Int. J. Greenhouse Gas Control. 51, 81–94.

Liang, L., Rinaldi, R., Schober, H., 2009. Neutron applications in earth, energy, and environmental sciences. Springer Science, New York, USA.
Liang, S., Han, H., Elsworth, D., Fu, X., Yao, Q., Kang, J., Li, X., Li, X., 2020. Evolution of production and transport characteristics of steeply-dipping ultra-thick coalbed methane reservoirs. Energies. 13 (19), 5081. https://doi.org/10.3390/en13195081.
Liu, Q., Maroto-Valer, M.M., 2011. Parameters affecting mineral trapping of CO_2 sequestration in brines. Greenhouse Gases 1 (3), 211–222.
Liu, K., Ostadhassan, M., Sun, L., Zou, J., Yuan, Y., Gentzis, T., Zhang, Y., Ortiz, H.C., Rezaee, R., 2019. A comprehensive pore structure study of the Bakken Shale with SANS, N2 adsorption and mercury intrusion. Fuel. 245, 274–285.
Liu, T., Gautam, S., Cole, D.R., Patankar, S., Tomasko, D., Zhou, W., Rother, G., 2020. Structure and dynamics of ethane confined in silica nanopores in the presence of CO_2. J. Chem. Phys. 152, 084707.
Lutterotti, L., Matthies, S., Wenk, H.-R., 1999. MAUD: a friendly Java program for materials analysis using diffraction. Int. U. Crystallogr. Comm. Powder Diffraction Newsletter. 21, 14–15.
Ma, L., Fauchille, A.L., Dowey, P.J., Pilz, F.F., Courtois, L., Taylor, K.G., Lee, P.D., 2017. Correlative multi-scale imaging of shales: a review and future perspectives. Geol. Soc. Lond., Spec. Publ. 454 (1), 175–199.
Mamontov, E., Herwig, K.W., 2011. A time-of-flight backscattering spectrometer at the Spallation Neutron Source. Rev. Sci. Inst. 82, 085109.
Mao, W., Ai, W., Sheng, L., Dou, X., Wang, P., Hong, D., Gao, W., 2020. A new slim hole neutron porosity logging while drilling tool using a pulsed neutron generator source. Soc. Petrol. Eng. https://doi.org/10.2118/203199-MS.
Marry, V., Dubois, E., Malikova, N., Durand-Vidal, S., Longeville, S., Breu, J., 2011. Water dynamics in hectorite clays: Infuence of temperature studied by coupling neutron spin echo and molecular dynamics. Environ. Sci. Technol. 45, 2850–2855.
Mason, T.E., Gawne, T.J., Nagler, S.E., Nestor, M.B., Carpenter, J.M., 2012. The early development of neutron diffraction: science in the wings of the Manhattan Project. Acta Crystallogr. A69, 37–44.
Masoomi, M., Shamsaei, N., Winholtz, R.A., Milner, J.L., Gnäupel-Herold, T., Elwany, A., Mahmoudi, M., Thompson, S.M., 2017. Residual stress measurements via neutron diffraction of additive manufactured stainless steel 17-4 PH. Data in Brief. 13, 408–414.
McFarlane, A.R., Geller, H., Silverwood, I.P., Cooper, R.I., Watkin, D.J., Parker, S.F., Winfield, J.M., Lennon, D., 2016. The application of inelastic neutron scattering to investigate the interaction of methyl propanoate with silica. Phys. Chem. Chem. Phys. 18, 17210–17216.
Melnichenko, Y.B., 2016. Small-Angle Scattering from Confined and Interfacial Fluids: Applications to Energy Storage and Environmental Science. Springer International Publishing, Switzerland.
Melnichenko, Y.B., Wignall, G.D., 2007. Small-angle neutron scattering in materials science: Recent practical applications. J. Appl. Phys. 102, 021101.
Melnichenko, Y.B., Wignall, G.D., Cole, D.R., Frielinghaus, H., 2006. Adsorption of supercritical CO_2 in aerogels as studied by small-angle neutron scattering and neutron transmission techniques. J. Chem. Phys. 124, 204711(11).
Melnichenko, Y.B., Radlinski, A.P., Mastalerz, M., Cheng, G., Rupp, J., 2009. Characterization of the CO_2 fluid adsorption in coal as a function of pressure using neutron scattering techniques (SANS and USANS). Aust. Coal Geol. 77, 69–79.
Melnichenko, Y.B., He, L., Sakurovs, R., Kholodenko, A.L., Blach, T., Mastalerz, M., Radlinski, A.P., Cheng, G., Mildner, D.F.R., 2012. Accessibility of pores in coal to methane and carbon dioxide. Fuel. 91, 200–208.
Menelle, A., Bellissent, R., Flank, A.M., 1989. Short range order in liquid Se-Te system by neutron scattering. Phys. B Condens. Matter 156 & 157, 174–176.
Meyer, H.W., Marion, S., Sondergeld, P., Carpenter, M.A., Knight, K.S., Redfern, S.A.T., Dove, M.T., 2001. Displacive components of the low-temperature phase transitions in lawsonite. Am. Mineral. 86, 566–577.
Meyer, A., Dimeo, R.M., Gehring, P.M., Neumann, D.A., 2003. The high-flux backscattering spectrometer at the NIST Center for Neutron Research, 74, pp. 2759–2777.
Middleton, M.F., Pázsit, I., Solymar, M., 2001. Petrophysical applications of neutron radiography. Nondestruct. Test. Evaluation. 16, 321–333.
Mildner, D.F.R., Hall, P.L., 1986. Small-angle scattering from porous solids with fractal Geometry. J. Phys. D. Appl. Phys. 19, 1535–1545.
Mouzakis, K.M., Navarre-Sitchler, A.K., Rother, G., Bañuelos, J.L., Wang, X., Kaszuba, J. P., Heath, J.E., Miller, Q.R.S., Alvarado, V., McCray, J.E., 2016. Experimental study of porosity changes in shale caprocks exposed to CO_2-saturated brines I: Evolution of mineralogy, pore connectivity, pore size distribution, and surface area environmental engineering science. Environ. Eng. Sci. 33, 725–735.
Mulder, M., Li, X.X., Nazim, M.M., Dalgliesh, R.M., Tian, B., Buijse, M., Van Wunnik, J., Bouwman, W.G., 2019. Systematically quantifying oil–water microemulsion structures using (spinecho) small angle neutron scattering. Colloids and Surfaces A. 575, 166–175.
Neil, C.W., Hjelm, R.P., Hawley, M.E., Watkins, E.B., Cockreham, C.B., Wu, D., Mao, Y., Fischer, T.B., Stokes, M.R., Xu, H., 2020a. Small-angle neutron scattering (SANS) characterization of clay- and carbonate-rich shale at elevated pressures. Energy Fuel 34 (7), 8178–8185.
Neil, C.W., Mehana, M., Hjelm, R.P., Hawley, M.E., Watkins, E.B., Mao, Y., Viswanathan, H., Kang, Q., Xu, H., 2020b. Reduced methane recovery at high pressure due to methane trapping in shale nanopores. Communicat. Earth & Environ. 1, 49.
Nesvizhevsky, V., Villain, J., 2017. The discovery of the neutron and its consequences (1930–1940). Comptes Rendus Physique. 18, 592–600.
Nikitin, A.N., Ivankina, T.I., Sobolev, G.A., Scheffzük, Ch., Frischbutter, A., Walther, K., 2004. Neutron Diffraction Study of Intracrystalline Strains and Stresses in a Marble Sample at High Temperatures and External Mechanical Loads. Izvestiya, Phys. Solid Earth. 40, 83–90.
Oesch, T., Weise, F., Meinel, D., Gollwitzer, C., 2019. Quantitative in-situ analysis of water transport in concrete completed using X-ray computed tomography. Transp. Porous Media 127, 371–389.
Oliveira, G.J.R., de Oliveira, P.C., Surmas, R., de Paulo Ferreira, L., Markötter, H., Kardjilov, N., Manke, I., Montoro, L.A., Isaac, A., 2019. Probing the 3D molecular and mineralogical heterogeneity in oil reservoir rocks at the pore scale. Sci. Rep. 9, 8263.
Oyeyemi, K.D., Olowokere, M.T., Aizebeokhai, A.P., 2019. Prospect analysis and hydrocarbon reservoir volume estimation in an exploration field, shallow offshore depobelt, Western Niger Delta, Nigeria. Nat. Resour. Res. 28, 173–185.
Pakhnevich, A., Kurkin, A., Lavrov, A., Tarasenko, K., Kovalenko, E., Kaloyan, A., Podurets, K., 2018. Synchrotron and neutron tomography of paleontological objects on the facilities of the kurchatov Institute. J. Imaging. 4, 103. https://doi.org/10.3390/jimaging4080103.
Parise, J.B., Leinenweber, K., Weidner, D.J., Tan, K., Von Dreele, R.B., 1994. Pressure-induced H bonding: Neutron diffraction study of brucite, Mg (OD)2, to 9.3 GPa. Am. Mineral. 79, 193–196.
Pearce, J.K., Dawson, G.K.W., Blach, T.p., Bahadur, J., Melnichenko, Y.B., Golding, S.D., 2018. Impure CO_2 reaction of feldspar, clay, and organic matter rich cap-rocks: Decreases in the fraction of accessible mesopores measured by SANS. Int. J. Coal Geol. 185, 79–90.
Pefoute, E., Martin-Gondre, L., Ollivier, J., Soetens, J.-C., Russina, M., Desmedt, A., 2017. Modeling the THF clathrate hydrate dynamics by combining molecular dynamics and quasi-elastic neutron scattering. Chem. Phys. 496, 24–34.
Pereira, G.F.L., Costa, F.N., Souza, J.A., Haddad, P.S., Ferreira, F.F., 2018. Parametric Rietveld refinement and magnetic characterization of superparamagnetic iron oxide nanoparticles. J. Magn. Magn. Mater. 456, 108–117.
Perfect, E., Cheng, C.-L., Kang, M., Bilheux, H.Z., Lamanna, J.M., Gragg, M.J., Wright, D. M., 2014. Neutron imaging of hydrogen-rich fluids in geomaterials and engineered porous media: A review. Earth Sci. Rev. 129, 120–135.
Perfect, E., Brabazon, J.W., Gates, C.H., 2020. Forward prediction of early-time spontaneous imbibition of water in unsaturated rock fractures. Vadose Zone J. https://doi.org/10.1002/vzj2.20056.
Perreault, C., Vohra, Y.K., Dos Santos, A.M., Molaison, J.J., Boehler, R., 2019. Magnetic ordering in rare earth metal dysprosium revealed by neutron diffraction studies in a large-volume diamond anvil cell. High Pressure Research 39, 588–597.
Piovano, A., 2015. Inelastic neutron scattering applied to materials for energy. Eur. Phys. J. Conf. 104, 01006.
Pluymaekers, M.P.D., Kramers, L., Van Wees, J.-D., Kronimus, A., Nelskamp, S., Boxem, T., Bonté, D., 2012. Reservoir characterisation of aquifers for direct heat production: Methodology and screening of the potential reservoirs for the Netherlands. J. Geosci. Geologie En Mijnbouw 91 (4), 621–636.
Pollock, R.A., Walsh, B.R., Fry, J., Ghampson, I.T., Melnichenko, Y.B., Kaiser, H., Pynn, R., DeSisto, W.J., Wheeler, M.C., Frederick, B.G., 2011. Size and spatial distribution of micropores in SBA-15 using CM-SANS. Chem. Mater. 23, 3828–3840.
Polsky, Y., Anovitz, L.M., Bingham, P., Carmichael, J., 2013a. Application of neutron imaging to investigate flow through fractures for EGS. In: Thirty-Eighth Workshop on Geothermal Reservoir Engineering, Stanford University, Stanford, California, February 11-13.
Polsky, Y., Dessieux, L., An, K., Anovitz, L.M., Bingham, P., Carmichael, J., 2013b. Development of a neutron diffraction based experimental capability for investigating hydraulic fracturing for EGS-like conditions. In: Thirty-Eighth Workshop on Geothermal Reservoir Engineering, Stanford University, Stanford, California, February 11-13.
Proffen, T., Billinge, S.J.L., 1999. PDFFIT, a program for full profile structural refinement of the atomic pair distribution function. J. Appl. Crystallogr. 32, 572–575.
Pryakhin, E.A., Mokrov, Y.G., Tryapitsina, G.A., Ivanov, I.A., Osipov, D.I., Atamanyuk, N. I., Deryabina, L.V., Shaposhnikova, I.A., Shishkina, E.A., Obvintseva, N.A., Egoreichenkov, E.A., Styazhkina, E.V., Osipova, O.F., Mogilnikova, N.I., Andreev, S. S., Tarasov, O.V., Geras'kin, S.A., Trapeznikov, A.V., Akleyev, A.V., 2015. Characterization of biocenoses in the storage reservoirs of liquid radioactive wastes of Mayak PA. Initial descriptive report. J. Environ. Radioact. 151, 449–460.
Purevjav, N., Okuchi, T., Tomioka, N., Wang, X., Hoffmann, C., 2016. Quantitative analysis of hydrogen sites and occupancy in deep mantle hydrous wadsleyite using single crystal neutron diffraction. Sci. Rep. 6, 34988.
Radlinski, A.P., Hinde, A.L., 2001. Applications of small angle neutron scattering and small angle X-ray scattering to petroleum geology. In: Proceedings of the ESRF/ILL Joint Workshop on Environmental Studies Using Neutron and Synchrotron Facilities, Grenoble, France.
Radlinski, A.P., Boreham, C.J., Lindner, P., Randl, O., Wignall, G.D., Hinde, A., Hope, J. M., 2000. Small angle neutron scattering signature of oil generation in artificially and naturally matured hydrocarbon source rocks. Org. Geochem. 31, 1–14.
Radlinski, A.P., Ioannidis, M.A., Hinde, A.L., Hainbuchner, M., Baron, M., Rauch, H., Kline, S.R., 2002. Multiscale characterization of reservoir rock microstructure: combining Small Angle Neutron Scattering and image analysis. In: Proceedings of International Symposium of the Society of Core Analysts, Monterey, California, September 22-25.
Radlinski, A.P., Ioannidis, M.A., Hinde, A.L., Hainbuchner, M., Baron, M., Rauch, H., Kline, S.R., 2004. Angstrom-to-millimeter characterization of sedimentary rock microstructure. J. Colloid Interface Sci. 274, 607–612.
Ramirez-Cuesta, A.J., Jones, M.O., David, W.I.F., 2009. Neutron Scattering and Hydrogen Storage, 12, pp. 54–61.
Ramsay, J.D.F., 1988. Neutron scattering from porous solids. Stud. Surf. Sci. Catal. 39, 23–34.

Ramsay, J.D.F., 1993. Applications of neutron scattering in investigations of adsorption processes in porous materials. Pure Appl. Chem. 65 (10), 2169–2174.
Rashid, F., Glover, P.W.J., Lorinczi, P., Hussein, D., Collier, R., Lawrence, J., 2015. Permeability prediction in tight carbonate rocks using capillary pressure measurements. Mar. Pet. Geol. 68, 536–550.
Raza, A., 2017. Reservoir characterization for CO_2 injectivity and flooding in petroleum reservoirs, offshore Malaysia. PhD diss. Curtin University. http://hdl.handle.net/20.500.11937/57524.
Redfern, S.A.T., 2002. Neutron powder diffraction of minerals at high pressures and temperatures: some recent technical developments and scientific applications. Eur. J. Mineral. 14, 251–261.
Redfern, S.A.T., Henderson, C.M.B., Knight, K.S., Wood, B.J., 1997. High-temperature order-disorder in (Fe0.5Mn0.5)2SiO4 and (Mg0.5Mn0.5)2SiO4 olivines: an in situ neutron diffraction study. Eur. J. Mineral. 9, 287–300.
Redfern, S.A.T., Artioli, G., Rinaldi, R., Henderson, C.M.B., Knight, K.S., Wood, B.J., 2000. Octahedral cation ordering in olivine at high temperature. II: an in situ neutron powder diffraction study on synthetic MgFeSiO4 (Fa50). Phys. Chem. Miner. 27, 630–637.
Rehm, C., Barker, J., Bouwman, W.G., Pynn, R., 2012. DCD USANS and SESANS: a comparison of two neutron scattering techniques applicable for the study of large-scale structures. J. Appl. Crystallogr. 46, 1–11.
Rezaeyan, A., Seemann, T., Bertier, P., Pipich, V., Leo, L., Kampman, N., Feoktystov, A., Barnsley, L.C., Busch, A., 2019. Understanding pore structure of mudrocks and pore-size dependent sorption mechanism using Small Angle Neutron Scattering. In: SPE/AAPG/SEG Asia Pacific Unconventional Resources Technology Conference, Brisbane, Australia, November 18 –19.
Rhodes, E., Kupperman, D.S., Hitterman, R.L., 1992. Dual-energy neutron tomography of water in rock using the argonne IPNS. In: Tech. Rep. Argonne National Lab, IL (United States).
Rietveld, H.M., 1967. Line profiles of neutron powder-diffraction peaks for structure refinement. Acta Cryst 22, 151–152.
Rietveld, H.M., 1969. A Profile Refinement Method for Nuclear and Magnetic Structures. J. Appl. Crystallogr. 2, 65–71.
Rinaldi, R., 2002. Neutron scattering in mineral sciences: Preface. Eur. J. Mineral. 14, 195–202.
Rodríguez-Carvajal, J., 1990. FULLPROF: A program for Rietveld refinement and pattern matching analysis. www.llb.cea.fr/fullweb/fp2k/fp2k.htm.
Ruppert, L.F., Sakurovs, R., Blach, T.P., He, L., Melnichenko, Y.B., Mildner, D.F.R., Alcantar-Lopez, L., 2013. A USANS/SANS study of the accessibility of pores in the Barnett shale to methane and water. Energy Fuel 27, 772–779.
Rush, J.J., 2015. US neutron facility development in the last half-century: A cautionary tale. Phys. Perspect. 17, 135–155.
Russel, T.P., Lin, J.S., Spooner, S., Wignall, G.D., 1988. Intercalibration of Small-angle X-ray and neutron scattering data. J. Appl. Crystallogr. 21, 629–638.
Santisteban, J.R., Edwards, L., Fitzpatrick, M.E., Steuwer, A., Withers, P.J., Daymond, M. R., Johnson, M.W., Rhodesd, N., Schooneveld, E.M., 2002. Strain imaging by Bragg edge neutron transmission. Nuc. Instr. Meth. Phys. Res. A. 481, 765–768.
Schafer, W., 2002. Neutron diffraction applied to geological texture and stress analysis. Eur. J. Mineral. 14, 263–289.
Schlumberger Oilfield Glossary, 2021. Schlumberger. https://www.glossary.oilfield.slb.com/.
Schofield, P.F., Knight, K.S., Stretton, I.C., 1996. Thermal expansion of gypsum investigated by neutron powder diffraction. Am. Mineral. 81, 847–851.
Schwarz, D., Vontobel, P., Lehmann, E.H., Meyer, C.A., Bongartz, G., 2005. Neutron tomography of internal structures of vertebrate remains: A comparison with X-ray computed tomography. Palaeontol. Electron. 8 (2), 30A, 11p.
Sen, D., Mazumder, S., 2002. Pore morphology and pore surface roughening in rocks: a small-angle neutron scattering investigation. J. Mater. Sci. 37, 941–947.
Shull, C.G., Smart, J.S., 1949. Detection of antiferromagnetism by neutron diffraction. Phys. Rev. 76, 1256–1257.
Sinha, S., Braun, E.M., Determan, M.D., Passey, Q.R., Leonardi, S.A., Boros, J.A., Wood, A.C., Zirkle, T., Kudva, R.A., 2013a. Steady-state permeability measurements on intact shale samples at reservoir conditions – Effects of stress, temperature, pressure, and type of gas. In: SPE Middle East Oil and Gas Show and Conference held in Manama, Bahrain, March 10-13.
Sinha, V., Srivastava, A., Lee, H.K., Liu, X., 2013b. Performance evaluation of a combined neutron and X-ray digital imaging system. Proc. of SPIE. 8694, 86940R–2.
Skipper, N.T., Williams, G.D., De Sequeira, A.V.C., Lobban, C., Soper, A.K., 2000. Time-of-flight neutron diffraction studies of clay-fluid interactions under basin conditions. Clay Miner. 35, 283–290.
Smith, J.C., Kneller, G.R., 1993. Combination of neutron scattering and molecular dynamics to determine internal motions in biomolecules. Mol. Simul. 10 (2–6), 363–375.
Song, K., Liu, L., Zhang, D., Hautzinger, M.P., Jin, S., Han, Y., 2020. Atomic-resolution imaging of halide perovskites using electron microscopy. Adv. Energy Mater. 10 (26), 1904006.
Stauffer, D., 1979. Scaling theory of percolation clusters. Phys. Rep. 54, 1–74.
Stavropoulou, E., Andò, E., Tengattini, A., Briffaut, M., Dufour, F., Atkins, D., Armand, G., 2019. Liquid water uptake in unconfined Callovo Oxfordian clay-rock studied with neutron and X-ray imaging. Acta Geotech. 14, 19–33.
Stefanopoulos, K.L., Steriotis, T.A., Katsaros, F.K., Kanellopoulos, N.K., Hannon, A.C., Ramsay, J.D.F., 2012. Structural study of supercritical carbon dioxide confined in nanoporous silica by in situ neutron diffraction. J. Phys. Conf. Ser. 340, 012049.
Stefanopoulos, K.L., Katsaros, F.K., Steriotis, Th.A., Sapalidis, A.A., Thommes, M., Bowron, D.T., Youngs, T.G.A., 2016. Anomalous depletion of pore-confined carbon dioxide upon cooling below the bulk triple point: An in situ neutron diffraction study. Phys. Rev. Lett. 116 (025502), 6.
Stefanopoulos, K.L., Youngs, T.G.A., Sakurovs, R., Ruppert, L.F., Bahadur, J., Melnichenko, Y.B., 2017. Neutron scattering measurements of carbon dioxide adsorption in pores within the Marcellus shale: Implications for sequestration. Environ. Sci. Technol. 51, 6515–6521.
Steriotis, Th.A., Stefanopoulos, K.L., Kanellopoulos, N.K., Mitropoulos, A.Ch., Hoser, A., 2004. The structure of adsorbed CO_2 in carbon nanopores: a neutron diffraction study. Coll. Surf. A 241, 239–244.
Stern, L.A., Circone, S., Kirby, S.H., Durham, W.B., 2001. Anomalous preservation of pure methane hydrate at 1 atm. J. Phys. Chem. B 105, 1756–1762.
Stinton, G.W., Evans, J.S.O., 2007. Parametric Rietveld refinement. J. Appl. Crystallogr. 40, 87–95.
Strobl, M., Harti, R.P., Grünzweig, C., Woracek, R., Plomp, J., 2017. Small angle scattering in neutron imaging—A review. J. Imag. 3, 64.
Sun, M., Yu, B., Hu, Q., Yang, R., Zhang, Y., Li, B., Melnichenko, Y.B., Cheng, G., 2017. Pore structure characterization of organic-rich Niutitang shale from China: Small angle neutron scattering (SANS) study. Int. J. Coal Geol. https://doi.org/10.1016/j.coal.2017.12.006.
Sun, M., Zhang, L., Hu, Q., Pan, Z., Yu, B., Sun, L., Bai, L., Fu, H., Zhang, Y., Zhang, C., Cheng, G., 2019. Multiscale connectivity characterization of marine shales in southern China by fluid intrusion, small-angle neutron scattering (SANS), and FIB-SEM. Mar. Pet. Geol. https://doi.org/10.1016/j.marpetgeo.2019.104101.
Swainson, I.P., Hammond, R.P., 2003. Hydrogen bonding in ikaite, CaCO3.6H2O. Mineral. Mag. 67, 555–562.
Swenson, J., Bergman, R., Longeville, S., 2001. A neutron spin-echo study of confined water. J. Chem. Phys. 115, 11299–11305.
Tang, S., Tang, D., Tang, J., Tao, S., Xu, H., Geng, Y., 2017. Controlling factors of coalbed methane well productivity of multiple superposed coalbed methane systems. Energy Explor. Exploit. 35, 665–684.
Tengattini, A., Lenoir, N., Andò, E., Viggiani, G., 2020. Neutron imaging for geomechanics: A review. Geomechanics for Energy and the Environment. In Press, Corrected Proof. https://doi.org/10.1016/j.gete.2020.100206.
Thanh, H.V., Sugai, Y., Sasaki, K., 2020. Application of artificial neural network for predicting the performance of CO_2 enhanced oil recovery and storage in residual oil zones. Sci. Rep. 10, 18204.
Thompson, H., Soper, A.K., Buchanan, P., Aldiwan, N., Creek, J.L., Koh, C.A., 2006. Methane hydrate formation and decomposition: Structural studies via neutron diffraction and empirical potential structure refinement. J. Chem. Phys. 124, 164508.
Toby, B.H., 2000. EXPGUI, a graphical user interface for GSAS. J. Appl. Crystallogr. 34, 210–213.
Tomioka, N., Okuchi, T., Purevjav, N., Abe, J., Harjo, S., 2016. Hydrogen sites in the dense hydrous magnesian silicate phase E: a pulsed neutron powder diffraction study. Phys. Chem. Miner. 43, 267–275.
Tötzke, C., Kardjilov, N., Manke, I., Oswald, S.E., 2017. Capturing 3D water flow in rooted soil by ultra-fast neutron tomography. Sci. Rep. 7, 6192. https://doi.org/10.1038/s41598-017-06046-w.
Trouw, F.R., 1992. Molecular dynamics simulation and inelastic neutron scattering. Spectrochim. Acta 48A, 455–476.
Tsang, C.F., Neretnieks, I., Tsang, Y., 2015. Hydrologic issues associated with nuclear waste repositories. Water Resour. Res. 51, 6923–6972.
Tudisco, E., Etxegarai, M., Hall, S.A., Charalampidou, E.M., Couples, G.D., Lewis, H., Tengattini, A., Kardjilov, N., 2019. Fast 4D imaging of fluid flow in rock by high-speed neutron tomography. JGR: Solid Earth 124, 3557–3569.
Underwood, M.C., Dyos, C.J., 1986. Inelastic neutron scattering reactions in fluid saturated rock as exploited in oil well logging. Int. J. Radiat. Appl. Instrument. 37, 475–481.
Urakawa, S., Inoue, T., Hattori, T., Sano-Furukawa, A., Kohara, S., Wakabayashi, D., Sato, T., Funamori, N., Funakoshi, K.-I., 2020. X-ray and neutron study on the structure of hydrous SiO_2 glass up to 10 GPa. Minerals. 10, 84.
Vontobel, P., Lehmann, E., Carlson, W.D., 2005. Comparison of X-ray and neutron tomography investigations of geological materials. IEEE Trans. Nucl. Sci. 52, 338–341.
Vrij, A., 2003. Neutron scattering of colloidal particle dispersions; contrast variation with homogeneous and granular solvents. Coll. Surf. A 213, 117–129.
Walther, K., Heinitz, J., Ullemeyer, K., Betzl, M., Wenk, H.-R., 1995. Time-of-Flight texture analysis of limestone standard: Dubna results. J. Appl. Crystallogr. 28, 503–507.
Wang, H.-W., Daemen, L.L., Cheshire, M.C., Kidder, M.K., Stack, A.G., Allard, L.F., Neuefeind, J., Olds, D., Liu, J., Page, K., 2017. Synthesis and structure of synthetically pure and deuterated amorphous (basic) calcium carbonates. Chem. Commun. 53, 2942–2945.
Weber, B., Wyrzykowski, M., Griffa, M., Carl, S., Lehmann, E., Lura, P., 2013. Neutron radiography of heated high-performance mortar. MATEC Web Conf. 6, 03004.
Webster, G.A., Wimpory, R.W., Youtsos, A.G., Ohms, C., 2002. Polycrystalline materials determination of residual stresses by neutron diffraction. European Communities.
Wenk, H.-R. (Ed.), 1985. Preferred orientation in deformed metals and rocks: an introduction to modern texture analysis. Academic Press, London.
Wenk, H.-R., 1991. Standard project for pole-figure determination by neutron diffraction. J. Appl. Crystallogr. 24, 920–927.
Wenk, H.-R. (Ed.), 2006. Neutron Scattering in Earth Sciences. Reviews in Mineralogy and Geochemistry. Vol, 63. The Mineralogical Society of America, Washington.
Wenk, H.-R., 2012. Application of Neutron Scattering in Earth Sciences. J. Min. Metals & Mater. Soc. 64 (1), 127–137.

Wenk, H.-R., Kern, H., Schaefer, W., Will, G., 1984. Comparison of neutron and X-ray diffraction in texture analysis of deformed carbonate rocks. J. Struct. Geol. 6, 687–692.
Wenk, H.-R., Yu, R., Vogel, S., Vasin, R., 2019. Preferred orientation of quartz in metamorphic rocks from the Bergell Alps. Minerals. 9, 277.
Wensrich, C.M., Kisi, E.H., Zhang, J.F., Kirstein, O., 2012. Measurement and analysis of the stress distribution during die compaction using neutron diffraction. Granul. Matter 14, 671–680.
Wignall, G.D., Melnichenko, Y.B., 2005. Recent applications of small-angle neutron scattering in strongly interacting soft condensed matter. Rep. Prog. Phys. 68, 1761–1810.
Wilding, M., Lesher, C.E., Shields, K., 2005. Applications of neutron computed tomography in the geosciences. Nucl. Inst. Methods Phys. Res. A 542, 290–295.
Winkler, B., Knorr, K., Kahle, A., Vontobel, P., Lehmann, E., Hennion, B., Bayon, G., 2002. Neutron imaging and neutron tomography as non-destructive tools to study bulk-rock samples. Eur. J. Mineral. 14, 349–354.
Wong, P.-Z., Howard, J., Lin, J.S., 1986. Surface roughening and the fractal nature of rocks. Phys. Rev. Lett. 57, 637–640.
Xu, H., 2019. Probing nanopore structure and confined fluid behavior in shale matrix: A review on small-angle neutron scattering studies. Int. J. Coal Geol. 217. Article 103325.
Yang, R., He, S., Hu, O., Sun, M., Hu, D., Yi, J., 2017. Applying SANS technique to characterize nano-scale pore structure of Longmaxi shale, Sichuan Basin (China). Fuel. 197, 91–99.
Ye, Z., Hou, E., Duan, Z., Li, Z., 2019. Coal reservoir characterization in a tectonic setting and the effects of tectonism on the coalbed methane (CBM) content. Adv. Mater. Sci. Eng. https://doi.org/10.1155/2019/7974628.
Yehya, M., Ando, E., Dufour, F., Tengattini, A., 2018. Fluid-flow measurements in low permeability media with high pressure gradients using neutron imaging: Application to concrete. Nuclear Inst. and Methods in Physics Research, A. 890, 35–42.
Yekta, A.E., Manceau, J.-C., Gaboreau, S., Pichavant, M., Audigane, P., 2018. Determination of hydrogen–water relative permeability andc Pressure in sandstone: Application to underground hydrogen injection in sedimentary formations. Transp. Porous Media 122, 333–356.
Yoshida, K., Yamaguchi, T., Kittaka, S., Bellissent-Funel, M.C., Fouquet, B., 2008. Thermodynamic, structural, and dynamic properties of supercooled water confined in mesoporous MCM-41 studied with calorimetric, neutron diffraction, and neutron spin echo measurements. J. Chem. Phys. 129, 054702.
Young, R.A., Wiles, D.B., 1982. Profile shape functions in Rietveld refinements. J. Appl. Crystallogr. 15, 430–438.
Zabel, H., Siebrecht, R., Schreyer, A., 2000. Neutron reflectometry on magnetic thin films. Physica B 276-278, 17–21.
Zambrano, M., Hameed, F., Anders, K., Mancini, L., Tondi, E., 2019. Implementation of dynamic neutron radiography and integrated X-ray and neutron tomography in porous carbonate reservoir rocks. Front. Earth Sci. 7, 329. https://doi.org/10.3389/feart.2019.00329.
Zhang, H., Al-Farisi, O., Raza, A., Zhang, T., 2018. NMR-MRI characterization of low-salinity water alternating CO_2 flooding in tight carbonate. In: SEG/AAPG/EAGE/SPE Research and Development Petroleum Conference and Exhibition, Abu Dhabi, UAE, May 9-10.
Zhao, J., Chen, H., Yin, L., Li, N., 2017a. Mineral inversion for element capture spectroscopy logging based on optimization theory. J. Geophys. Eng. 14, 1430.
Zhao, J., Jin, Z., Hu, Q., Jin, Z., Barber, T.J., Zhang, Y., Bleuel, M., 2017b. Integrating SANS and fluid invasion methods to characterize pore structure of typical American shale oil reservoirs. Sci. Rep. 7, 15413.
Zhao, Y., Xue, S., Han, S., Chen, Z., Liu, S., Elsworth, D., He, L., Cai, J., Liu, Y., Chen, D., 2017c. Effects of microstructure on water imbibition in sandstones using X-ray computed tomography and neutron radiography. Solid Earth. 122, 4963–4981.
Zhao, Y., Wu, Y., Han, S., Xue, S., Fan, G., Chen, Z., El Abd, A., 2019. Water sorptivity of unsaturated fractured sandstone: fractal modeling and neutron radiography experiment. Adv. Water Resour. 130, 172–183.
Zhou, Z., Bouwman, W.G., Schut, H., Desert, S., Jestin, J., Hartmann, S., Pappas, C., 2016. From nanopores to macropores: Fractal morphology of graphite. Carbon. 96, 541–547.
Zhu, Z., Lei, X., Xu, N., Shao, D., Jiang, X., Wu, X., 2020. Integration of 3D geological modeling and geothermal field analysis for the evaluation of geothermal reserves in the northwest of Beijing Plain, China. Water 12, 638.
Zucali, M., Tartarotti, P., Capelli, S., Ouladdiaf, B., 2012. Multiscalar structural study of the ultramafic rocks of the Antrona Ophiolite (Pennine Alps). J. Virtual Explor. 41 https://doi.org/10.3809/jvirtex.2011.00295 paper 4.
Zucali, M., Chateigner, D., Ouladdiaf, B., 2020. Crystallographic and seismic anisotropies of calcite at different depths: A study using quantitative texture analysis by neutron diffraction. Minerals. 10 (1), 26. https://doi.org/10.3390/min10010026.